

Dissertation

Structural and functional characterization of the actin and microtubule
cytoskeleton in dendrites

Zur Erlangung des Doktorgrades der Naturwissenschaften am Fachbereich
Chemie der Fakultät für Mathematik, Informatik und Naturwissenschaften der
Universität Hamburg

doctor rerum naturalium
(Dr. rer. nat.)

im April 2020

eingereichte Dissertation,

vorgelegt von M.Sc. Bas van Bommel

van Bommel, Bas

Structural and functional characterization of the actin and microtubule cytoskeleton in dendrites

Dissertation, Fakultät für Mathematik, Informatik und Naturwissenschaften

Universität Hamburg

April 2020

Gutachter

Dr. Marina Mikhaylova

AG Neuronal Protein Transport, Center for Molecular Neurobiology Hamburg at the University
Medical Center Hamburg-Eppendorf, Hamburg

Prof. Dr. Henning Tidow

Institute for Biochemistry and Molecular Biology, University of Hamburg, Hamburg

Disputation

24. Juli 2020

Mitglieder der Prüfungskommission

Prof. Dr. Kay Grünewald

Institute for Biochemistry and Molecular Biology, Center for Structural Systems Biology, Hamburg

Prof. Dr. Thomas G. Oertner

Institute for Synaptic Plasticity, Center for Molecular Neurobiology Hamburg at the University
Medical Center Hamburg-Eppendorf, Hamburg

Dr. Marina Mikhaylova

AG Neuronal Protein Transport, Center for Molecular Neurobiology Hamburg at the University
Medical Center Hamburg-Eppendorf, Hamburg

Practical work was conducted between April 2016 and April 2020 in the research group 'Neuronal Protein Transport', Center for Molecular Neurobiology Hamburg at the University Medical Center Hamburg-Eppendorf in frame of the ZMNH graduate programme.

Supervisors

Dr. Marina Mikhaylova

'Neuronal Protein Transport', Center for Molecular Neurobiology Hamburg at the University Medical Center Hamburg-Eppendorf, Hamburg

Prof. Dr. Henning Tidow

Institute for Biochemistry and Molecular Biology, University of Hamburg, Hamburg

Co-Supervisor

Prof. Dr. Thomas G. Oertner

Institute for Synaptic Physiology, Center for Molecular Neurobiology Hamburg at the University Medical Center Hamburg-Eppendorf, Hamburg

Publications

Long-term information storage at schaffer collateral synapses does not depend on the sequence of pre-and postsynaptic spikes

Anisimova M., **van Bommel B.**, Wiegert S.J., Mikhaylova M., Oertner T.G., Gee C.E.

Submitted/ BioRxiv, 2019, Research article

F-actin patches associated with glutamatergic synapses control positioning of dendritic lysosomes

van Bommel B.*, Konietzny A.* , Kobler O., Bär J., Mikhaylova M.

The EMBO Journal, 2019, Research article

Caldendrin directly couples postsynaptic calcium signals to actin remodeling in dendritic spines
Mikhaylova M*., Bär J.* , **van Bommel B.**, Schätzle P., YuanXiang P., Raman R., Hradsky J., Konietzny A., Loktionov E.Y., Reddy P.P., Lopez-Rojas J., Spilker C., Kobler O., Raza S.A., Stork O., Hoogenraad C.C., Kreutz M.R.

Neuron, 2018, Research article

Periodic F-actin structures shape the neck of dendritic spines

Bär J.* , Kobler O*., **van Bommel B.***, Mikhaylova M.

Scientific Reports, 2016, Research article

Talking to the neighbours: The molecular and physiological mechanisms of clustered synaptic plasticity

van Bommel B., Mikhaylova M.

Neuroscience & Biobehavioral Reviews, 2016, Review

** These authors contributed equally to the work.*

Abstract

The brain consists of billions of neurons that connect in networks and communicate for brain function. Neurons are connected to one another via chemical synapses. In chemical synapses, signals are conveyed via neurotransmitter release from presynaptic to postsynaptic sites. Synapses are complex structures with a densely packed postsynaptic scaffold, the postsynaptic density, supported by the cellular cytoskeleton. Synapses can persist for long periods of time, and are maintained by an equilibrium in synaptic protein exchange. Hereby synaptic structures exist for much longer periods than the synaptic residing time of individual proteins from which they are built. Changing the synaptic equilibrium (plasticity) leads to changes in synaptic strength, the effectiveness of neuron-to-neuron communication. By strengthening (enlarging or the formation of additional synaptic connections) or weakening (shrinking or loss of synaptic connections) connectivity, the neuronal network tunes the propagation of activity, and has the ability to process and store information.

The maintenance and plasticity of synapses requires local sources and machineries for protein turnover. Neurons have a sophisticated organelle repertoire to produce, degrade or recycle proteins. Part of these organelles, mainly small sized by character, are transported far into the dendritic and axonal arbour. This is believed to be essential for the local support of synapses. Larger organelles, e.g. ER and mitochondria, are less mobile. The organelles present within dendrites allow for local translation, recycling and degradation of proteins. This is not the exclusive source of new proteins. Some proteins, mainly transmembrane proteins, are produced by the organelles located within the soma. These proteins are subsequently transported towards synapses by active transport. This transport is guided along the cytoskeleton built of microtubules and filamentous actin, which at the same time provides structural support. The ongoing dynamics of organelles supports the maintenance and plasticity of synapses.

This work was aimed to understand how the cytoskeleton and intracellular transport supports synapses. To do this I performed studies with the focus on i) the cytoskeletal architecture at the nanoscale level, ii) signalling that alters synaptic cytoskeleton organisation, iii) and transport of organelles that could support synapses. Super-resolution STED nanoscopy revealed that the neck of dendritic protrusions is supported by a periodic actin lattice and indicated the presence of actin patches located within dendritic shafts. The actin lattice in spines shows strong similarities with an earlier described membrane associated cytoskeleton and could be placed within this category of actin structures. The actin patches appeared to associate with excitatory synapses. Moreover, sets of advanced light microscopy experiments elicited a crucial role of the calcium binding protein caldendrin in controlling spinous actin dynamics during the process of synaptic strengthening (long-term potentiation). During this process caldendrin, via the F-actin binding protein cortactin, protects and stabilises an essential pool of synaptic actin filaments. This F-actin pool forms the stable basis for the establishment of a new actin arrangement and enables formation of a larger spine head, which holds a new protein equilibrium.

Experiments focussing on organelle transport illustrated that dendritic actin patches strongly influence organelle transport. These actin structures are spaced loosely within the dendritic branch, are part of excitatory shaft synapses or can be found at the base of dendritic spines.

STRUCTURAL AND FUNCTIONAL CHARACTERIZATION OF THE ACTIN AND MICROTUBULE
CYTOSKELETON IN DENDRITES
M.SC. BAS VAN BOMMEL

Lysosomes, here used as model organelle, halt/pause at these actin patches. This is induced by actin, forming a physical barrier for microtubule-based transport and by providing binding places for myosin V. It is yet unclear what the halting of organelles exactly achieves in terms of function. It could be that halting is an essential prerequisite to focus organelle function towards particular places. Hereby they could boost protein turnover and support synapses at particular dendritic segments, perhaps at dendritic segments where ongoing activity and synaptic plasticity takes place. Moreover, dendritic actin might also halt different organelles which could promote fusion, exchange of content and maturation. Future experiments could elicit the exact function of organelle halting. Organelles and their dynamics might directly contribute to the 'rules' of synaptic plasticity and the ability to adapt synaptic wiring, and thereby our capacity to process information and capture memories.

Zusammenfassung

Das Gehirn besteht aus einer Vielzahl von Nervenzellen, welche in Netzwerken organisiert sind und durch ihre Kommunikation die Grundlage für Gehirnfunktionen bilden. Neurone sind durch chemische Synapsen verbunden. Die präsynaptische Seite setzt durch Exozytose Neurotransmitter frei, welche von postsynaptischen Rezeptoren gebunden werden. Synapsen sind komplexe Strukturen bestehend aus einer Vielzahl von Proteinen, welche durch das Zytoskelett unterstützt werden. Die Strukturen der Synapse und des Zytoskeletts unterliegen einem ständigen Wandel und werden durch ein Gleichgewicht des Proteinaustauschs aufrechterhalten. Somit werden synaptische und zytoskelettäre Strukturen deutlich länger erhalten als die Lebenszeit der individuellen Proteine, aus denen sie bestehen. Eine Veränderung des synaptischen Gleichgewichts (Plastizität) führt zu Änderungen der synaptischen Stärke und der Wirksamkeit der Kommunikation zwischen Neuronen. Durch Stärkung (mehr oder stärkere Synapsen) oder Abschwächung (weniger oder schwächere Synapsen) der Konnektivität kann das neuronale Netzwerk den Aktivitätsfluss regulieren, Informationen verarbeiten und speichern.

Der Erhalt von Synapsen und insbesondere synaptische Plastizität erfordern Proteinumsatz. Neurone haben ein hoch entwickeltes Repertoire an Organellen, um Proteine produzieren, degradieren und recyceln zu können. Ein Teil dieser Organellen, hauptsächlich von geringer Größe, wird aktiv weit in distale Dendriten und Axone transportiert, was zur lokalen Unterstützung von Synapsen wichtig sein dürfte. Größere Organellen, z.B. ER und Mitochondrien, sind weniger mobil. Außerdem werden neue, im Soma synthetisierte Proteine, über aktive Transportprozesse zu weiter entfernten Synapsen transportiert. Dieser Transport erfolgt entlang des Zytoskeletts, das neben der Bereitstellung der Struktur die Wege für den aktiven Transport ebnet. Der Transport von Proteinen und Organellen insgesamt ist für die Unterstützung der zellulären Dynamik, einschließlich der synaptischen Dynamik, von wesentlicher Bedeutung.

Zu diesem Zweck führte ich Experimente mit folgenden Schwerpunkten durch: der Zytoskelettarchitektur im Nanobereich, den Signalwegen, die eine Veränderung dieser Zytoskelettorganisation herbeiführen können, sowie den Transport von Organellen, die Synapsen unterstützen könnten. Hochauflösende STED-Nanoskopie ergab, dass im Dendriten Aktinpatches vorhanden sind, die teilweise mit Synapsen assoziieren und dass der Hals der dendritischen Spines mit einem periodischen Aktinraster strukturiert ist. Dieses Aktinraster in Spines zeigt starke Ähnlichkeiten mit einem früher beschriebenen membranassoziierten Zytoskelett und könnte in diese Kategorie von Aktinstrukturen eingeordnet werden. Die Aktinpatches hingegen scheinen sich an exzitatorischen Schaftsynapsen zu befinden. Darüber hinaus haben fortgeschrittene lichtmikroskopische Versuchsreihen eine entscheidende Rolle des Calciumbindungsproteins Caldendrin bei der Steuerung der Dynamik von Aktin in Spines gezeigt. Caldendrin ist besonders während der synaptischen Stärkung als Ergebnis einer hohen synaptischen Aktivität und entsprechender erhöhter Konzentration an intrazellulärem Calcium von Bedeutung. Während dieses Prozesses schützt Caldendrin einen essentiellen Teil der Aktinstruktur, der eine stabile Grundlage für das Wachstum einer neuen Aktinanordnung bildet, und somit das Wachstum des Spineköpfchens ermöglicht.

Verschiedene Experimente zum Organellentransport haben gezeigt, dass filamentöse dendritische Aktinpatches den Transport stark beeinflussen indem sie Haltepunkte bilden. Diese verzweigten Aktinstrukturen sind in Dendriten verteilt, sind Teil von exzitatorischen Schaftsynapsen oder befinden sich an der Basis von dendritischen Spines. Lysosomen, hier als Modellorganelle verwendet, halten diesen Aktinpatches. Das Anhalten der Organellen wird durch Aktin als strukturelle Barriere und durch die Myosin-V-Aktivität vermittelt. Die genaue Funktion des Anhaltens von Organellen ist noch unklar. Es könnte sein, dass das Anhalten wesentlich ist, damit Organellen ihre Funktion auf bestimmte Orte konzentrieren können. Hierdurch könnten sie Synapsen an bestimmten dendritischen Abschnitten unterstützen, möglicherweise in Abschnitten mit hoher synaptischer Aktivität. Das Aktin-Zytoskelett könnte auch Organellenfusion, Reifung oder den Austausch von Proteinen vermitteln. Zukünftige Experimente könnten die genaue Funktion des Organellenstopps aufzeigen. Sie hängt möglicherweise direkt mit der Fähigkeit zusammen, die synaptische Stärke zu ändern und somit mit unserer Fähigkeit, Informationen zu verarbeiten und Erinnerungen zu bilden.

Contents

List of Figures	iii
List of Tables	v
Abbreviations	vii
1 General introduction	1
1.1 Brain and neuron communication	3
1.2 Clustered synaptic plasticity	5
1.3 The challenges of neuronal transport	7
1.4 The neuronal cytoskeleton	8
1.5 Aims of this thesis	13
2 The calcium binding protein caldendrin controls actin dynamics in the head of dendritic spines	15
2.1 Calcium signalling via caldenrin in neurons	17
2.2 Calcium binding opens the conformation of caldendrin and promotes the interaction with cortactin in dendritic spines	17
2.3 The influence of caldendrin knockout on dendritic and spine morphology	19
2.4 The function of caldendrin in controlling actin dynamics	21
2.5 The nano-organization of actin in spines of caldendrin knockout cultures	22
2.6 The function of caldendrin in the establishment of structural LTP	22
2.7 The function of caldendrin in dendritic spines	25
2.8 Materials and methods	27
3 Periodic F-actin structures shape the neck of dendritic spines	33
3.1 The actin cytoskeleton	35
3.2 The membrane-associated periodic actin skeleton	35
3.3 The MPS is found in the neck of dendritic protrusions	35
3.4 The dendritic protrusions can be categorized as dendritic spines	36
3.5 The spinous MPS shows strong similarities to the MPS in axons and dendrites	36
3.6 Actin, but not β -II spectrin, forms a periodic lattice all throughout the neck of spines	39
3.7 The periodic actin lattice in spine necks can be found in hippocampal tissue	40
3.8 Materials and methods	42

4 F-actin patches associated with glutamatergic synapses control positioning of dendritic lysosomes	45
4.1 The cytoskeleton organisation and its functions	47
4.2 Actin patches within the dendritic shaft	47
4.3 Actin patches are part of active excitatory synapses	47
4.4 Dendritic actin patches are dynamic actin structures, but their location is stable	49
4.5 Dendritic lysosomes are positioned close to microtubules and at actin patches .	52
4.6 Lysosomes are stalling at dendritic actin patches	54
4.7 What is the mechanism of lysosome stalling at dendritic actin patches?	55
4.8 Do dendritic actin patches influence all dendritic transport, and what is the role of synaptic activity?	58
4.9 Materials and methods	59
5 Expansion microscopy for high resolution imaging	65
5.1 Super-resolution light microscopy	67
5.2 Expansion microscopy	67
5.3 Expansion retention microscopy on cytoskeletal structures	68
5.4 Materials and methods	75
6 Discussion and perspective	79
6.1 Synopsis	81
6.2 Caldendrin and calcium signalling	81
6.3 The MPS in the neck of dendritic spines	82
6.4 Dendritic organelle transport	83
References	87
A Additional materials, methods, and protocols	99
A.1 Plasmid DNA preparation	99
A.2 Molecular cloning procedures	100
A.3 Preparation of chemical competent bacteria	103
A.4 Culturing procedures for standardized cell lines	104
A.5 Poly-L-lysine coating of coverslips for adherent cell culture	106
A.6 Preparation of primary rat hippocampal cell cultures	107
A.7 Preparation of organotypic hippocampal slice cultures	110
A.8 Immunocytochemistry	115
A.9 Expansion microscopy	116
B List of hazardous substances	119
Acknowledgements	134
Curriculum Vitae	137
Eidesstattliche Versicherung	141

List of Figures

1.1	Neuron, dendrite and synapse morphology	3
1.2	Clustered synaptic plasticity	6
1.3	Schematic illustration of the cytoskeleton and active intracellular transport	9
2.1	Activity dependent opening of caldendrin's conformation, and binding to cortactin in dendritic spines	18
2.2	The dendritic complexity of +/+ and caldendrin -/-neurons	20
2.3	Protrusion morphology in caldendrin +/+ and caldendrin -/- slices	21
2.4	Actin dynamics in spines of caldendrin +/+ and -/- cultures	23
2.5	The nanostructure of F-actin in spines of caldendrin +/+ and -/- cultures	24
2.6	Single spine structural LTP in caldendrin +/+ and -/- organotypic slice cultures	25
2.7	Model illustrating the function of caldendrin	26
3.1	Schematic illustrations of the MPS	36
3.2	A periodic actin lattice in the neck of dendritic protrusions	37
3.3	The dendritic protrusions are contacted by presynaptic sites	38
3.4	The MPS in dendritic spines is similar to the lattice in axons and dendrites	38
3.5	The F-actin lattice is more pronounced in spine necks than β -II spectrin	39
3.6	Phalloidin labels dendrites and spines in living hippocampal slices	40
3.7	The MPS can be found in the neck of spines in hippocampal slices	41
4.1	Super-resolution microscopy reveals the dendritic actin cytoskeleton at the nanoscale level	48
4.2	Development series of primary hippocampal neurons stained for a synaptic marker (bassoon), dendritic marker (MAP2), and the actin cytoskeleton (phalloidin)	49
4.3	Dendritic actin patches are part of functional excitatory shaft synapses	50
4.4	Time-lapse series of F-actin structures at a dendritic segment	51
4.5	F-actin turnover at dendritic patches and within the head of dendritic spines	52
4.6	The microtubule and actin cytoskeleton form segregated structures to which lysosomes associate	53
4.7	Analysis of lysosome mobility in proximity and away from actin patches	55
4.8	Illustration of the Matlab analysis of lysosomes mobility in proximity and away from actin patches	56
4.9	Actin induces stalling of lysosomes by forming a barrier or a binding location for vesicle associated myosins	57
5.1	Principles of expansion microscopy and fluorophore retention strategies	69
5.2	Survival of fluorophores upon gelation in an acrylamide gel	71

LIST OF FIGURES

5.3	Expansion microscopy applied for visualization of the cytoskeleton of COS-7 cells	72
5.4	Immunostainings visualizing podosomes, non-expanded and expanded	73
B.1	Globally harmonized system of classification and labelling of chemicals. Their symbols, numbers and summarized meaning	119

List of Tables

2.1	Constructs chapter 2	27
4.1	Constructs chapter 4	59
4.2	Primary antibodies	60
4.3	Secondary antibodies	60
5.1	Materials for ICC	75
5.2	Materials for expansion microscopy	76
5.3	Materials used for fluorophore survival analysis	77
A.1	Buffers for DNA mini prep	99
A.2	Standard PCR pipetting scheme	100
A.3	Standard PCR Protocol	101
A.4	Transformation buffer I	103
A.5	Transformation buffer II	103
A.6	Full medium	104
A.7	Dissection medium	112
A.8	Slice culturing medium	112
A.9	Gel solution	117
A.10	Digestion buffer	117
B.1	GHS Hazard statements	119
B.2	GHS precautionary statements	122
B.3	Response precautionary statements	123
B.4	Storage precautionary statements	126
B.5	Disposal precautionary statements	127
B.6	GHS substances used for the work presented in this thesis	128

Abbreviations

+/+	Wildtype
-/-	Knockout
ACSF	Artificial cerebrospinal fluid
AcX	Acryloyl-X, SE, 6- ((acryloyl)amino) hexanoic acid
AIS	Axon initial segment
AMPA receptor	α -amino-3-hydroxy-5-methyl-4-isoxazolepropionic acid receptor
ANOVA	Analysis of variance
Arp2/3	Arp2/3 protein complex
ATP	Adenosine triphosphate
bic	Bicuculline
cald	Caldendrin
CFP	Cyan fluorescent protein
CLSM	Confocal laser-scanning microscopy
decon.	Deconvolved
DIV	Day(s) <i>in vitro</i>
DMEM	Dulbecco's Modified Eagle Medium
DMSO	Dimethylsulfoxide
eGFP	Enhanced green fluorescent protein
EM	Electron microscopy
ER	Endoplasmic reticulum
FLIM	Fluorescence lifetime imaging microscopy
FRAP	Fluorescence recovery after photobleaching
FRET	Förster resonance energy transfer
G	Needle wire gauge
HBSS	Hank's balanced salt solution
HBSS (-/-)	HBSS without bivalent cations
ICC	Immunocytochemistry
LB	Lysogeny broth
LTD	Long-term depression
LTP	Long-term potentiation
MA-NHS	Methylacrylic acid N-hydroxysuccinimide ester
mCherry	Monomeric cherry (fluorescent protein)
MPS	Membrane-associated periodic actin skeleton
mut	(Ca ²⁺ -binding) mutant
N-WASP	Neural Wiskott-Aldrich syndrome protein
N/A	Not applicable
NA	Numerical aperture

ABBREVIATIONS

NMDA receptor	N-Methyl-D-aspartate receptor
ON	Overnight
PBS	Phosphate buffered saline
PCR	Polymerase chain reaction
PSD	Postsynaptic density
ROI	Region of interest
RT	Room temperature
SD	Standard deviation
SEM	Standard error of the mean
SIM	Structured illumination microscopy
SMLM	Single molecule localization microscopy
STED-microscopy	...	Stimulated emission depletion-microscopy
STORM	Stochastic optical reconstruction microscopy
TagBFP	Tag blue fluorescent protein
TIRF	Total internal reflection fluorescence (microscopy)
TTX	Tetrodotoxin
UV	Ultraviolet
WLL	White light laser
wt	Wildtype
YFP	Yellow fluorescent protein

1 General introduction

1.1 Brain and neuron communication

1.1.1 Neuron physiology

The brain enables us to receive and respond to environmental cues in a coordinated manner. 100 billion cells, named neurons, communicate with one another in functional networks to perform this function. Neurons are highly specialized cells, strongly molecular polarized and have a distinct morphological identity (Figure 1.1A). They are one of the few cell types that are excitable and connected via chemical synapses. The chemical synapses allow the transmission of information from one neuron to another. The brain includes various neuronal subtypes, each of them having a defined class of neurotransmitter, and distinct morphological and functional characteristics. Functionally the strongest difference is found between inhibitory and excitatory neurons. Excitatory neurons enhance activity in other neurons while inhibitory, as the name illustrates, inhibit the activity of others. Morphologically, neuronal subtypes vary from another based on their axonal and dendritic complexity, including large and detailed differences.

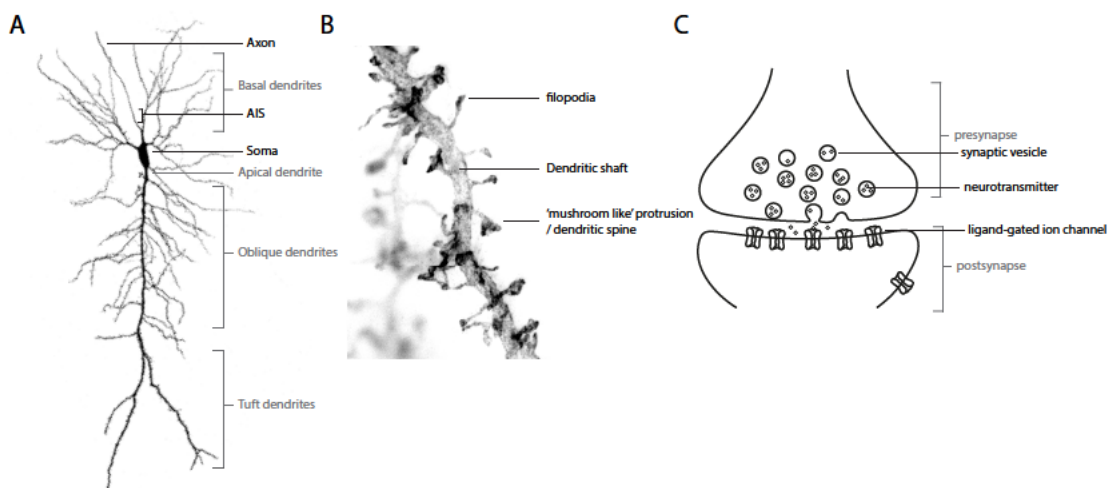


Figure 1.1: Neuron, dendrite and synapse morphology.

A. Fluorescence microscopy image of a typical excitatory pyramidal neuron. Names illustrate the different sections within a pyramidal neuron. The axon continues outside of the image window. Image is a maximum intensity projection of a confocal image stack containing images of different foci. The neuron was expressing the fluorescent protein mRuby2.

B. Fluorescence microscopy image of a dendritic segment (oblique dendrite) showing different morphologies of dendritic protrusion, including 'mushroom like' spines. Image was taken from an eGFP expressing pyramidal neuron imaged with a STED super-resolution microscope.

C. Schematic illustration of a chemical synapse. The presynapse contains synaptic vesicles filled with neurotransmitter. These synaptic vesicles can fuse with the presynaptic membrane, on which neurotransmitter is released within the synaptic cleft. In this moment, neurotransmitter can bind to ligand-gated ion channels (receptors) located in the postsynaptic membrane. This causes influx of ions and a depolarization of the postsynaptic contact; a propagation of a signal.

Neurons have in common that they are divided into three main compartments: the soma, the dendrites and a single axon (Figure 1.1A). The dendritic compartment is strongly branched and

offers place to postsynaptic sites, locations where neurons receive input from other neurons. The postsynaptic sites are located on the dendritic shaft or at little protrusions, named dendritic spines (Figure 1.1B). The axonal compartment is the output of the neuron, it harbours numerous presynaptic sites. The somato-dendritic and the axonal compartments are separated by the axon initial segment (AIS), located at the start of the axon, which functions as a barrier for intracellular transport thereby strongly contributing to cell polarization. The AIS also performs an essential function in cell excitability. It harbours different types of voltage sensitive ion channels which can induce action potentials; strong cellular depolarization and repolarisation of the cell; shortly changing the membrane potential from -70 mV up to +40 mV. The threshold for the initiation of an action potential is determined by the voltage threshold of the voltage-sensitive ion channels. This threshold can be reached by a summation of short-lasting depolarizing inputs coming from postsynaptic sites. In the summation, excitatory depolarizing inputs have to strongly out-compete inhibiting hyperpolarisations. As neurons integrate numerous inputs by strength and timing, neurons are sometimes pictured as small computational units that deliver one output via their axon (Mel et al. [2017]). Neuronal excitability and neuron-to-neuron communication via chemical synapses forms the basis of information processing and brain functioning.

1.1.2 Dynamics at excitatory synapses

Chemical synapses are either excitatory or inhibitory. Inhibitory synapses are mainly formed onto the dendritic shaft while excitatory synapses are mostly located on dendritic spines. Dendritic spines are small protrusions connected with a thin neck to the dendrites (Figure 1.1B). The neck separates the spine head, including a postsynaptic site, from the dendritic shaft. Dendritic spines can be found in a variety of morphologies, but the most prevalent shape in mature neurons is described as 'mushroom' like. The cytoskeleton forms the structural basis of spines (Korobova and Svitkina [2010]). The cytoskeleton provides binding places for scaffolding proteins; for proteins containing SH3 and multiple ankyrin repeat domains (e.g. SHANKs) and postsynaptic density (PSD) protein 95. These scaffolding proteins form the connection between the cytoskeleton and receptors positioned within the synapse (Bucher et al. [2019]).

Chemical synapses, that connect neurons, are highly dynamic. Synapses can form, become stronger, reduce strength or disappear with time. Highly active synapses tend to become stronger and persist longer, while less active synapses have a higher chance on elimination (Wiegert et al. [2018], Yang et al. [2009]). In addition, the pattern or interval of synaptic activations can have a strong influence on synaptic strength (Bi and Poo [1998]). Changes in synaptic strength, due to synaptic activity, is commonly referred to as synaptic plasticity.

Synaptic plasticity takes place both at the pre- and postsynaptic site. At the presynaptic site, the release of total neurotransmitter can change. This includes an increase or decrease in the quantal release probability of presynaptic vesicles (Yang and Calakos [2013]). These changes occur together with an overall alteration in bouton size, the part of the axon that harbours a presynaptic site (Chéreau et al. [2017]). Postsynaptic sites undergo physiological changes and strong structural remodelling when altering synaptic strength (Bosch et al. [2014], Harvey and Svoboda [2007], Matsuzaki et al. [2014]). The main driver of postsynaptic plasticity is calcium influx via the N-methyl-D-aspartate (NMDA) co-incidence receptor (Lüscher and Malenka [2012]). Calcium ions entering the cell trigger a plethora of signalling cascades. These signalling cascades

translate calcium elevations to alteration in the cytoskeleton (Bosch et al. [2014]). In case of synaptic strengthening, the cytoskeleton is strongly elaborated resulting in a larger spine. Most important changes take place at the PSD. The size of the PSD increases, which allows more receptors to reside within the synapse. Mostly increasing in number are α -amino-3-hydroxy-5-methyl-4-isoxazolepropionic acid (AMPA) receptors. The increase of AMPA receptors is the key feature of synaptic strengthening, as opening of more ionotrope receptors induces a stronger postsynaptic depolarizing current. In other words, the synapse is more likely to induce an action potential in the postsynaptic cell. The quantity of AMPA receptors residing within synapses correlates with synaptic strength, stronger synapses contain a higher number of AMPA receptors than weaker synapses (Lüscher and Malenka [2012]).

Tuning of synaptic strength is believed to underlie learning and memory formation (Takeuchi et al. [2014]). As memories are formed, it is thought that neurons form stronger and/ or more synaptic connections (Josselyn and Tonegawa [2020]). The elaboration of synaptic strength is reflected in higher probability that presynaptic neuron A activates postsynaptic neuron B, and the likelihood of a signal to propagate within a neuronal network. Changes in synaptic strength are essential in the formation of neuronal ensembles. Neuronal ensembles are groups of neurons that efficiently activate all together, which is proven to be essential for the retrieval of memories (Tonegawa et al. [2015], Denny et al. [2014], Kitamura et al. [2017], Josselyn and Tonegawa [2020]).

1.2 Clustered synaptic plasticity

1.2.1 The dendritic segment as unit of synaptic plasticity

Synaptic plasticity is often looked at as an event taking place at a single synapse, however it often involves the connected dendritic branch and other closely located synapses. The dendritic branch is extremely important for the coordination of plasticity processes. Activation of multiple synapses can locally depolarize a dendritic branch, which is sufficient to induce synaptic plasticity at synapses independently of neuron activation (Gambino et al. [2014], Rossato et al. [2018]). Moreover, precise studies of synaptic plasticity at dendritic segments have shown that synapses can share molecular resources. The activation of existing proteins and newly translated proteins coming from one synapse undergoing long-term potentiation (LTP), can lower the amount of activity required for LTP at another synapse (Govindarajan et al. [2011], Harvey and Svoboda [2007], Harvey et al. [2008], Murakoshi et al. [2011]). This phenomenon is observed in postsynaptic sites located maximally 10 μm apart, and named clustered synaptic plasticity. It suggests that dendritic segments can function as computational units for synaptic plasticity. These dynamics at dendritic segments, affecting synaptic strength, could guide the wiring of neuronal circuits.

1.2.2 Sharing of synaptic resources

The resources that are shared between synapses can be divided into two different groups: existing proteins that become activated and diffuse and newly translated proteins. By single synapse stimulation and fluorescence lifetime imaging microscopy - Förster resonance energy transfer

(FLIM-FRET) microscopy it is shown that the influx of calcium triggers the activation of different Rho-GTPases: RhoA, H-Ras and Cdc42 (Murakoshi et al. [2011]). These Rho-GTPases are mainly involved in the remodelling of the activated synapse, but not exclusively. Activated RhoA and H-Ras are found to diffuse out of the spine, via the dendritic shaft, into neighbouring spines (Figure 1.2). Depending on the spine density at the local dendritic segment, this can include 10 up to 20 spines. Their spread is spatially constricted by inhibitors, which inhibit the activity of Rho-GTPases and return them to their non-activated form (Oliveira and Yasuda [2014]). In neighbouring synapses, active RhoA and H-Ras reduce the amount of activity required for LTP. This might be an effect of priming the actin cytoskeleton for modification, and/or promoting additional insertion of AMPA receptors into the plasma membrane by exocytosis. The latter would primarily occur within the outer edges of spines and at the dendritic shaft, followed by AMPA receptor diffusion into the PSD (Park [2018]). The diffusion of proteins, promoting strengthening of synapses next to potentiated synapses, shows that plasticity events are strongly dependent on the local molecular environment.

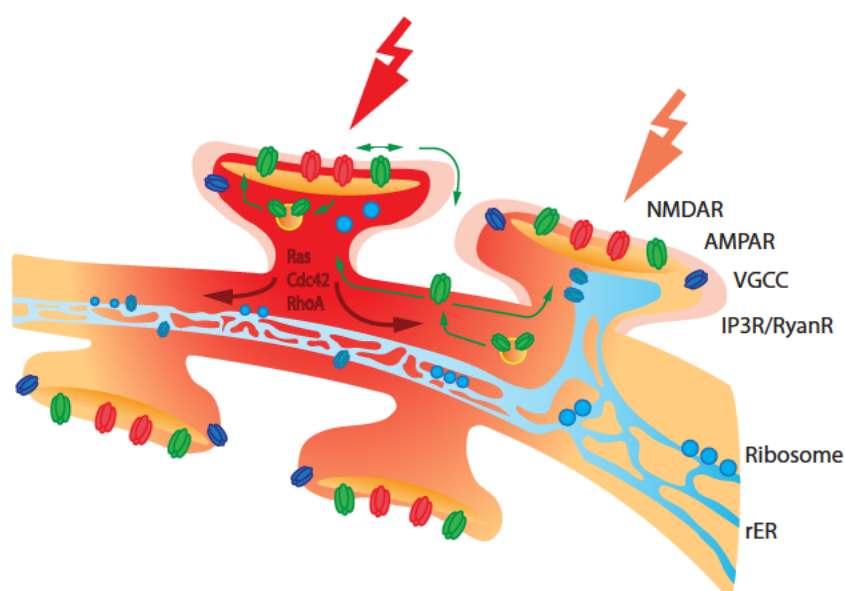


Figure 1.2: Clustered synaptic plasticity.

Illustration of a dendritic branch showing the known factors that are involved in clustered synaptic plasticity. Activity at one synapse can influence the probability for potentiation in another, by lowering the required amount of activity for LTP (indicated by the orange arrow). This phenomenon is observed in up to 10 μm dendritic stretches from a strongly stimulated spine (red arrow). Illustrated in red is the diffusion of activated Ras and RhoA.

NMDAR - NMDA-receptor, AMPAR - AMPA-receptor, VGCC - voltage-gated calcium channels, IP3R/RyanR - Inositol triphosphate receptor/ Ryanidine receptor, rER - rough endoplasmatic reticulum.

Image from (van Bommel and Mikhaylova [2016]).

The diffusion of active proteins is not the only factor of importance in clustered synaptic activity. The transition of synaptic strengthening into LTP requires the translation of new proteins (Govindarajan et al. [2011]). The need for protein synthesis was illustrated by inhibiting protein translation, which results in a loss of lasting synaptic potentiation (Govindarajan et al. [2011]).

Proteins supporting LTP can originate from local protein translation within dendrites. Strong plasticity inducing activation of a single synapse is sufficient for the induction of dendritic protein translation. The resulting proteins help the according synapse to maintain its increase in strength (LTP). This strengthening can be observed as an increase in AMPA receptors and structural enlargement of the spine. In an event that two nearby synapses receive similar LTP inducing stimuli, they start to compete for resources. The translated proteins have to be shared, and this is reflected in a smaller structural increase of both spines. Nonetheless, both synapses become long-term strengthened. In addition, an interesting observation is that one synapse can use the translated proteins of another spine to transition from short-lasting to long-lasting potentiation (Govindarajan et al. [2011]). This promotes the overall strengthening of synapses at dendritic segments. The observation illustrates that synapses, even though compartmentalized on spines, can affect one another on a molecular basis.

These observations, summarized by the term clustered synaptic plasticity, indicated that local physiological and molecular events can influence synaptic strength. Interestingly, most processes discovered so far illustrate a collaborative increase of synaptic strength rather than long-term synaptic depression (LTD). Assuming that clustered plasticity mainly facilitates synaptic strengthening, the processes of clustered plasticity has the potential to strongly enhance synaptic strength at dendritic segments. This could increase the power of dendritic segments to induce spiking of the neuron, in other words their computation weight. Molecular dynamics at dendritic segments might largely influence synaptic strength and thereby neuronal wiring, and could play an important role in how neurons encode memories.

1.3 The challenges of neuronal transport

Neurons are highly polarized cells with a complex architecture. Their large dendritic arbour and long extended axons makes them span large areas compared to other cell types. Their polarization and the requirement to maintain a high number of chemical synapses create many intracellular challenges. One of them is the continuous supply of synaptic proteins to maintain synapses. Neurons have complex systems to maintain a protein pool for the exchange of proteins at rather stable structures. This is required as the lifetime of proteins is generally shorter than the existence of synapses. Local protein amounts can be maintained by local translation and/or recycling at dendritic segments, or proteins can be newly brought-in from the soma by molecular transport (Govindarajan et al. [2011], Mikhaylova et al. [2016]). The latter mostly applies to transmembrane proteins. Transmembrane proteins are translated by ribosomes located on the rough endoplasmic reticulum, which is followed by the introduction of post-translational modifications at the Golgi apparatus. Thereafter, cargoes are transported into the axon or dendritic tree by molecular transport.

This raises several questions: How do cargoes/ organelles containing these proteins find their way to the specific locations, which factors determine their transport, and does synaptic plasticity have an influence on the transport? One important factor is the organization of the F-actin and microtubule cytoskeleton. The cytoskeleton does not only offer mechanical strength to neurons, but also functions as the paths for molecular transport (Figure 1.3).

1.4 The neuronal cytoskeleton

1.4.1 The microtubule cytoskeleton

Microtubules consist of dimers of alpha- and beta tubulin, which together form protofilaments [Alberts et al. [2008]]. The protofilaments together create a tubular structure, which is the microtubule (Figure 1.3). Microtubules are dynamic at their, so called, plus end. The plus end can incorporate alpha/beta tubulin dimers and grow, or fall apart and shrink (catastrophe). The dynamics are regulated by microtubule plus end binding molecules. The minus end is mostly stable, and associated with the microtubule organizing centre. Interestingly, in neurons the microtubule organizing centre disappears during development and microtubule minus ends are stabilized by minus-end binding proteins [Hendershott and Vale [2014], Jiang et al. [2014]]. In neurons, new microtubules are created by severing enzymes that break existing microtubules into two, which creates an additional plus-end for microtubule growth.

The microtubule cytoskeleton includes both dynamic and stable microtubules. Most studies on microtubule polarity focus on dynamic microtubules, since there are excellent tools available for study [Honnappa et al. [2009]]. The polymerization of microtubules can be visualized in great detail by expression of fluorescently tagged plus-end binding proteins. These proteins accumulate at the polymerizing plus-end and form a clear beacon for microtubule polymerization. Even though these tools provide a great tool to study microtubule dynamics, they do not show the stable microtubule cytoskeleton. There is a large proportion of microtubules that remain stable for longer time periods (>1 hour). Stable microtubules contain post-translational modifications as acetylation and detyrosination [Schulze et al. [1987]]. However, acetylation and detyrosination are a feature of, but do not stabilize microtubules. Why some microtubules are stable and while others are not is unclear [Yu et al. [2015]]. This deserves further study as it is very likely that stable and unstable microtubules perform different intracellular functions.

In neurons, the axonal and dendritic compartments have a very differently organized microtubule cytoskeleton. In the axon, microtubules are oriented with the plus-end away from the soma (plus-end out). In dendrites the microtubules have a mixed polarity, plus-end in and plus-end out [Yau et al. [2016]]. In general, microtubules are organized in bundles with a uniform polarity [Tas et al. [2017]]. Occasionally polymerizing microtubules extend into spines, but its function remains unclear [Schätzle et al. [2018]].

Microtubules are important structures for cellular transport. They form the paths for active transport by motor protein complexes that transport cellular cargo over long-range. There are many factors that can influence the cargo transport. Depending on the type of motor complex, cargoes can be transported towards the plus- or minus-end of microtubules. Thus, the differential organization of microtubules in the axon versus dendrites has strong implications on cellular transport. Moreover, microtubule associated proteins, microtubule post-translational modifications and most likely tubulin isoforms can influence the affinity of motor proteins to microtubules [Kaul et al. [2014], Sirajuddin et al. [2014]]. The organisation of the microtubule cytoskeleton including the directionality and modifications is referred to as the 'tubulin code', which is highly complex, and how it affects transport has been topic of many studies [Janke and Kneussel [2010], Yu et al. [2015]].

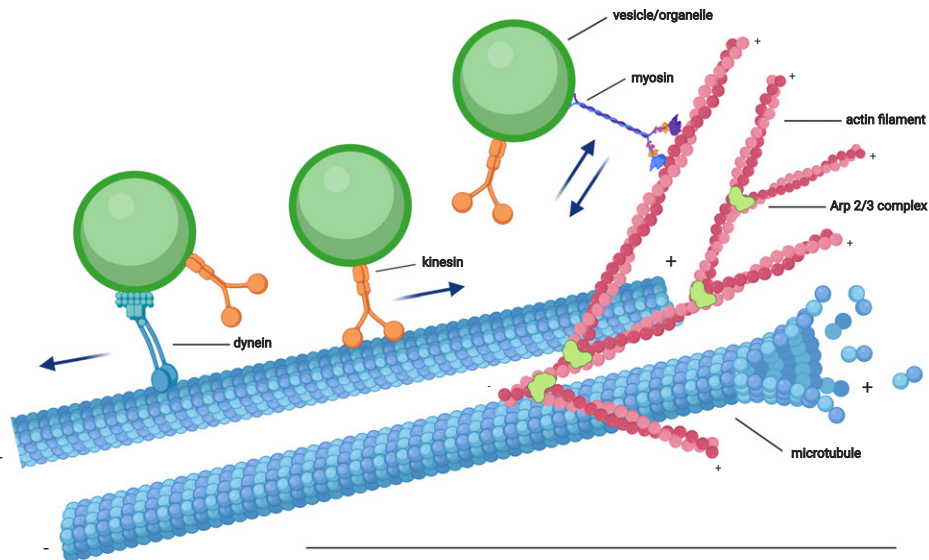


Figure 1.3: Schematic illustration of the cytoskeleton and active intracellular transport.

Microtubules and actin filaments form the paths for active intracellular transport. Microtubules form long hollow tube structures, actin can form a strongly branched network. Kinesins and dyneins transport cargoes over longer distances along microtubules. Local transport and positioning can take place by myosins, which walk slower and follow actin filaments. Myosins are stronger motors than kinesins and dynein.

This image is created with Biorender.

1.4.2 The actin cytoskeleton

The actin cytoskeleton is more dynamic than the microtubule cytoskeleton. It plays an important role in dynamic processes observed in neurons and is especially enriched in four major structures: in growth cones, in dendritic spines, in the AIS and along the plasma membrane.

Early in development, during cell differentiation, neurons grow their axon and dendrites. The growth of these protrusions is steered by guidance cues. Guidance cues can be gradients of extracellular molecules or adhesion molecules present on other cells (Purves et al. [2012]). These cues are sensed by receptors on the growing protrusions. Growing protrusions develop a 'hand' like structure with 'finger' like extensions to explore the environments. The overall structure is supported by the actin cytoskeleton. Actin polymerization drives the extension of the growth cone and its 'fingers'. Positive cues promote while negative cues inhibit actin polymerization; hereby growth is guided towards a specified direction (Omotade et al. [2017]). The guidance of growth cones by the modulation of the actin cytoskeleton is crucial for establishing the fundamental, coarse wiring of the brain.

In mature neurons, the actin cytoskeleton shapes and supports dendritic spines. The neck of dendritic spines contains longitudinal actin filaments, while the spine head is enriched with a branching actin meshwork (Korobova and Svitkina [2010]). Spinous actin forms paths for short-range transport via myosins, which is required to move cargoes in and out of dendritic spines (Esteves da Silva et al. [2015], Wang et al. [2008]). Actin within the outer layers of the spine head displays strong dynamics, and forms a strongly branched actin meshwork that provides

stability to the spine head (Korobova and Svitkina [2010], Frost et al. [2010], Hotulainen and Hoogenraad [2010]). The size of spines is maintained by an equilibrium in actin polymerization and depolymerization. The equilibrium can be changed by synaptic plasticity inducing stimuli. Robust remodelling and the establishment of a new structure and equilibrium, as during LTP, is guided by the activation of multiple signalling cascades. Downstream of these signalling cascades are proteins that sever, elongate or promote branching of actin filaments (Konietzny et al. [2017]). During the first steps of actin remodelling, severing of actin branches takes place by the protein cofilin. The re-establishment of new actin structures is mainly performed by formin, promoting elongation of actin filaments, and neural Wiskott-Aldrich syndrome protein (N-WASP) and the actin-related protein(s) 2/3 complex (Arp2/3) promoting actin branching (Figure 1.3). The new larger structure provides more space for synaptic scaffolding proteins and ligand-gated ion channels, thereby supporting a stronger synaptic connection.

High concentration of actin can also be found in the AIS, where it performs a filtering function for active cellular transport. The filtering is achieved by a branched actin network. The AIS separates axonal- from dendritic cargoes, as it stalls dendritic cargoes via the motor protein myosin V (Janssen et al. [2017]). An interaction of myosin V located on the vesicle with the actin network makes dendritic cargoes stall. Eventually, the cargoes are redirected via microtubule based transport into the dendrites (Franker et al. [2016]). The presence of actin as a filter is crucial for the maintenance of neuronal polarity.

The introduction of super-resolution light microscopy led to discovery of a previously unseen actin structure in neurons summarized by the name: the membrane-associated periodic skeleton (MPS, He et al. [2016], Xu et al. [2013], Zhong et al. [2014]). First findings reported the presence of the MPS in axons, later it was also found in the soma and dendrites (Han et al. [2017]). The MPS includes small longitudinal actin fragments capped by the protein adducin. In the axon and dendrites the MPS forms rings. Each ring is approximately spaced 180-190 nm apart. The spacing between the rings originates from the size of two β - spectrin dimers located in between. In the soma, the MPS displays a hexagonal pattern (Han et al. [2017]). This hexagonal pattern is also found in erythrocytes where it was discovered early by electron microscopy (Byers and Branton [1985], Shen et al. [1986]). The function of the MPS is not yet fully clarified, but based on the estimated stiffness of actin rings it is thought that the MPS provides rigidity to the plasma membrane (Leite et al. [2016], Smith et al. [2018]). The MPS will be further discussed in Chapter 3.

Taken together, the actin cytoskeleton is essential in neurons. It forms crucial structures, such as the AIS and dendritic spines. It defines and maintains neuronal polarity by orchestrating active transport, and at the same time, forms dynamic structures prone to remodelling by synaptic activity (Bosch et al. [2014], Janssen et al. [2017], Mikhaylova et al. [2018]). Dynamics in the F-actin cytoskeleton are essential for synaptic plasticity, and help to define how neurons are integrated within the neuronal network.

1.4.3 Motor proteins

Protein transport in neurons depends on active motor-based and passive diffusional transport. Active, adenosine triphosphate (ATP) dependent transport takes place by motor proteins along cytoskeletal structures. Most cargoes contain multiple motor proteins which are connected to the

cargo by adapter molecules (Fu and Holzbaur [2014]). The cytoskeleton environment around the cargo, the present adaptor proteins and motors on the cargo, and motor-motor competition determines the transport directionality (Schroeder III et al. [2010]). Motor proteins come in many different forms but are subdivided into three major classes. The kinesins and dyneins which run along microtubules, and myosins that use actin filaments (Figure 1.3).

The class of kinesins contains 14 different subfamilies (Endow et al. [2010]). Each of the kinesins has diverse characteristics and most likely contributes to transport in a slightly different manner. Overall, their protein structure consist of a motor domain, a stalk and a cargo binding domain. Kinesins form functional motors by dimerization. The dimers are formed via the coiled-coil domains located within the stalk region. Dimers can associate with microtubules by the motor region. When bound by ATP, the motor domains have a high affinity for microtubules. When the ATP is hydrolysed, the affinity is weakened which leads to a dissociation. By alternating ATP binding and ATP hydrolysis by the two motor domains, a kinesin motor dimer performs a 'stepping' motion along the microtubules. Generally speaking, most kinesins walk towards the plus-end of microtubules. The activity of kinesin motor dimers is further coordinated by regulatory proteins which interact with the stalk and cargo-binding domain, can phosphorylate and or forms the bound cargo itself (Verhey and Hammond [2009]).

Transport to the minus end of microtubules is performed by the dynein complex (Jaarsma and Hoogenraad [2015]). Dynein contains two major components: two dynein heavy chains and dynactin, a regulatory protein responsible for cargo binding and processive motion. Similar to kinesins, the dynein complex performs a 'walking' motion along microtubules and requires binding to a cargo adapter for activity. BICD2 is one of the most frequent cargo binding adapters and sometimes considered to be part of the dynein complex (Jaarsma and Hoogenraad [2015]), while other adapters are also known. In addition to cargo transport, the dynein complex is also known to orchestrate the organisation of the Golgi-network located in the soma (Burkhardt [1998]). Together kinesins and dynein are responsible for all active transport along microtubules.

Transport along actin filaments is performed by myosins (Kneussel and Wagner [2013]). Two unconventional myosins, myosin V and VI, are responsible for the cargo trafficking whereas other family members play a role in the organization of the F-actin cytoskeleton, by cross-linking or sliding actin filaments along each other. Myosin V activity is pronounced in spines and the AIS. This motor walks to the plus-end of actin filament and transports cargoes from the dendritic shaft into spines (Hammer and Wagner [2013], Wang et al. [2008]). Opposing is myosin VI, walking to the minus-end of microtubules. Myosin VI can transport cargoes out of spines dendritic spines (Esteves da Silva et al. [2015], Wagner et al. [2019]). The transport speed of the processive myosins is considerably lower than that of kinesins and dyneins. Based on the speed of myosins, the length as well as complexity of actin structures, it is believed that processive myosins are providing short range transport.

1.4.4 The complexity of transport in neurons

Neuronal transport is multifaceted and highly regulated. Transported cargoes are bound by a multitude of motor proteins, each interacting with the local environment in their own manner. The bound motor proteins can actively transport the cargoes along the cytoskeleton, or passively

travel with it. Active motor proteins can also compete with each other, which is named 'tug-of-war' (Derr et al. [2012]). A tug-of-war can result in complex behaviour of the transported cargo. It can influence the speed of transport or completely stall transport, preventing it from entering certain regions; such as the axon. Which motor protein is active is fully dependent on the surrounding molecular environment. This includes local ion concentration, the presence/absence of active signalling molecules, phosphorylation of the motor as well its adapter protein, and the organisation of the cytoskeleton (Fu and Holzbaur [2014], Janke and Kneussel [2010], Yu et al. [2015]). Each motor protein has its preference for cytoskeleton components, sometimes with specific post-translational modifications. These modifications can guide cargoes towards or away from specific cellular regions. In neurons, as excitable cells, local fluctuations in ion concentration can also influence motor proteins. For example, the activity of myosins is influenced by calcium and proteins in downstream signalling cascades, such as calmodulin (Batters et al. [2016], Krementsov et al. [2004]). The multitude of factors that influence cellular transport make it a difficult to predict and study process.

1.5 Aims of this thesis

The focus of this thesis is the organisation of the cytoskeleton and cellular transport in neurons. Actin shapes spines, and contributes strongly to the organization of the dendritic arbour. In my work, I focus on the nano-structural organization of the actin cytoskeleton in dendrites, with the goal to understand biological processes that contribute to synaptic maintenance and plasticity. This includes the transport of organelles along the cytoskeletal paths. To achieve this goal, I aim

1. to provide a better understanding of the F- actin nanostructure within the dendritic arbour.
2. to obtain a better insight in how calcium elevations are translated to F-actin reorganization in dendritic spines.
3. to understand the factors that organize molecular transport in dendrites, with the focus on the actin cytoskeleton and lysosomes as a model cargo.

2 The calcium binding protein caldendrin controls actin dynamics in the head of dendritic spines

This work is part of the scientific publication:

Caldendrin directly couples postsynaptic calcium signals to actin remodeling in dendritic spines

Marina Mikhaylova*, Julia Bär*, Bas van Bommel, Philipp Schätzle, PingAn YuanXiang, Rajeev Raman, Johannes Hradsky, Anja Konietzny, Egor Y. Loktionov, Pasham Parameshwar Reddy, Jeffrey Lopez-Rojas, Christina Spilker, Oliver Kobler, Syed Ahsan Raza, Oliver Stork, Casper C. Hoogenraad and Michael R. Kreutz

Neuron, 2018

**These authors contributed equally*

Contribution of others in the work stated here:

Dr. Marina Mikhaylova and Dr. Julia Bär helped with performing the FRAP experiments. Dr. Julia Bär traced the neurons for Sholl analysis. Dr. Marina Mikhaylova acquired the STED images with technical assistance of Oliver Kobler. I thank all authors contributing to the final publication that put the experiments presented here in frame, and their contribution to discussions during the project.

2.1 Calcium signalling via caldendrin in neurons

Calcium is one of the most important signalling ions in neurons. In polarized condition (-65 mV) calcium levels in neurons remain at low levels (< 100 nM), due to the active clearance of calcium ions from the cytoplasm by ion pumps (Clapham [2007]). Calcium levels can become elevated as result of synaptic activity and cellular depolarization, either within the entire neuron or confined within dendritic spines or dendritic segments (Sabatini et al. [2002]). These elevations in calcium are sensed by calcium binding proteins such as calmodulin and caldendrin that trigger downstream signalling pathways affecting cell homeostasis, including the regulation of cytoskeleton dynamics and protein translation (Bosch et al. [2014], Kaushik et al. [2014], Mikhaylova et al. [2018]).

In neurons caldendrin is one of the calcium binding proteins. Previous work was focussed on the biochemical properties of caldendrin and its interaction partners. Experiments highlighted that caldendrin contains four EF hand domains, of which three are able to bind calcium (Mikhaylova et al. [2006]). The second domain is cryptic and does not bind calcium. When calcium binds, caldendrin opens its conformation exposing a proline-rich N-terminus. This N-terminus forms a place for interaction with other proteins containing an SH3- domain (Mikhaylova et al. [2018]). This includes the F-actin binding protein cortactin. Caldendrin in a open conformation can bind cortactin. Together caldendrin and cortactin can bind actin filaments, probably changing dynamics. In this work I focussed on the role of caldendrin in neurons with the aim to understand how caldendrin-cortactin signalling is involved in (actin) dynamics at dendritic spines.

2.2 Calcium binding opens the conformation of caldendrin and promotes the interaction with cortactin in dendritic spines

To test whether caldendrin can activate and bind cortactin in spines, we performed FRET-acceptor bleaching experiments with fluorescently tagged caldendrin and cortactin. Here we used CFP/ YFP and eGFP/ mCherry FRET pairs with overlapping emission-excitation spectra. When in close proximity, energy of the donor fluorophore (CFP/ eGFP) can be transferred to the acceptor fluorophore (YFP/ mCherry), resulting in lower fluorescence of the donor and excitation of the acceptor. One method of measuring the FRET efficiency is photobleaching the acceptor and measuring the fluorescence of the donor. When the acceptor is photobleached, energy can no longer be transferred to the acceptor and the fluorescence of the donor will increase. The increase in fluorescence intensity after photobleaching, relative to the post-bleaching fluorescence intensity represents the FRET efficiency. Here we photobleached YFP/ mCherry to study the FRET efficiency in different experimental groups.

From previously performed experiments, using HEK cells, we know that in absence of calcium caldendrin displays strong FRET efficiency with a CFP located at the N-terminus and a YFP at the C-terminus (Mikhaylova et al. [2018]). When calcium bound, caldendrin opens its conformation and the FRET efficiency declines. We performed a similar experiment in neurons

2 THE CALCIUM BINDING PROTEIN CALDENDRIN CONTROLS ACTIN DYNAMICS IN THE HEAD OF DENDRITIC SPINES

to see if caldendrin unfolds as result of synaptic activity. CFP-caldendrin-YFP was overexpressed in caldendrin knockout neurons, subsequently the neuronal cultures were either silenced using tetrodotoxin (TTX) or activity was promoted by reducing neuronal inhibition with bicuculline application. In both groups the YFP was photobleached in dendritic spines and the increase of CFP fluorescence was measured. The measured FRET efficiency was on average lower in the bicuculline stimulated cultures compared to TTX silenced neurons (Figure 2.1A,B). This indicates that synaptic activity and corresponding calcium influx can induce an open active conformation of caldendrin.

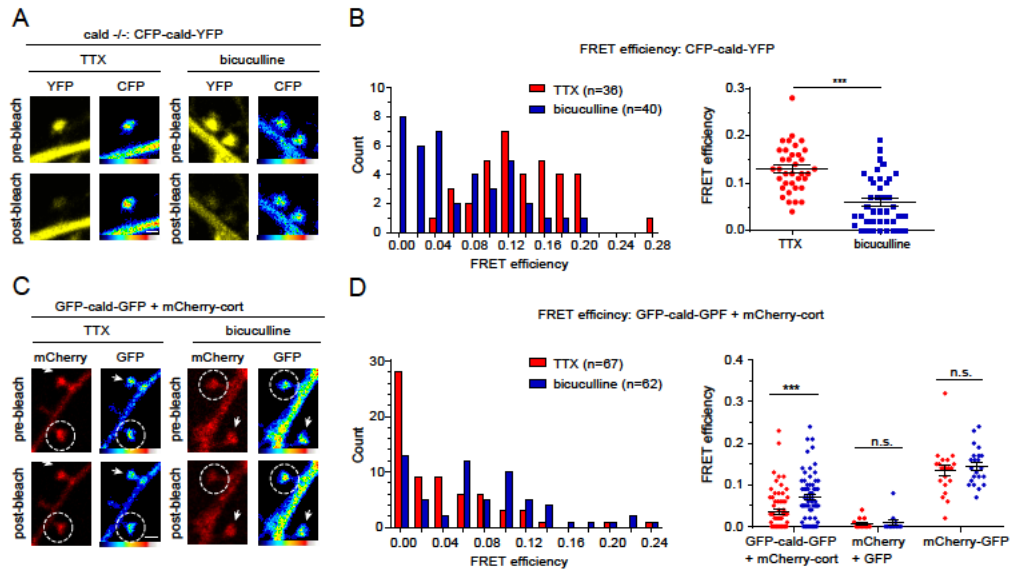


Figure 2.1: Activity dependent opening of caldendrin's conformation, and binding to cortactin in dendritic spines. A) Examples of a FRET experiment with fluorescently tagged caldendrin in spines from silenced (TTX) and activated (bicuculline) neuronal cultures. FRET efficiency is calculated from the fluorescence intensity of CFP after photobleaching of the acceptor (YFP). A lower FRET efficiency indicates an open conformation of caldendrin. Scale bar: 1 μ m. B) Quantification of the experiments shown in panel A. Spines in stimulated neuronal cultures show on average a lower FRET efficiency than spines in TTX silenced cultures. Synaptic activity, and corresponding calcium signalling, opens the conformation of caldendrin in spines. Right: mean FRET efficiency \pm SEM. Unpaired, 2-tailed Student's t test. *** $p < 0.001$. $N = 2$. n numbers (spines per group) provided in figure. C) Examples of a FRET experiment showing the interaction of eGFP-tagged caldendrin with mCherry-tagged cortactin. FRET efficiency was measured by the fluorescence intensity of eGFP signal after photobleaching of the mCherry acceptor. A high FRET efficiency indicates a more pronounced interaction between caldendrin and cortactin. The experiments were performed in TTX silenced and bicuculline activated neuronal cultures. The circle indicates the photo-bleached spine. The arrow indicates a control spine. Scale bar: 1 μ m. D) Quantification of the experiments shown in panel C. Activation of the neuronal culture yields on average a higher FRET efficiency between caldendrin and cortactin, indicating a more pronounced interaction between caldendrin and cortactin. Right: mean FRET efficiency \pm SEM. Unpaired, 2-tailed Student's t test. *** $p < 0.001$. $N = 2$. n numbers (spines per group) provided in figure.

In addition, we studied if the open conformation of caldendrin promotes its binding to cortactin within dendritic spines of living neurons. Here caldendrin was tagged on the N- and C-terminus with eGFP. Cortactin was tagged on the N-terminus with the fluorescent molecule

mCherry. When the proteins come in close proximity, eGFP (donor) and mCherry (acceptor) can display FRET. The FRET efficiency was analysed by photobleaching of mCherry and measuring the increase in fluorescence of eGFP. Silenced cultures (TTX) were compared to stimulated cultures (bicuculine). Stimulated cultures displayed on average a stronger FRET efficiency, indicating that caldendrin binds cortactin in a calcium dependent manner in dendritic spines (Figure 2.1C,D).

The experiments employing FRET acceptor bleaching show that synaptic activity and subsequent calcium influx is able to induce a conformational change in caldendrin. This opening of caldendrin exposes its proline-rich N-terminus by which caldendrin interacts with cortactin. By this pathway elevations in calcium levels, as result of synaptic activity, can be translated towards actin dynamics. Hereby caldendrin could play an important role in the regulation of actin dynamics and structural organization of dendritic spines.

2.3 The influence of caldendrin knockout on dendritic and spine morphology

Based on the previously acquired interaction data we hypothesized that spine morphology could be affected in the absence of caldendrin, since dendritic spines are known to depend strongly on the actin cytoskeleton and experience strong alterations in calcium levels. To study the morphology of dendrites and spines, individual neurons were transfected with a plasmid encoding mRuby2 (a fluorescent protein in the red spectrum) by single cell electroporation in organotypic slice cultures from caldendrin wildtype (+/+) and knockout mice (-/-). First, we cultured the slices for approximately two weeks, the age at which the slices are considered to be fully developed and have a stable connectivity. Around the second week, we transfected single neurons and let them express mRuby2 for a few days before fixation. Subsequently, the samples were mounted and imaged using confocal microscopy.

We started by studying the overall morphology of the neurons. In maximum intensity projections at a relative low magnification, the dendrites of the transfected neurons were traced in ImageJ. Sholl analysis, a method for quantification of dendritic complexity, showed no differences between neurons of caldendrin +/+ and -/- neurons (Figure 2.2 A,B). The dendritic length of the basal dendrites, the apical dendrites and the total dendritic length are identical between the two groups (Figure 2.2 C). A small difference was observed in the radius of the basal dendrites (Figure 2.2 D). The basal dendrites of knockout neurons span over a smaller area, this however does not have a direct physiological implication. Overall we found no major differences between caldendrin +/+ and -/- neurons regarding the complexity of the dendritic tree.

In the same set of samples we studied the morphology of dendritic protrusions. Three dimensional microscopy images were acquired at a higher magnification and 3D reconstructed to discriminate between morphologies (Figure 2.3). We imaged dendritic protrusions on segments of both basal and apical dendrites. Protrusions on the dendrites were categorized into filopodia and spines. Filopodia are small long protrusions, while spines display a 'mushroom' like shape with a so-called spine head. The distinct discrimination parameters used for the analysis can be found in the material and methods section. It is believed that spines form the basis for stronger synaptic connections, while filopodia are newly developing spines. It is important to keep in

2 THE CALCIUM BINDING PROTEIN CALDENDRIN CONTROLS ACTIN DYNAMICS IN THE HEAD OF DENDRITIC SPINES

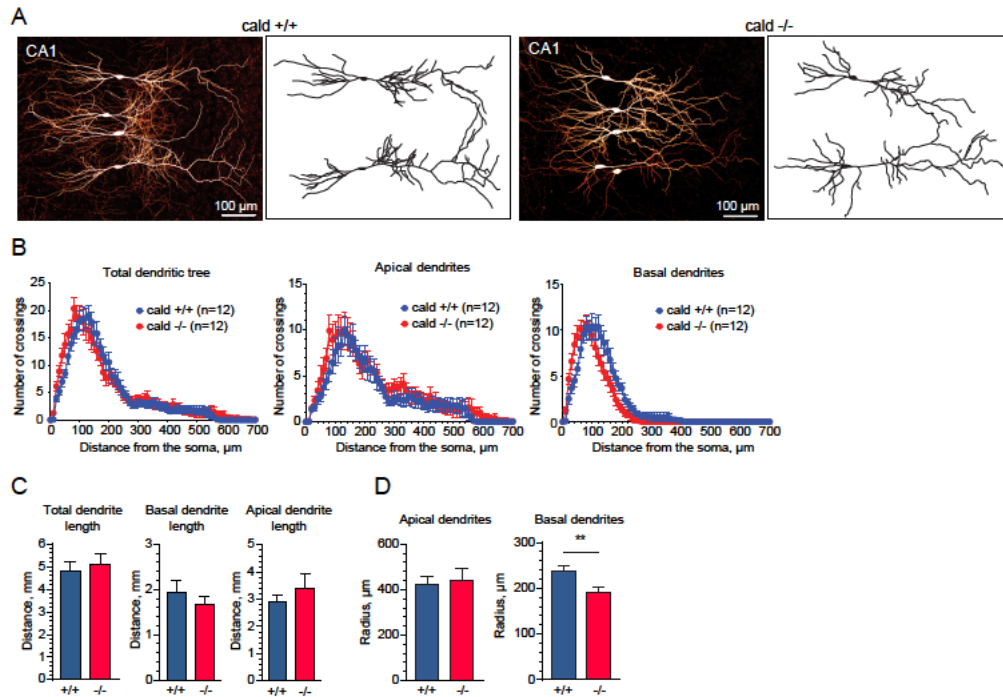


Figure 2.2: The dendritic complexity of +/+ and caldendrin $-/-$ neurons.

A) Electroporated CA1 hippocampal neurons in caldendrin +/+ and caldendrin $-/-$ organotypic slices. Neurons express the fluorescent protein mRuby2, which shows their morphology. Pyramidal neurons were traced for further Sholl analysis.

B) Complexity of the total dendritic tree, separated by apical and basal part, analysed by Sholl analysis. Knockout of caldendrin has no significant influence on the complexity of the dendritic tree. Repeated measures, 2-way ANOVA. N = 2 mice +/+, 4 mice $-/-$, 6 and 7 organotypic slices, and 12 neurons each.

C) Quantification of dendritic length. Dendritic length is not significantly different between caldendrin +/+ and caldendrin $-/-$ neurons. Data is represented as mean + SEM. Unpaired, 2-tailed Student's t-test. N = 2 mice +/+, 4 mice $-/-$, 6 and 7 organotypic slices, and 12 neurons each.

D) Analysis of the radius of the apical and basal dendrites. The radius of basal dendrites is slightly reduced in caldendrin $-/-$ neurons. Data is represented as mean + SEM. Unpaired, 2-tailed Student's t-test, ** p < 0.01. N = 2 mice +/+, 4 mice $-/-$, 6 and 7 organotypic slices, and 12 neurons each.

mind that the strict discrimination between filopodia and spines is defined by the set parameters in the study, within the data set there could be a smooth transition of spine morphologies from one group to the other.

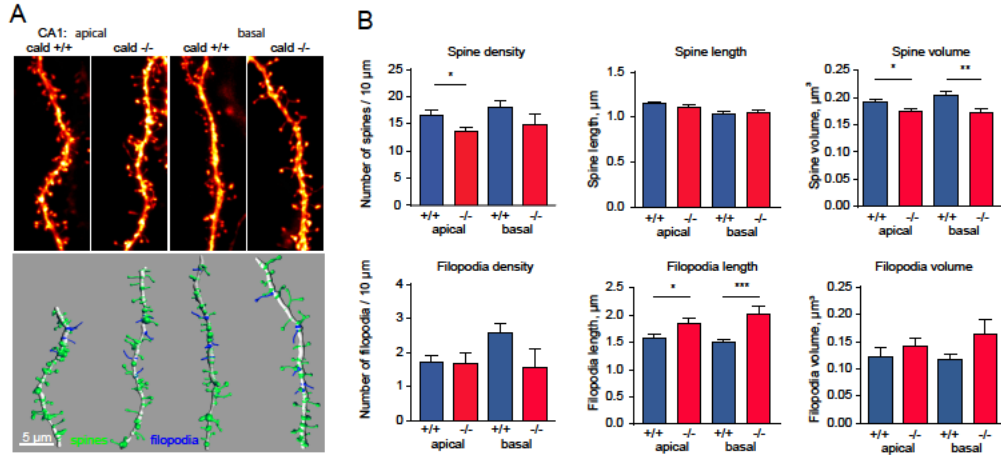


Figure 2.3: Protrusion morphology in caldendrin +/+ and caldendrin -/- slices.

A) Top, examples of dendritic segments used to study the morphology of dendritic protrusions. Dendritic segments and protrusions are visualized by expressing the fluorescent protein mRuby2. Bottom, reconstructed segments using Imaris software (Bitplane).

B) Quantification of protrusion density and morphology. Spine density and volume are reduced in caldendrin -/- neurons. Filopodia length is increased and filopodia volume shows a trend towards an increase. Data is represented as mean + SEM. * $p < 0.01$, ** $p < 0.01$, *** $p < 0.001$. n numbers are for spine density measures $n = 16$ apical -/-, $n = 12$ apical +/+, $n = 7$ basal -/-, and $n = 10$ basal +/+ dendritic segments, for spine characterization $n = 696$ apical -/-, $n = 577$ apical +/+, $n = 345$ basal -/-, and $n = 543$ basal +/+, and for filopodia characterization $n = 86$ apical -/-, $n = 60$ apical +/+, $n = 37$ basal -/-, and $n = 77$ basal +/+. From identical mice and organotypic slice number as in Figure 2.2.

A comparison between dendritic segments of caldendrin +/+ and caldendrin -/- neurons shows differences in the morphology of protrusions (Figure 2.3). In caldendrin -/- spines are smaller and the overall spine density is decreased. The filopodia length is increased. Also, the filopodia volume and density show a tendency to an increase. Overall, it seems that the absence of caldendrin reduces the volume of spine heads, so that spines have a smaller volume and some of spines become categorized as filopodia. The calcium dependent activation of caldendrin and binding of cortactin might be very important for the formation and/ or maintenance of spine heads.

2.4 The function of caldendrin in controlling actin dynamics

In a set of experiments we explored how caldendrin influences actin dynamics in dendritic spines, by comparing caldendrin +/+ to caldendrin -/- spines. First, overexpression of eGFP-actin showed remarkable fluctuation in actin content within spine heads of caldendrin -/- (Figure 2.4). In the absences of caldendrin a subset of spines showed excessive variations in fluorescence intensity, indicating that the amount of actin within the spine head is strongly fluctuating.

We further tested the actin turnover by fluorescence recovery after photobleaching (FRAP). In +/+ neurons, actin in spines consists of a stable and dynamic pool (Star et al. [2002], Koskinen and Hotulainen [2014]). The dynamic pool is exchanged within the 2 minutes imaging time, while the stable pool ($\pm 30\%$) isn't. In caldendrin $-/-$ neurons the stable pool is absent (Figure 2.4C, D). Within 2 minutes all actin within the head of spines is exchanged indicating that caldendrin is important for stabilization of the actin cytoskeleton.

Synaptic activity is known to induce calcium influx and actin reorganization, and increases actin turnover in wildtype spines (Figure 2.4E). Stimulation with bicuculline did not affect the phenotype observed in caldendrin $-/-$. In coherence, knockout of caldendrin also increases the turnover of the interaction partner cortactin (Figure 2.4H). While CaMKII, as an independent control, is not affected (Figure 2.4I). The knockout phenotype of caldendrin isn't directly rescued by re-introducing caldendrin, but requires additional calcium influx from synaptic activity (Figure 2.4F, G). The FRAP experiments indicate that caldendrin is important for the regulation of actin dynamics, and that the binding of calcium is necessary to establish a stable pool of actin within spines.

2.5 The nano-organization of actin in spines of caldendrin knockout cultures

The live-imaging experiments indicated that the absence of caldendrin has severe consequences for actin dynamics in spines. To look in more detail, we employed Stimulated emission depletion (STED) microscopy to study the actin organisation at the nanoscale level (Figure 2.5). Primary neurons were fixed and stained for filamentous actin, then high resolution images were taken of 'mushroom' like spines. Mushroom like spines contain a particular actin organization, F-actin arranged in a cup shape surrounding the post-synaptic density. When studying the images, it became apparent that caldendrin $-/-$ leads to a disordered organization of this structure. The organization of actin was systematically analysed by measuring the fluorescence intensity along a line profile, starting from the head of the spine towards the base. In spine heads of caldendrin $-/-$ neurons, F-actin is slightly shifted towards the front. In addition, we analysed the actin organization in a two-dimensional plot, segmenting the spine head in 12 equally sized segments. Comparing spines of caldendrin +/+ and $-/-$ we observed that the arrangement of F-actin in a cup shape is less pronounced in the absence of caldendrin and more actin is shifted towards the front of the spine (Figure 2.5D). The last is also observed by plotting the average center of mass (Figure 2.5E).

2.6 The function of caldendrin in the establishment of structural LTP

The absence of caldendrin has profound consequences for actin dynamics in dendritic spines. Since caldendrin is a calcium binding protein and calcium influx occurs during synaptic transmission, it could be that caldendrin performs an important function in synaptic reorganization

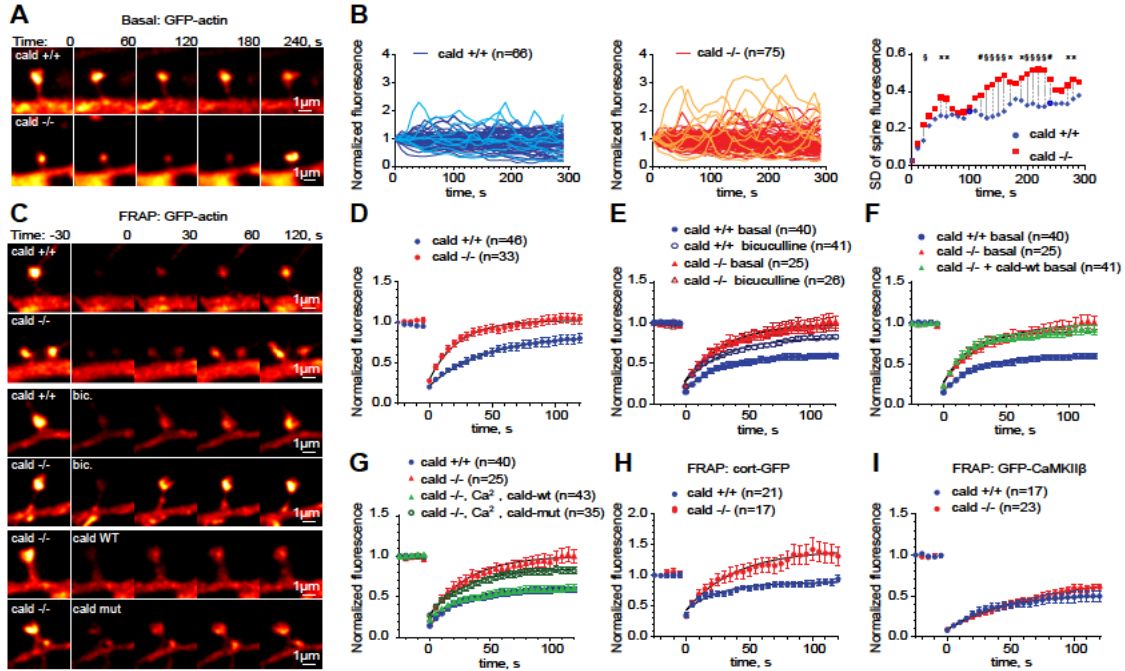


Figure 2.4: Actin dynamics in spines of caldendrin +/+ and -/- cultures.

- A) Examples of eGFP-actin fluctuations in a time-lapse series of caldendrin +/+ and -/- dendritic spines.
- B) Normalized fluorescence intensity of eGFP-actin in spines from time-lapse experiments, in wildtype (left) and knockout (middle). Right, quantification of the variance (standard deviation) for wildtype and knockout. F-test to compare variances * $p < 0.05$, # $p < 0.01$ and \$ $p < 0.001$. N = 3, n numbers (spines per group) provided in figure.
- C) Examples of eGFP-actin FRAP experiments for caldendrin +/+ and -/- neurons. Experiments were performed in untreated cultures, cultures treated with bicuculline to enhance activity, and re-introduction of caldendrin wildtype and Ca^{2+} binding mutant in a knockout background.
- D) FRAP curves of eGFP-actin in caldendrin +/+ and -/- dendritic spines. N = 3, n numbers (spines per group) provided in figure.
- E) FRAP curves of eGFP-actin in caldendrin +/+ and -/- dendritic spines in combination with bicuculline treatment. N = 2, n numbers (spines per group) provided in figure.
- F) FRAP curves of eGFP-actin in caldendrin +/+ and -/- spines. Re-introduction of caldendrin in a -/- background does not result in a reduction of the -/- phenotype. N = 2, n numbers (spines per group) provided in figure.
- G) Similar experiment to F, except cultures with re-introduced caldendrin or a Ca^{2+} -binding mutant of caldendrin were treated for 5 min with bicuculline 8 h prior to the experiments. Rescue can be observed upon re-introduction of caldendrin in combination with neuronal activity inducing calcium influx. N = 2, n numbers (spines per group) provided in figure.
- H) FRAP curves of cortactin-eGFP in caldendrin +/+ and -/- spines. N = 1, n numbers (spines per group) provided in figure.
- I) FRAP curves of eGFP-CaMKII β in caldendrin +/+ and -/- spines. N = 1, n numbers (spines per group) provided in figure.

2 THE CALCIUM BINDING PROTEIN CALDENDRIN CONTROLS ACTIN DYNAMICS IN THE HEAD OF DENDRITIC SPINES

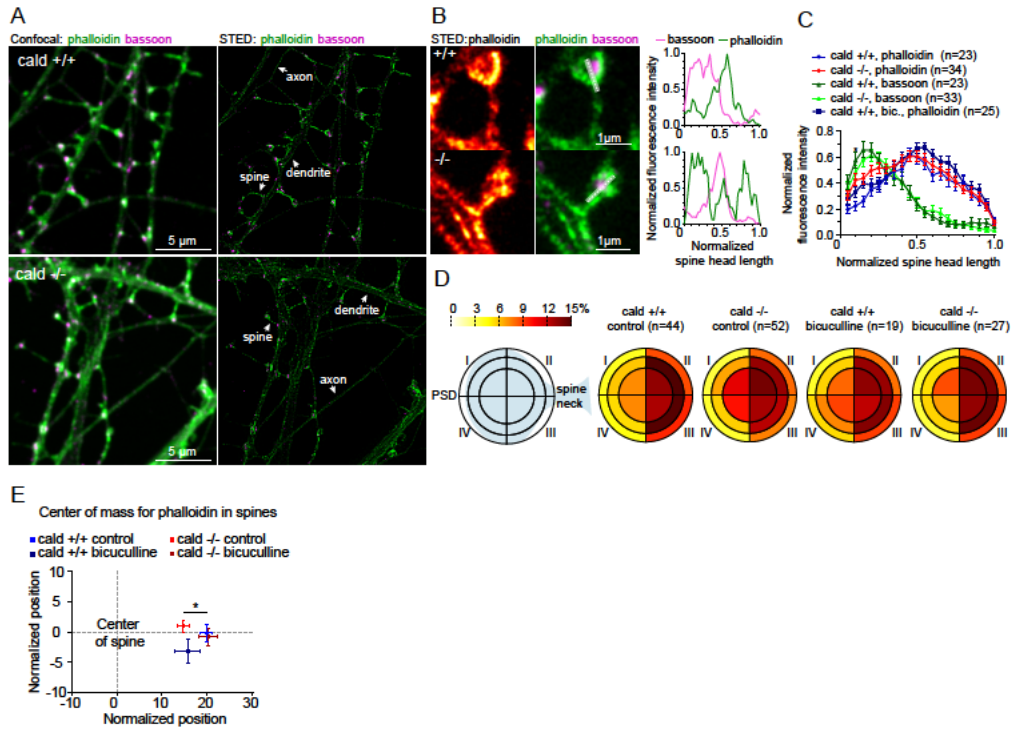


Figure 2.5: The nanostructure of F-actin in spines of caldendrin +/+ and -/- cultures.

A) Overview images of GATEDSTED visualizing filamentous actin (phalloidin) and the presynaptic scaffolding protein bassoon.

B) GATEDSTED images showing a disorganized F-actin structure in the head of caldendrin -/- spines. Intensity plots are given on the right for the line crossing the spine head indicated in the microscope images.

C) Average of multiple line profiles across spine heads from caldendrin +/+ and -/- cultures. Data are represented as mean \pm SEM. 2-way ANOVA with Sidak's post hoc test. * $p < 0.05$ (+/+ versus -/-). N = 2, n numbers (spines per group) provided in figure.

D) 2D descriptive analysis of the actin organization in spine heads of caldendrin +/+ and -/- cultures, including enhancement of neuronal activity by bicuculline treatment. N = 2, n numbers (spines per group) provided in figure.

E) Center of mass for the F-actin organisation in spine heads. Data are represented as mean \pm SEM. 1-way ANOVA with Bonferroni post hoc test, * $p < 0.05$ (+/+ versus -/-). Same dataset as in D).

during the initiation of long-term potentiation. We experimentally tested this by performing 2-photon glutamate uncaging in organotypic hippocampal slices. Single spines of fluorescently labelled neurons were targeted with LTP inducing stimuli, consisting of repetitive optically triggered uncaging of glutamate in the absence of magnesium. This protocol induces strong calcium influxes through the NMDA receptors, resulting in structural LTP; enlargement of the spine (Figure 2.6). In line with previously published reports (Bosch et al. [2014], Govindarajan et al. [2011], Harvey and Svoboda [2007]), we found that spines of wildtype neurons react with an initial fast growth in spine volume which is later maintained at approximately 1.5 times of the initial volume. Spines in caldendrin $-/-$ cultures showed similar kinetics with the exception that the spine volume highly fluctuated during the first 15 minutes after stimulation. Within this time period, calcium signals are translated to actin dynamics, forming a new larger organised actin meshwork (Bosch et al. [2014]). The absence of caldendrin alters the actin reorganization phase, which could have implication for the stability of the spine complex over longer time periods (>1 hour).

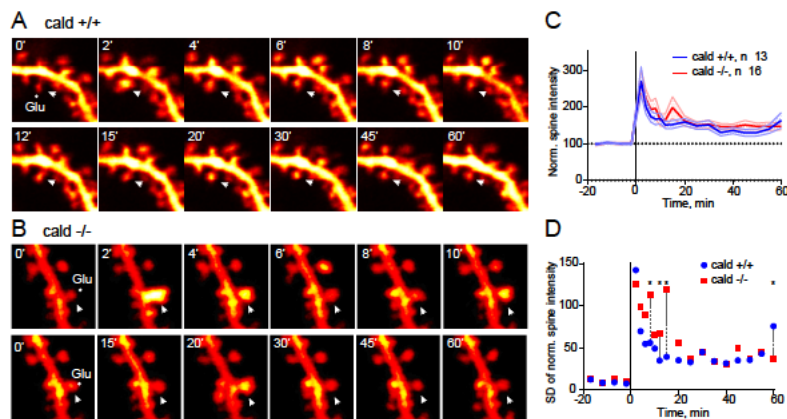


Figure 2.6: Single spine structural LTP in caldendrin $+/+$ and $-/-$ organotypic slice cultures. A) Example of single spine LTP via glutamate uncaging in a wildtype culture. Arrow indicates the stimulated spine. B) Example of single spine LTP via glutamate uncaging in a caldendrin knockout culture. Arrow indicates the stimulated spine. The stimulated spine shows strong fluctuation in fluorescence intensity. C) Average of normalized fluorescent intensity as a measure for spine volume. Single spine stimulation results in structural enlargement of the spine head in both wildtype and caldendrin knockout slice cultures. Slices from 6 caldendrin $+/+$ and 5 caldendrin $-/-$ mice. n (spines per group) numbers provided in figure. D) Stronger fluctuations in spine size are seen for caldendrin $-/-$, reflected in the standard deviation. F-test to compare variances of spine size between caldendrin $+/+$ and $-/-$. * $p < 0.05$. Slices from 6 caldendrin $+/+$ and 5 caldendrin $-/-$ mice. Same dataset (n) as in panel C).

2.7 The function of caldendrin in dendritic spines

The presented set of experiments shines light on the function of caldendrin in respect to the actin dynamics at dendritic spines. Caldendrin, a calcium binding protein, is important for keeping the actin dynamics in balance (Figure 2.7). In situations where caldendrin is absent, spines display higher actin dynamics and the established actin structures are disorganized at nanoscale level.

2 THE CALCIUM BINDING PROTEIN CALDENDRIN CONTROLS ACTIN DYNAMICS IN THE HEAD OF DENDRITIC SPINES

The outcome of the experiments suggests that caldendrin, after calcium influx, together with cortactin stabilizes parts of the actin cytoskeleton ensuring the existence of stable 'mushroom' like spines. Other experiments published in Mikhaylova, suggest that the caldendrin-cortactin complex could protect actin branches from cofilin severing (Mikhaylova et al. [2018]). In addition, co-immunoprecipitation experiments suggest that caldendrin supports actin branching by promoting the interaction between cortactin and N-WASP. These findings point to a role of caldendrin in establishing a stable actin cytoskeleton in response to calcium elevations. Altogether, caldendrin translates calcium signalling to spinous actin dynamics, promoting stability in F-actin and overall spines morphology.

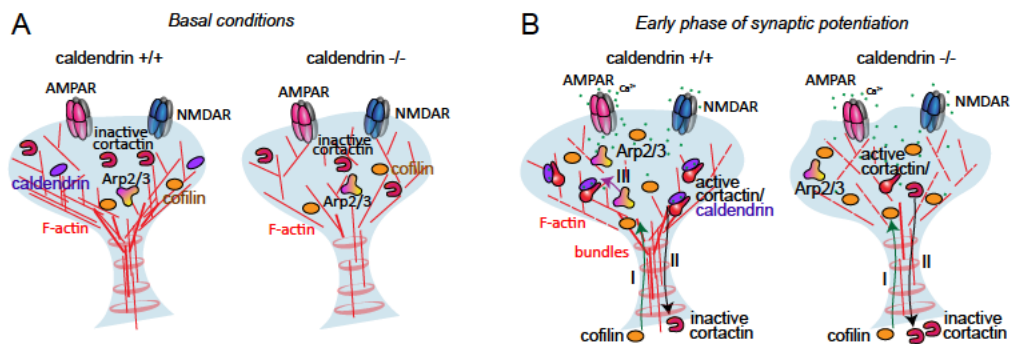


Figure 2.7: Model illustrating the function of caldendrin.

A) In basal conditions caldendrin is present within the cytosol with, so far, no characterized interaction partners.
 B) Upon synaptic stimulation and calcium influx, caldendrin's conformation becomes opened which exposes its N-terminus. At the same time, cofilin enters the spine head and severs F-actin branches (I). During this time caldendrin binds cortactin by its N-terminus, preventing it from leaving the spine (II), and together by binding F-actin filaments, protect a small proportion of filaments from severing. In a later phase (III), caldendrin comes loose from F-actin bound cortactin and allows binding of N-WASP and the Arp2/3 complex for the growth of new actin filaments. In caldendrin knockout a stable/ protected actin pool is absent. This result in an unstable actin cytoskeleton and extreme fluctuations in morphology upon calcium influx.

2.8 Materials and methods

2.8.1 Animals

All experiments involving the use of animals were conducted in accordance with the European Communities Council Directive (2010/63/BJ) and the Animal Welfare Law of the Federal Republic of Germany (Tierschutzgesetz der Bundesrepublik Deutschland, TierSchG) approved by the local authorities of Sachsen-Anhalt/Germany (reference number 42502-2-987IfN and 42502-2-1264 LIN, TV 42502-2-1009 UniMD) or by the city-state Hamburg (Behörde für Gesundheit und Verbraucherschutz, Fachbereich Veterinärwesen) and the animal care committee of the University Medical Center Hamburg-Eppendorf. Animals used for the study were bred and housed in the animal facility of the Leibniz Institute for Neurobiology, Magdeburg, Germany, or the ZMNH, Hamburg, Germany.

2.8.2 Caldendrin-knockout mouse strain

Caldendrin knockout mice were obtained from the Texas A & M Institute for Genomic Medicine (Houston, USA). The knockout mice strain was obtained using the OmniBank ES cell clone OST258109 derived from the 129SvEv strain. Mice in the study were backcrossed for a minimum of at least 10 generations to C57BL/6J strain and derived from heterozygous breedings. Genotyping was conducted using the following primers: Cald-wt-Fwd: GGGGAGGGTGATC-CGATGTCTC, Cald-wt-Rev: GGATTTTCCTGTCTCTGACTCCTCA, LTR2-mut-Fwd ATG-GCGTTACTTAAGCTAGCTTGC. Polymerase chain reaction (PCR) products were analysed by gel electrophoresis.

2.8.3 Constructs

Table 2.1: List of constructs

Backbone	Promoter	Insert	Source
pGW1	CMV	CFP-caldendrin-YFP	This study
pEGFP-N1	CMV	GFP-caldendrin-GFP	This study
pmCherry-C1	CMV	mCherry-cortactin	This study
pAAV	Synapsin	mRuby2	Gift from T.G. Oertner
p- β -actin	β -actin	GFP-actin	This study
pEGFP-C1	Synapsin	YFP	This study
pEGFP-C1	CMV	GFP-CamKII β	Gift from Tobias Meyer, Addgene plasmid #21227
pAAV	CMV	Cortactin-GFP	This study

2.8.4 Primary hippocampal culture

Primary hippocampal cultures were prepared from wildtype and caldendrin $-/-$ mice. In brief, hippocampi were dissected from P0 mice and cells were dissociated by incubation in trypsin

for 10 min at 37 °C. Dissociated cells were plated on poly-L-lysine coated coverslips in a density of 50000 cells for transfection or 30000 cells for immunocytochemistry (ICC)(18 mm \varnothing coverslips) in Dulbecco's modified eagle medium (DMEM, Thermo Fisher Scientific) supplemented with 8 % FCS, 1 % penicillin/streptomycin. After cell adherence, cells were further cultured in Neurobasal medium (GIBCO) supplemented with 0.5 mM glutamine, 2 % B27 and 1 % penicillin/streptomycin (all GIBCO) at 37 °C, 5 % CO₂. Transfection was performed using lipofectamine 2000 (Thermo Fisher Scientific) according to manufacturer's description. Transfected cells were imaged 24-72 h after transfection.

2.8.5 Immunocytochemistry

Cells were fixed in 4 % PFA (Roti-Histofix, Carl-Roth)/ 4 % sucrose for 10 min at RT. Subsequently, cells were washed three times and permeabilized with 0.2 % Triton X-100 (PanReac AppliChem, A4975) in phosphate buffered saline (PBS) for 10 min. After two washes with PBS, samples were blocked with blocking buffer (BB, 0.1 % Triton X-100, 10 % horse serum in PBS). Samples were incubated with primary antibody (anti-basson clone (SAP7F407) 1:500, Stressgen #ADI-VAM-PS003) in BB overnight (ON) at 4 °C, and washed three times with PBS. Next, samples were incubated with secondary antibodies (anti-mouse Abberior Star 580, abberior #2-0002-005-1) in BB. After three times washing with PBS, samples were incubated with phalloidin-Atto647N (1:40 dilution in PBS, according to manufacture's instructions) at RT for 2.5 h. Samples were washed three times in PBS and mounted on microscope slides with mowiol.

2.8.6 Organotypic hippocampal slice cultures

Organotypic hippocampal slice cultures were prepared from male and female P9 wildtype and caldendrin $-/-$ mice. Hippocampi were dissected in preparation medium (HAME-01 Prep Medium, Cell Concepts, Umkirch, Germany). Next, hippocampi were sliced using a McIlwain tissue chopper (Mickle Laboratory Engineering, Surrey, UK) to 350-400 μ m thick slices. Slices were placed on Millipore membranes (4 slices per membrane, Merck Millipore) placed in 6- well plates with 1 ml OHSC medium (50 % MEM, 25 % heat inactivated horse serum, 25 mM glucose, 2 mM glutamine, 25 mM HEPES, 2 % B27, 1 % penicillin-streptomycin, < 25 % Hank's balanced salt solution (HBSS) +/-). Culturing was performed at 37 °C, 5 % CO₂. Every three days 0.9 ml of the medium was exchanged for new medium, starting from 2 days *in vitro* (DIV).

2.8.7 Single-cell electroporation

At DIV5, single CA1 neurons were transfected by single-cell electroporation as described previously (Wiegert et al. [2017]). Cells were electroporated using an Axoporation 800A (Axon Instruments) under visual control via Dodt/DIC contrast. Slices were placed in sterile filtered extracellular medium containing (in mM): 145 NaCl, 10 HEPES, 25 D-glucose, 2.5 KCl, 1 MgCl₂, 2 CaCl₂ (pH 7.4, 318 mOsm). Plasmids were diluted (30 ng syn-mRuby2 or 40-50 ng syn-YFP) in potassium-based intracellular solution containing (in mM): 135 K-gluconate, 0.2 EGTA, 4 MgCl₂, 4 Na₂-ATP, 0.4 Na-GTP, 10 Na₂-phosphocreatine, 3 ascorbate, 0.02 Alexa Fluor 594, and 10 HEPES (pH 7.2). DNA was transferred by 50 hyperpolarizing pulses (0.5 ms,

-12 mV, at 50 Hz). After electroporation, slices were placed back in their original culturing medium and further cultured in the incubator. For morphological analysis slices were fixed in 4 % PFA (Roti-Histofix, Carl-Roth)/ 4 % sucrose one day after electroporation and mounted in mowiol. Two-photon glutamate uncaging was performed 2-4 days after electroporation.

2.8.8 Protein dynamics and FRAP

Live imaging was performed using a Leica SP5 (Leica) microscope equipped with a 63x objective (HCX PL APO CS 63.0x 1.40 oil objective). Images were acquired with a 4x digital zoom, 8-bit, 512x512 pixels, resulting in a final pixel size of 120 nm. Fluctuation of actin in spines was assessed in spines of DIV12 primary neuronal cultures, transfected with GFP-actin alone or in combination with mRuby2. Images were acquired with a 10 s interval.

Baseline actin fluctuations in spines was assessed by GFP intensity in the spine head. Intensity values for each time point were compared to the intensity in the first recorded image.

For FRAP experiments, DIV20/21 mouse hippocampal cultures were treated with 50 μ M bicuculline for 5 min. FRAP was performed using the Leica software built-in FRAP wizard. Images were acquired with a 5 s interval. Regions of interest (ROI) were photo-bleached with 3-5 scans with maximum laser power (488 nm). 5 baseline frames were recorded before photobleaching. Recovery was recorded within 25 frames. For rescue FRAP experiments, DIV11-13 mouse hippocampal cultures were treated with 50 μ M bicuculline for 5 min and imaged 8 h afterward.

FRAP recovery was calculated using Fiji. ROIs were placed on the bleached spine, and a non-bleached dendritic stretch as control, and in a cell-free area to measure the background. Measured intensity values for the photo-bleached spines were background subtracted for each time point, normalized to their dendritic control and normalized to the first pre-bleach value.

2.8.9 FRET acceptor bleaching

FRET acceptor bleaching experiments were performed using a SP5 Leica confocal system (Leica). Fluorophores were excited by an Argon laser at a wavelength of 458 nm for CFP, 488 nm for GFP and 514 nm for YFP. mCherry was excited by a 561 nm diode laser. YFP and mCherry were photobleached at maximum intensity of the corresponding lasers. FRET efficiency was calculated using the Leica FRET-AB Wizard where E_{FRET} was calculated $E_{\text{FRET}} = (D_{\text{post}} - D_{\text{pre}}) / D_{\text{post}}$ with D being donor fluorescence before (pre) and after (post) acceptor bleaching. All live experiments were carried out in a humidified chamber at 37 °C, 5 % CO₂. To assess the calcium dependent conformational change of caldendrin in dendritic spines, caldendrin $-/-$ neurons were transfected with YFP-caldendrin-CFP at DIV11. A tandem of YFP-CFP and co-overexpression of single YFP/CFP were used as controls. After transfection, neurons were cultured in conditioned medium containing 1 μ M TTX and imaged the next day. The same coverslips were used to measure in silenced conditions (TTX) and stimulated condition after medium exchange with 50 μ M bicuculline. To study the calcium-dependent interaction of caldendrin and cortactin in spines, GFP-caldendrin-GFP and mCherry-cortactin were co-transfected in DIV13-16 rat primary neurons. Overexpression of a mCherry-GFP tandem and co-overexpression of single mCherry/ GFP were used as control. FRET acceptor photobleaching was performed maximum 1 h after bicuculline stimulation.

2.8.10 Confocal microscopy of organotypic slices

Fixed organotypic slices were imaged with a Leica SP5 microscope (Leica), using a 63x objective (HCX PL APO CS 63.0x1.40 oil objective, Leica). For analysis of dendritic morphology, neurons were imaged at a 1x zoom (512 px, 8-bit, 400 Hz scan speed per line, 1 μm z-step size, 2x frame average). mRuby2 was excited using a 561 nm laser. Multiple tiles were stitched using the Leica ASF software (Leica). For analysis of spine morphology, images were acquired at a higher 4x digital zoom with a step size of 0.3 μm .

2.8.11 GATEDSTED microscopy

The nanostructure of actin in the head of dendritic spines was analysed using an SP8-3X-GATEDSTED microscope (Leica). Samples were labelled for F-actin with phalloidin-Atto647N and with an anti-bassoon antibody detected by an Abberior Star 580-labelled secondary antibody. Atto647N and Abberior Star 580 were excited with a white light laser (WLL), tuned to respectively 660-730 nm for Atto647N and 580-620 nm for Abberior Star 580. Both fluorophores were depleted using a 775 nm depletion laser, set in 2D configuration. The detector gating was set from 0.5/ 1 ns to 6 ns. All images were acquired using a 100x objective (HC APO CS2 100x/1.40 oil, Leica). Single plane images were taken at 5x digital zoom, 1024x1024 pixels, 600 lines per second and a line averaging of 16.

2.8.12 Two-photon glutamate uncaging

Two-photon glutamate uncaging was performed with an Olympus FV1000 upright 2-photon microscope, operated with Fluoview software (Olympus). Excitation was provided by a Ti:sapphire laser (Mai Tai, Spectra Physics) tuned to 920 nm. All experiments were performed using a 25x water dipping objective (Olympus XLPlanN 25x MP, 1.05 numerical aperture (NA), Olympus). Hippocampal slices were submerged in recirculating bubbled (95 % O₂, 5 % CO₂) Mg²⁺ free artificial cerebrospinal fluid (ACSF) containing (in mM): 119 NaCl, 26.2 NaHCO₃, 11 C₆H₁₂O₆, 1 NaH₂PO₄, 2.5 KCl, 3 CaCl₂, 2.5 MNI-caged-L-glutamate (Tocris) and 0.001 TTX (Tocris), pH 7.4, 30-32 °C. Spines chosen for stimulation were located on the secondary or tertiary branch of oblique dendrites. After imaging of a 15 min baseline, spines were stimulated by glutamate by application of 60 light pulses of 1 ms at 1 Hz. For stimulation the multiphoton-laser was tuned to 720 nm. Subsequently, changes in spines were imaged for 1 h. Spine size was estimated by fluorescence intensity. For each spine, the fluorescence intensity is normalized to the intensity at baseline. Spines that did not respond to the uncaging stimulus were excluded (< 20 % increase 2 min after uncaging).

2.8.13 Quantification and statistical analysis

Analysis of dendritic morphology

Analysis of dendritic morphology, of clearly distinguishable CA1 pyramidal neurons, was performed using the simple neurite tracer plugin for Fiji (Longair et al. [2011]). Dendritic length

and complexity (Sholl analysis) were both analysed using the plugin. The researcher was blind to the animal genotype during the analysis.

Analysis of dendritic protrusions

Analysis of dendritic protrusions of neurons in organotypic hippocampal slices was performed on deconvolved images. 3D image stacks were deconvolved using Auto-QuantX3 (Media Cybernetics) using: adaptive point spread function, blind deconvolution (with theoretical adaptive point spread function) in two dimensions, one iteration and medium noise suppression. Subsequently, a 1-pixel 2D Gaussian blur filter was applied using Fiji. Resulting images were used for 3D reconstruction and analysis in Imaris8.1 (Bitplane). Dendrites were reconstructed using the auto-path option of the filament tracer, at default settings. Detection of spines was performed with the settings: 0.15 μm minimal head size, 0.6 μm maximum length, seed point threshold approx. 10, no branched spines allowed. Spine detection was manually corrected, if necessary. Classification of protrusions into spines and filopodia was performed using the Imaris XTension 'classify spines' according to the following definitions: spine: spine length $< 1 \mu\text{m}$ or (spine length $< 3 \mu\text{m}$ and spine head width $\geq 0.3 \mu\text{m}$); filopodia: true.

Analysis of the actin organization in spine heads

The organization of actin in spine heads of wild type and caldendrin $-/-$ cultures (DIV14) were studied based on 2D STED data. Data included spines at basal condition and after 5 min of stimulation with 50 μM bicuculline, increasing synaptic activity. The actin organization was analysed by the fluorescence intensity along a line-profile, starting from the tip of the spine and ending at its base. Acquired data was normalized for spine size and maximum intensity, and pooled together. In addition, the actin organization in dendritic spine heads was analyzed using a custom written Matlab script (R2015a, MathWorks, Inc) describing the organization in 2D. In short, a circular ROI was placed on the middle of the spine head completely covering the spine head. The ROI was divided into 12 equally sized sectors (4 quadrants each subdivided into 3 sectors) with the spine neck always facing the same direction. Phalloidin-Atto647N intensities were measured in each of the sectors based on pixel intensities (16-bit) and normalized to the total amount of phalloidin-Atto647N per spine head. These values were plotted in a color code. At last, for each spine head we calculated the weighted center of mass including pixel values of all the pixels within the ROI. To compare spines, we normalized the coordinates (-100 to +100) of the center of mass to the ROI size with coordinates 0,0 as center of the spine head.

Statistical analysis

Statistical analysis was performed in Prism 6.05 (GraphPad, La Jolla, CA, USA). The type of parametric test used for each experiment and significant levels are stated in the corresponding figure legends. The reported n numbers correspond to spines, protrusions, dendritic segments or neurons as indicated. Values are reported as mean \pm SEM throughout the manuscript.

3 Periodic F-actin structures shape the neck of dendritic spines

This work is part of the scientific publication:

Periodic F-actin structures shape the neck of dendritic spines

Julia Bär*, Oliver Kobler*, Bas van Bommel* and Marina Mikhaylova
Scientific Reports, 2016

** These authors contributed equally*

Contribution of others in the work stated here:

Dr. Julia Bär helped with ICC and analysis. Dr. Marina Mikhaylova helped with acquiring STED images. Oliver Kobler provided technical assistance and deconvolved the microscopy images.

3.1 The actin cytoskeleton

The actin cytoskeleton is the most dynamic component of the cellular cytoskeleton. It is built of straight actin fibers. The straight actin fibers can also be arranged in a branched configuration in combination with protein complexes (including Arp2/3, Figure 1.3). Actin filaments are extremely dynamic and can quickly grow and depolymerize. The equilibrium is set by actin regulating proteins and the balance between actin filaments and its building blocks, single actin monomers. The regulation of the actin cytoskeleton is in most cells coupled to intracellular calcium signalling and other membrane-receptor dependent signalling pathways.

3.2 The membrane-associated periodic actin skeleton

The MPS took strong interest with the development of super-resolution light microscopy. However, the structure was long discovered before the introduction of super-resolution light microscopy by the use of replica electron microscopy (EM). Replica EM performed on erythrocytes, exposed the MPS for the first time including its components: actin, adducin and β -spectrin (Byers and Branton [1985], Shen et al. [1986]). Here the MPS had a 2D periodicity (hexagonal pattern). The discovery, however, was not followed up. Perhaps, because the MPS was not seen in most EM experiments due to the lack of contrast by which actin is presented in most contrast-EM prepared samples.

The developments in super-resolution light microscopy lead to the discovery of the MPS in neurons, and opened an emerging field of research. First reports describe a periodic organization of actin and spectrin in axons (Xu et al. [2013]). 3D stochastic optical reconstruction microscopy (STORM) indicated that the MPS forms ring-like structures (1D-periodicity) located at the plasma membrane (Figure 3.1a). The rings are formed by short actin filaments capped by the protein adducin (Leite et al. [2016]). Spectrin tetramers position the actin rings approximately 180-190 nm apart. Later studies found similar ring-like structures existing in dendrites and a 2D lattice within the soma of neurons, similar to the one observed in erythrocytes (Figure 3.1b, Byers and Branton [1985], Shen et al. [1986], Bär et al. [2016], D'Este et al. [2016], Han et al. [2017]). The exact function of the MPS is not yet fully understood, but the structure is highly conserved among species (He et al. [2016]). Recent studies shine first light on its function, indicating that the existence of the MPS influences diffusion of receptors and signalling at the membrane (Zhou et al. [2019]).

3.3 The MPS is found in the neck of dendritic protrusions

The neck of dendritic spines compartmentalizes the spine head from the dendritic branch. Similar to the head of spines, the neck is structured by the actin cytoskeleton (Korobova and Svitkina [2010]). In this work F-actin was visualized using fluorescently labelled phalloidin (Figure 3.2). Phalloidin is a small toxin that binds multiple actin monomers that are arranged in a filament. Hereby phalloidin can be used to only label filaments and no actin monomers, providing a clear labelling of the actin cytoskeleton (Melak et al. [2017], Wulf et al. [1979]). In combination with high-resolution light microscopy, here stimulated emission depletion (STED), phalloidin

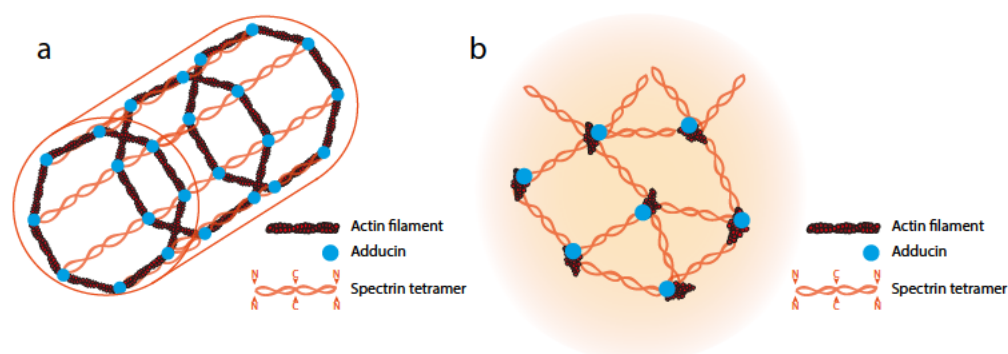


Figure 3.1: Schematic illustrations of the MPS.

A) The MPS as observed in axons, dendrites and dendritic protrusions. In super-resolution microscopy images the structure often appears as a lattice (a 1 dimensional periodicity).

B) The MPS as observed at the membrane of erythrocytes and the soma of neurons (a 2 dimensional periodicity).

labelling exposed a periodic actin structure within the neck of dendritic protrusions (Figure 3.2a). This periodicity has an interval of approximately 180-190 nm (Figure 3.2b) and is independent of protrusion length (Figure 1a,b). Longer dendritic protrusions have more actin repetitions. As expected, based on the other findings, the age of the neurons has no influence on the periodicity (Figure 3.2c).

3.4 The dendritic protrusions can be categorized as dendritic spines

To ensure that the studied protrusions are spines with a synaptic contact and no growth cones, the specimen were stained for the presynaptic scaffolding protein bassoon (Figure 3.3). The images indicate that the protrusions connect to presynaptic sites. Thereby we can be rather certain that the dendritic protrusions can be classified as dendritic spines. In addition, neurons expressed eGFP to outline the cell volume. The outline shows that the observed periodic actin lattice is located within the neck of spines.

3.5 The MPS in the neck of dendritic spines shows strong similarities to the MPS in axons and dendrites

The periodicity of the actin lattice within spine necks shows a strong similarity with the earlier reported actin rings in the axon and dendrites (Xu et al. [2013], D'Este et al. [2015], D'Este et al. [2016], He et al. [2016]). Here, we performed 2D- STED microscopy in which the rings appear as a lattice. We directly compared the interval of the lattice between the axon, dendrites and spine necks within the cultures (Figure 3.4). The observed periodicity in each of the neuronal compartments is highly similar, and most likely resembles the same structure. To fully verify this, one would image the spine neck in 3D super-resolution microscopy to see whether the actin

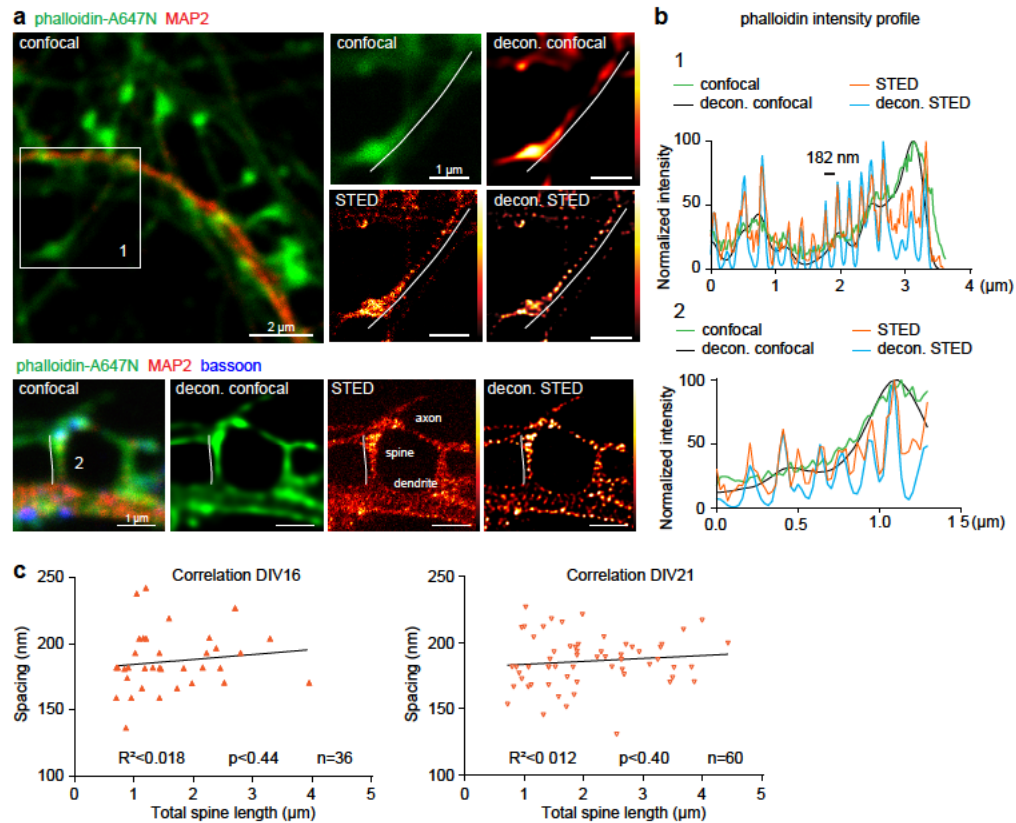


Figure 3.2: A periodic actin lattice in the neck of dendritic protrusions.

a) ICC staining for actin and MAP2 (dendritic microtubule marker) imaged with confocal and STED/deconvolved microscopy. Super-resolution resolved protrusions show a periodic actin lattice within the neck. The periodic lattice is found in long (upper) and short (lower) protrusions.

b) Intensity profiles along the neck of protrusion 1 and 2 (panel a). Scale bar indicates the average spacing within the actin lattice.

c) Periodicity of the actin lattice in the neck of dendritic protrusions plotted for neuronal cultures of DIV16 and 21. $N = 3$, n numbers (spines) provided in figure.

3 PERIODIC F-ACTIN STRUCTURES SHAPE THE NECK OF DENDRITIC SPINES

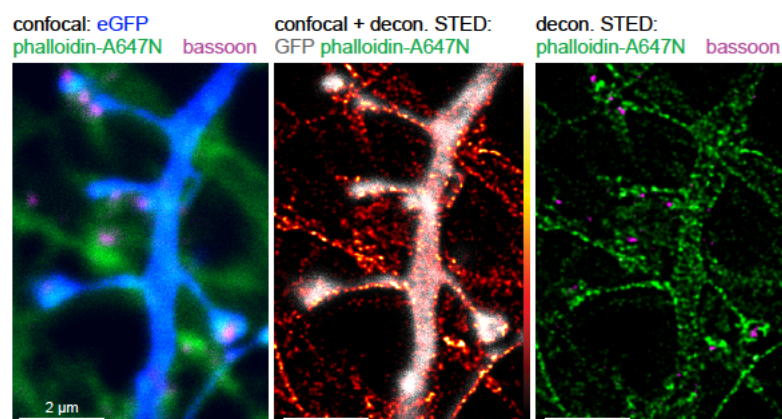


Figure 3.3: The dendritic protrusions are contacted by presynaptic sites. Confocal/STED images showing the dendritic morphology (eGFP), F-actin (phalloidin) and the presynaptic scaffolding protein bassoon.

forms rings. We have made several attempts with 3D-STED microscopy, but were unsuccessfully due to technical difficulties. 3D-STED microscopy is extremely harsh to the fluorophores in the sample, as the structure needs to be imaged a multitude of times to obtain the z-resolution. To be successful, one needs excellent fluorophores and a high labelling density. Unfortunately, the spine neck is very thin and contains little amounts of F-actin. This results in a very low number of binding places for phalloidin and a dimmer staining. Photobleaching of the low number of fluorescently-labelled phalloidin molecules made a 3D-acquisition impossible.

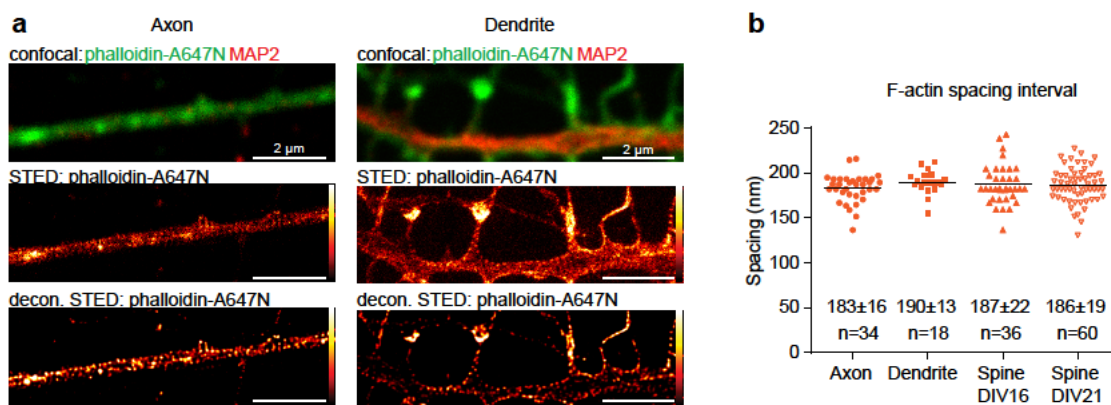


Figure 3.4: The MPS in dendritic spines is similar to the lattice in axons and dendrites. a) Confocal, STED, and deconvolved-STED images of an axon and dendrite. Both neuronal structures display a periodic actin lattice along the plasma membrane. b) Average periodicity interval of the periodic actin lattice in axons, dendrites and the neck of dendritic protrusions at DIV 16 and 21. N = 3, n numbers (spines) provided in figure.

3.6 Actin, but not β -II spectrin, forms a periodic lattice all throughout the neck of spines

To further characterize and test the similarities of the MPS in spine necks with the MPS located in other neuronal compartments, neurons were stained for F-actin and β -II spectrin. β -II spectrin is known to space the actin lattice in the axon and dendrites to the observed 180-190 nm interval (Xu et al. [2013]). 2-Colour STED microscopy revealed that β -II spectrin is also present in the neck of dendritic spines, and can cover the neck regions from the spine base up to the head (Figure 3.5a). Surprisingly, in some spine necks, the β -II spectrin lattice did not continue to the spine head but was discontinued earlier (Figure 3.5b). The exact cause of this discrepancy between spine necks is unknown and could have different causes. First, the methods for labelling of actin and spectrin are very different. F-actin was directly labelled by phalloidin, which is extremely small in size. β -II spectrin is labelled with a primary antibody and corresponding fluorescently labelled secondary antibodies. The primary and secondary antibodies, and its total complex, are considerably larger than phalloidin. The antibodies might have difficulties to penetrate into the narrow structure of the spine neck, or are unable to form a complex due to stochastic hindrance. This would lead to an absence of fluorophores in parts of the neck. The discrepancy could also have a biological origin. Parts of spine necks might not contain β -II spectrin, but other isoforms e.g. β -III spectrin (Efimova et al. [2017], Xu et al. [2013], Sidenstein et al. [2016]). Last, it might also be that a small population of the spines underwent plasticity and restructuring around the time of fixation, meaning that the absence of β -II spectrin is part of a restructuring/ synaptic plasticity event. Nonetheless, we can conclude that the observed lattice in spine necks is very similar to the rings observed in axons and dendrites. β -II spectrin is, at least, partially responsible for spacing the MPS within spine necks.

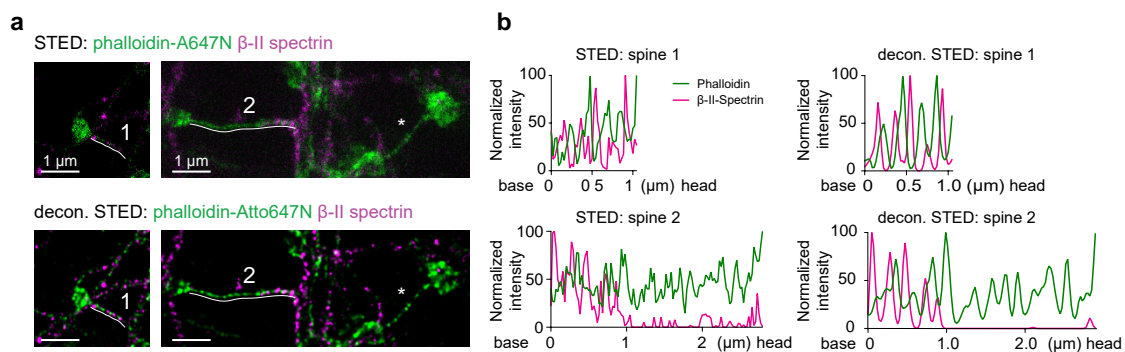


Figure 3.5: The F-actin lattice is more pronounced in spine necks than β -II spectrin. a) Confocal (upper) and deconvolved-STED (lower) images of F-actin and β -II spectrin. Images show an example of the periodic actin/spectrin lattice in short (left) and long (right) spines. In a proportion of the spine necks, the β -II spectrin lattice does not cover the full length of the spine neck. b) Intensity profile along the neck of spines displayed in panel a.

3.7 The periodic actin lattice in spine necks can be found in hippocampal tissue

All previously described experiments on the actin lattice in spine necks were performed in primary hippocampal cultures. In primary hippocampal cultures, neurons grow on glass coverslips in a single cell layer. The number of supporting cells such as astrocytes and microglia is limited. This way of culturing has strong advantages for microscopy and offers a wide experimental tool box. On the other hand, the culturing method could be considered artificial. Using tissue is a step closer to physiological conditions as found within the brain. To strengthen and validate the findings in primary hippocampal culture, we established a similar experiment in hippocampal slices. We tried different actin staining dyes to label actin in slices. In addition, we explored different administration techniques including single-cell electroporation, patch-clamp and bath application. We found that the simple administration of phalloidin in a highly concentrated droplet on top of slices provided the best actin staining in dendrites and spines (Figure 3.6a,b, Rex et al. [2010]).

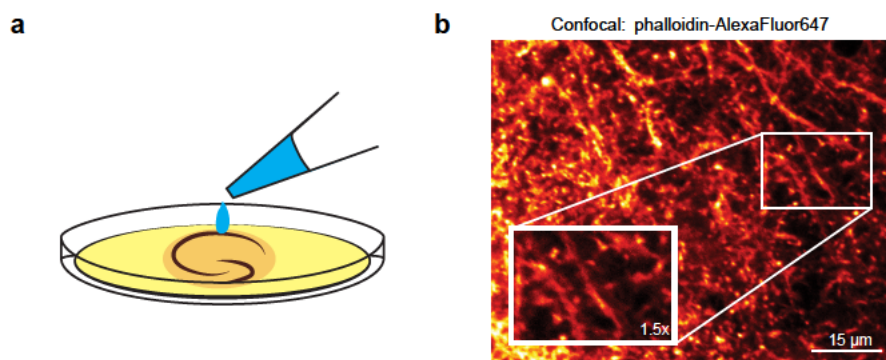


Figure 3.6: Phalloidin labels dendrites and spines in living hippocampal slices.
a) Drawing illustrating the administration of fluorescently labelled phalloidin to hippocampal slices.
b) Confocal images showing actin labelled by phalloidin in a living hippocampal slice.

From the initial establishment of an phalloidin-based actin staining in slices, imaged with confocal microscopy, we went further with super-resolution microscopy. In new experiments, 2D-STED microscopy in slices showed a similar actin lattice in the neck of spines than observed in primary hippocampal cultures (Figure 3.7a,b). The optical resolution is lower compared to the experiments performed in primary cultures due to light scattering of the excitation and depletion laser. Nonetheless, the periodicity of the lattice is similar to the periodicity observed in other experiments (Figure 3.7c).

Altogether, the results indicate the existence of a periodic actin lattice in the neck of dendritic spines (Figure 3.7d). The F-actin is partially or fully spaced by β -II spectrin, as observed in the axon and dendrites. The structure can be found both in primary hippocampal cultures and hippocampal tissue, indicating that the MPS is an intrinsic structure of neurons. The function of the periodic actin lattice in the neck of the dendritic spine requires further investigation.

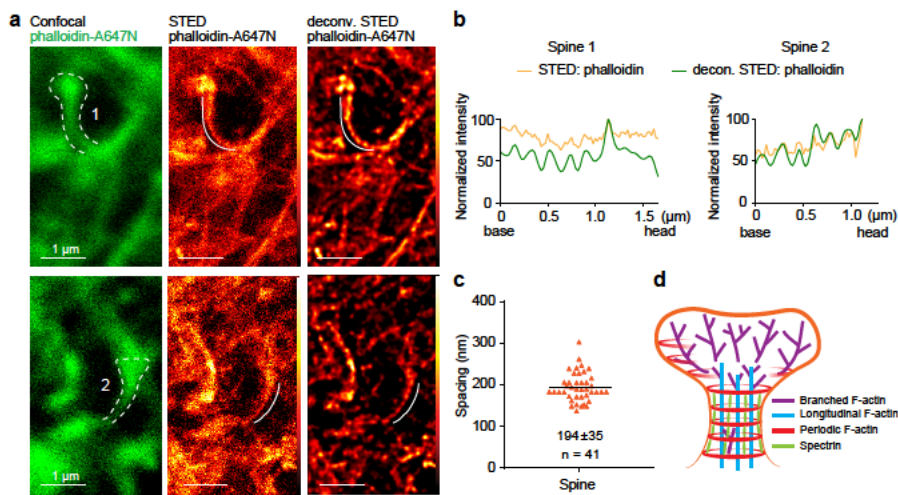


Figure 3.7: The MPS can be found in the neck of spines in hippocampal slices.
 a) Confocal, STED, and deconvolved-STED images showing the actin organization of spines in hippocampal tissue. Similar to primary cultures, the periodic actin lattice is present within the neck of spines.
 b) Intensity profile along the neck of dendritic spines displayed in panel a.
 c) Average spacing of the actin lattice in the neck of dendritic spines from tissue. $N = 2$, n numbers (spines) provided in figure.
 d) Model of the F-actin organization in dendritic spines, illustrating actin rings within the dendritic neck, which appear in super-resolved light microscopy as a periodic lattice.

3.8 Materials and methods

3.8.1 Animals

Animals used for this study were sacrificed in accordance with the Animal Welfare Law of the Federal Republic of Germany (Tierschutzgesetz der Bundesrepublik Deutschland, TierSchG) and with the approval of the local authorities of the city-state Hamburg (Behörde für Gesundheit und Verbraucherschutz, Fachbereich Veterinärwesen, from 21.04.2015) and the animal care committee of the University Medical Center Hamburg-Eppendorf.

3.8.2 Primary hippocampal culture

Primary hippocampal cultures were prepared from E18 wistar rat embryos. Hippocampi were isolated and washed in ice cold HBSS (Sigma Aldrich). Cells were incubated with trypsin for 15 min at 37 °C. Afterwards, cells were washed in warm HBSS, triturated by repeated pipetting through needles (20 G, 26 G), filtered with a 100 µm strainer (Greiner), counted and plated on poly-L-lysine coated coverslips in 1 ml of DMEM (Thermo Fisher Scientific), supplemented with 10 % fetal calf serum, 2 mM glutamine and 1x penicillin/streptomycin. Approximately 40000 cells were plated per coverslip in a 12-well plate. After cell adherence (approximately 1 h), the medium was exchanged to neurobasal medium (Thermo Fisher Scientific, supplemented with 2 % B27, 0.5 mM glutamine, 1x penicillin/ streptomycin). Cells were cultured at 37 °C, 5 % CO₂. Transfection of primary neurons was performed at DIV15 using lipofectamine 2000 (Invitrogen). Neurons were incubated for 1 h with transfection medium containing peGFP-N1 (Clontech). Afterwards, medium was exchanged to conditioned medium and neurons were cultured for 1 day at 37 °C, 5 % CO₂.

3.8.3 Immunocytochemistry

For ICC, primary neurons were fixed at DIV16/21 with 4 % PFA (Roti-Histofix, Carl-Roth)/ 4 % sucrose for 10-15 mins. Coverslips were washed 3x in PBS, permeabilized for 10 min with 0.2 % Triton-X-100 (PanReac AppliChem #A4975) in PBS and washed again in PBS. The coverslips were blocked for 45 min to 1 h in blocking buffer containing 0.1 % TritonX-100, 10 % horse serum in PBS. Next, coverslips were incubated with primary antibody diluted in blocking buffer at 4 °C ON. Antibodies used in this study: rabbit anti-MAP2 (Abcam #ab32454, 1:400), mouse anti-bassoon (clone SAP7F407, Stressgen, 1:500) and mouse anti-β-II spectrin (BD Biosciences #61256, 1:150). Next day, coverslips were washed 3x in PBS and incubated for 1.5 h with secondary antibody in blocking buffer at room temperature (RT). Secondary antibodies used in this study: anti-rabbit Alexa Fluor 488 (Invitrogen, 1:500) and anti-mouse Abberior Star 580 (Abberior, 1:200). After 3 washes with PBS coverslips were incubated with phalloidin-Atto647N (1:40 in PBS, according to manufacture's instructions, Sigma Aldrich) for 2.5 h at RT, followed by incubation at 4 °C ON. Subsequently, coverslips were washed with PBS and mounted onto objective slides using mowiol.

3.8.4 Preparation of hippocampal slices and phalloidin uptake assay

Hippocampal slices were prepared from a 9-weeks old male Wistar rat. Hippocampi were dissected in ice-cooled dissection medium consisting of (in mM): 1 CaCl₂, 5 MgCl₂, 10 glucose, 4 KCl, 26 NaHCO₃, 248 sucrose, 2 kynurenic acid, 0.001 % phenol red, (Sigma-Aldrich). The hippocampi were sliced into 400 µm slices using a tissue chopper (McIlwain Mickle Laboratory Engineering). Obtained slices were placed on Millicell membranes (Merck Millipore) placed in culturing medium consisting of MEM (Invitrogen), containing 20 % horse serum, 1 mM L-glutamine, 0.00125 % ascorbic acid, 0.01 mg/ml insulin, 1 mM CaCl₂, 2 mM MgSO₄, 13 mM D-glucose, 1 M HEPES pH ≈ 7.28 (Sigma-Aldrich). Slice were placed in an incubator set to 37 °C, 5 % CO₂. At the same day, a small droplet of phalloidin-Atto647N (2-4 µl, 6.6 µM) was pipetted on top of a slice. After a 1 h incubation period, the slices were imaged at a Leica TCS SP8-3X GATEDSTED microscope.

3.8.5 Confocal and GATEDSTED microscopy

Confocal and GATEDSTED images were acquired using a Leica TCS SP8-3X GATEDSTED microscope (Leica). Fluorophores were excited using a WLL tuned to 640 nm for Atto647N, 561 nm for Abberior Star 580 and 488 nm for eGFP. Emission light was collected in the wavelengths: 660-730 nm for Atto647N, 580-620 nm for Abberior Star 580 and 495-530 nm for eGFP. Light was collected in gates from 0.5-1 ns to 6 ns. STED, for Atto647N and Abberior Star 580, was obtained with a 775 nm depletion laser. Images were acquired using a 5x digital zoom in the center of the frame, resulting in a final pixel size of 23 nm. Images were taken with 600 lines per second and 16x line averaging. Corresponding confocal image were obtained using the same setting except the excitation power was reduced, and the detector gate timings were set to 300 ps to 6 ns. STED images of hippocampal slices were acquired by placing the hippocampal slices upside down in a live imaging chamber. The chamber was filled with HEPES-buffered ACSF (in mM: 145 NaCl, 10 HEPES, 12.5 D-glucose, 1.25 NaH₂PO₄, 2.5 KCl, 1 MgCl₂, 2 CaCl₂, (Sigma-Aldrich), pH ≈ 7.4 at RT). Imaging settings were similar to described above, with the exception of an increased digital zoom of 6x and a final pixel size of 18.9 nm.

3.8.6 Data analysis

Data was analysed in Fiji Schindelin et al. [2012]. The protrusion length was measured by drawing a segmented line from the spine base along the neck to the tip of the protrusion. Protrusions were classified as spines when they showed a clear presynaptic contact as visualized by bassoon ICC. Intensity profiles along spine necks were created in Fiji using the plot profile option and were obtained using a 3 pixel wide segmented line. Resulting values were exported, normalized to the maximum intensity values, and graphs were generated in Prism 6 (GraphPad, La Jolla, CA, USA). Local maxima were used for quantification of the lattice interval. Peaks were manually defined, and the average inter-peak distance of at least 3 subsequent peaks was taken. The researcher was blind to the origin of the profile (spine, axon or dendrite).

3.8.7 Statistics

Differences in F-actin periodicity in spines, dendrites and axons was analysed by 1-way analysis of variances (ANOVA) after testing for equal variances between the groups (Brown-Forsythe test) using Prism 6. Correlation between spine length and actin spacing was analysed using linear regression mode in Prism 6. Prism 6 was also used to create all graphs.

4 F-actin patches associated with glutamatergic synapses control positioning of dendritic lysosomes

This work is part of the scientific publication:

F-actin patches associated with glutamatergic synapses control positioning of dendritic lysosomes

Bas van Bommel*, Anja Konietzny*, Oliver Kobler, Julia Bär and Marina Mikhaylova
The EMBO Journal, 2019

** These authors contributed equally*

Contribution of others in the work stated here:

Dr. Marina Mikhaylova helped with acquiring STED imaging and analysis. Oliver Kobler helped by providing technical expertise on STED microscopy and image deconvolution. Dr. Julia Bär helped with the designs of the experiments and composing the figures. I would also like to thank Anja Konietzny for her input to the project. Parts of her findings are summarized in the text here, further details can be found in the publication 'F-actin patches associated with glutamatergic synapses control positioning of dendritic lysosomes' or her dissertation 'Of Road Blocks and Loading Bays - Control Mechanisms of Dendritic Cargo Trafficking'.

4.1 The cytoskeleton organisation and its functions

The cell cytoskeleton performs a multitude of cellular functions. It provides strength and paths for intracellular transport. Here we study the organisation and function of the cytoskeleton in dendrites, and broaden our knowledge on how the cytoskeleton in dendrites is organised and how this affects molecular transport.

4.2 Actin patches within the dendritic shaft

As previously addressed, the actin cytoskeleton in dendrites composes of three major elements: F-actin bundles, dendritic protrusions and the MPS. When studying F-actin in dendrites with STED microscopy we also observed other actin structures: dense actin patches located within the dendritic shaft (Figure 4.1A,B). These structures were both present in fixed cells, labelled with phalloidin, and in living cells where actin was labelled by overexpression of an actin-chromobody (an intracellular actin binding nanobody linked to a fluorescent protein, Figure 4.1B). When actin labelling was combined with immunostaining for bassoon, it became apparent that many of these dense actin structures were opposed by a presynaptic terminal (Figure 4.1C). This suggests that these actin structures could be part of synapses that are located at the dendritic shaft.

To investigate the possibility that these dense actin patches at the dendritic shaft are part of synapses, we explored their presence during neuronal development. We fixed neuronal cultures at different stages during development, and performed ICC for F-actin (phalloidin), bassoon (anti-bassoon) and MAP2 (anti-MAP2, Figure 4.2). At young age (DIV 4), neurons mainly extend their axon and start to grow their first dendrites. At DIV 6, the dendrites grow out and develop a large arbour for the later developing dendritic protrusions. Starting from DIV 8, primary neurons develop synaptic connections and their number is strongly increasing to the age of DIV 12. To track the overall development of the dendritic tree, we included the staining for MAP2. MAP2 exclusively binds to microtubules in the soma and dendrites, and can thereby be used as a dendritic marker. The experiment indicates that the first dense dendritic actin patches emerge around DIV 8, the time that synaptogenesis starts. They also highly co-localize with presynaptic bassoon, which supports the hypothesis that the dense structures are part of synapses.

4.3 Actin patches are part of active excitatory synapses

To further characterize and verify if dendritic actin patches are part of synapses, we performed ICC for different synaptic markers. Homer1 was used as a marker for excitatory and gephyrin for inhibitory synapses. Inhibitory synapses are known to mostly project onto the dendritic shaft, while excitatory synapses are mostly located on dendritic spines and at a much lower number found at the dendritic shaft. To our surprise we found that most actin patches are co-localizing with homer1, suggesting that actin patches are mostly part of excitatory synapses located on the dendritic shaft (Figure 4.3A-C). We continued with studying the distribution of actin patches at dendritic segments. We found that most actin patches are part of shaft synapses; a small share is part of dendritic spines and is located at the base of the spine neck (Figure 4.3D). In addition,

4 F-ACTIN PATCHES ASSOCIATED WITH GLUTAMATERGIC SYNAPSES CONTROL POSITIONING OF DENDRITIC LYOSOMES

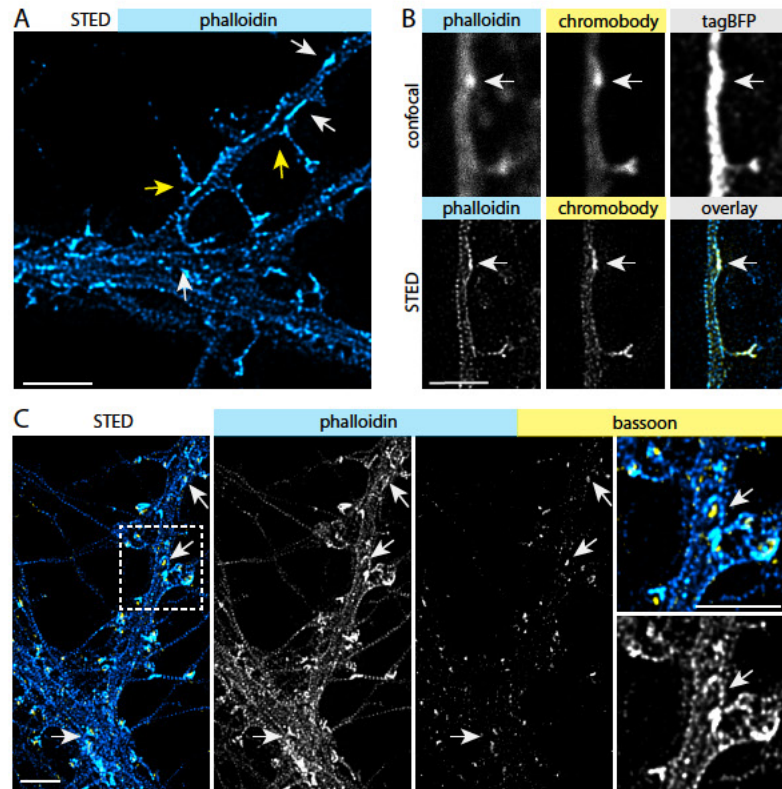


Figure 4.1: Super-resolution microscopy reveals the dendritic actin cytoskeleton at the nanoscale level.

A) Deconvolved STED image showing the dendritic F-actin cytoskeleton labelled with phalloidin. Yellow arrows indicate dense actin structures at the base of spines. White arrows indicate dense actin patches within the dendritic shaft. Scale bar: 2 μ m.

B) Fixed cells which overexpressed an actin-chromobody, and tagBFP to outline the cell. Phalloidin and actin-chromobody label the same dense actin structures. TagBFP indicates that the actin structures are located within the dendritic shaft. Scale bar: 2 μ m.

C) Deconvolved STED image of a dendrite labelled for F-actin with phalloidin and the presynaptic scaffolding protein bassoon. The image and close-ups show that dense actin structures at the dendritic shaft are opposed by bassoon. Scale bar: 2 μ m.

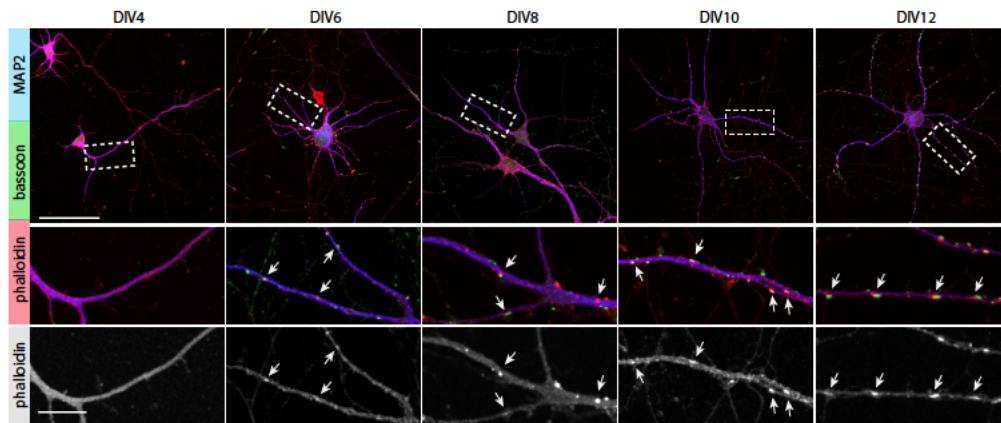


Figure 4.2: Development series of primary hippocampal neurons stained for a synaptic marker (bassoon), dendritic marker (MAP2), and the actin cytoskeleton (phalloidin). Primary hippocampal neurons fixed at different stages during development and stained for F-actin, bassoon, and MAP2. Dense dendritic structures are first found around the time when synaptogenesis starts. Scale bar: 50 μm , 10 μm close-ups.

we analyzed the size of the actin patches and found that patches positive for synaptic markers are on average slightly larger in size (Figure 4.3E).

To test whether the labelled excitatory/inhibitory synaptic markers (scaffolding molecules) are part of functional synapses, we performed a synaptotagmin antibody uptake assay (Figure 4.3F,G). Synaptotagmin is a transmembrane protein located at presynaptic vesicles. Living primary cultures were incubated with a fluorescently conjugated primary antibody against the luminal part of synaptotagmin. During synaptic activity, when synaptic vesicles fuse with the cellular membrane, the luminal part of synaptotagmin is exposed to the extracellular space. In this moment the antibody can bind and label synaptotagmin. Hereby we labelled all active synapses in an 30 minutes incubation period. The results indicate that the excitatory scaffolds are part of fully functional synapses, contacted by an active presynaptic partner. As control we silenced cultures with TTX, inhibiting synaptic transmission. Within the TTX control, synaptic activity and labelling intensity is strongly reduced. Little staining might originate from spontaneous release of vesicles, independent of neuronal activity.

4.4 Dendritic actin patches are dynamic actin structures, but their location is stable

The actin cytoskeleton in cells is extremely dynamic and prone to remodelling. However, some structures, e.g. dendritic spines, may persist for longer time periods. The life-time of dendritic actin patches is fully unknown. To study the dynamics of actin patches, we overexpressed eGFP as a volume marker together with an actin-chromobody to label F-actin. Time-lapse microscopy and corresponding kymographs showed that dendritic actin patches are stable structures that can persist for a time period of at least one hour (Figure 4.4). Also interesting to note, none of the

4 F-ACTIN PATCHES ASSOCIATED WITH GLUTAMATERGIC SYNAPSES CONTROL POSITIONING OF DENDRITIC LYOSOMES

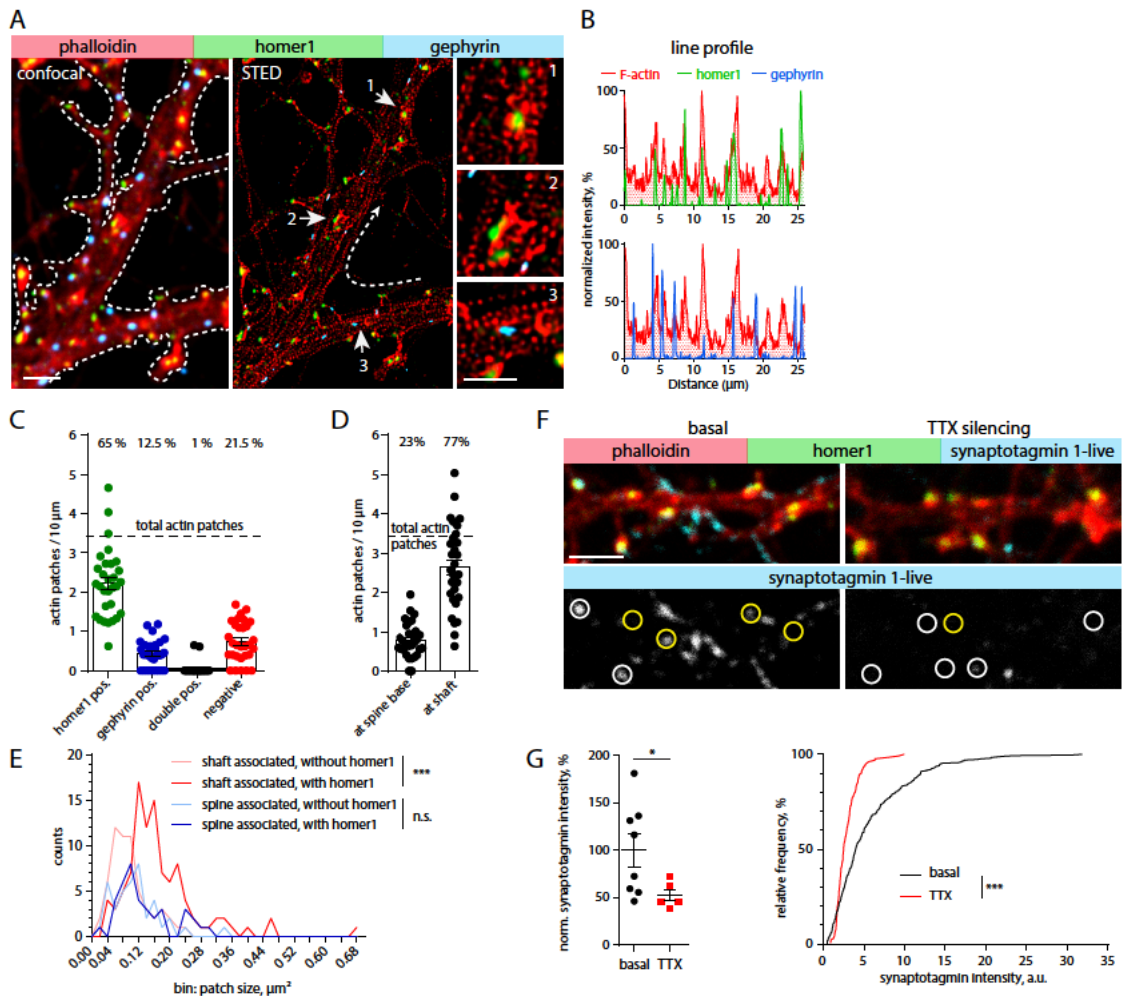


Figure 4.3: Dendritic actin patches are part of functional excitatory shaft synapses.

A) A dendritic branch stained for F-actin (phalloidin), homer1 and gephyrin. Smaller panels show the localization of homer1 or gephyrin at the dendritic shaft. Scale bar: 2 μm , 1 μm close-ups.

B) Intensity profile along the dendrite shown in panel A. The directionality is indicated by the dotted arrow.

C) Analysis of the proportion of dense actin patches positive for homer1 or gephyrin. The largest proportion of actin patches is positive for homer1. A smaller number is positive for gephyrin and a subset is negative for both makers. $n = 30$ dendritic segments of 19 cells in two independent cultures. Data are presented as mean \pm SEM.

D) Graph illustrating the density and position of actin patches within the dendritic shaft. Same n as in (C). Data are presented as mean \pm SEM.

E) Distribution of actin patch sizes, separated for homer1 positive/negative and spine/shaft associated. Mann-Whitney U-test. *** $p < 0.001$. $n = 59$ (shafts associated without homer1), $n = 101$ (shaft associated with homer1), $n = 40$ (spine associated without homer1), and $n = 38$ (spine associated with homer1) patches from 27 analyzed dendritic segments of 22 cells in two independent cultures.

F) Representative images showing the uptake of synaptotagmin antibody at basal conditions and upon silencing of neuronal activity by TTX. Yellow circles indicate active presynaptic sites opposing the dendritic shaft. White circles indicate active presynaptic sites projecting to dendritic spines. Scale bar: 2 μm .

G) Quantification of the synaptotagmin antibody uptake assay corresponding to panel F. Left: normalized synaptotagmin intensity measured in ROIs. Mann-Whitney U-test. * $p = 0.045$. $n = 8$ (basal) and $n = 5$ (TTX) analyze images with each 16-82 synapses per image from 1 culture. Right: Frequency distribution of synaptotagmin intensity of individual synapses. TTX treatment significantly decrease the intensity. Two-tailed Mann-Whitney U-test. *** $p < 0.001$. $n = 303$ (basal) and $n = 132$ (TTX) synapses.

actin patches transitioned into a dendritic protrusion during the 1 hour imaging sessions. The dendritic actin patches appear to be stable, long persisting structures.

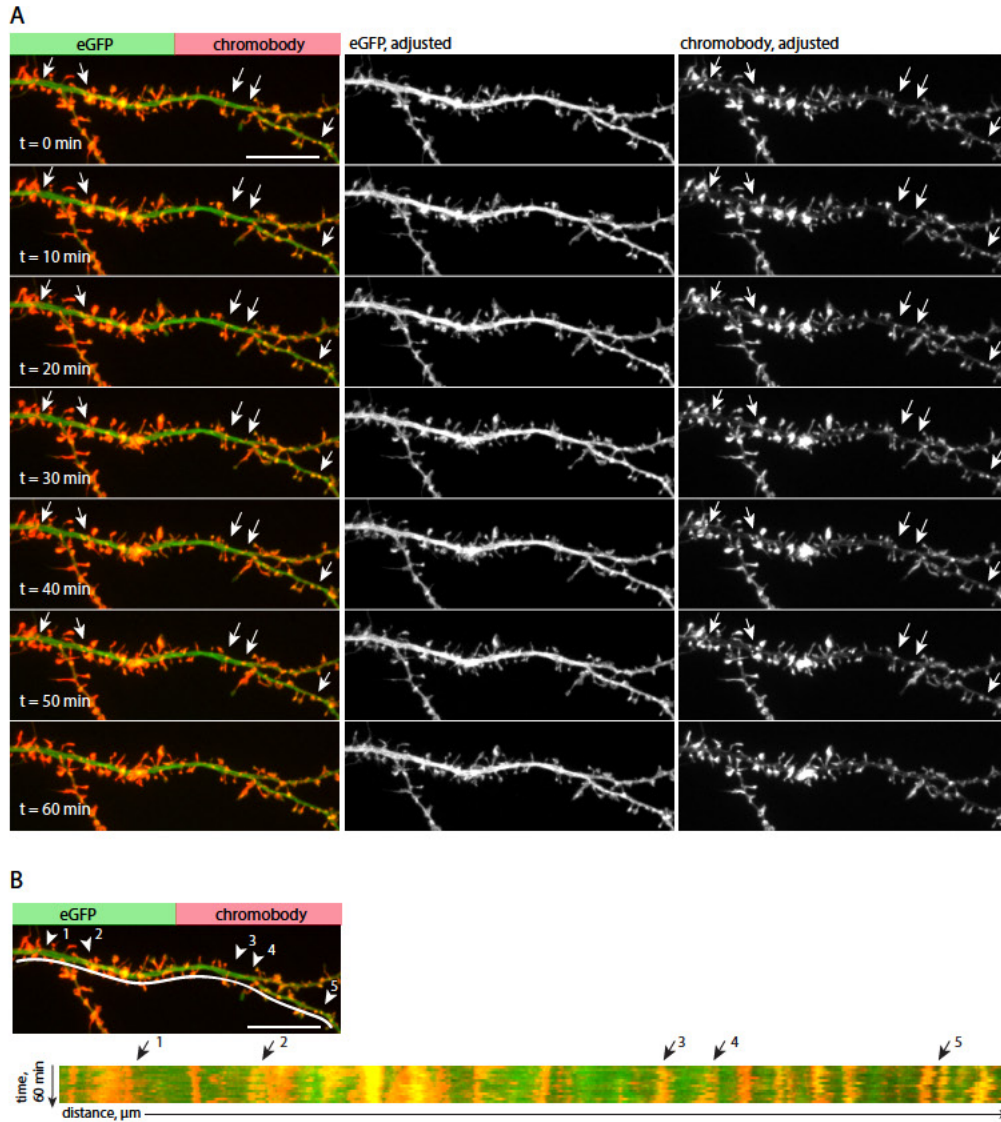


Figure 4.4: Time-lapse series of F-actin structures at a dendritic segment.

A) Time-lapse series of a dendritic segment with eGFP outlining the cytoplasm volume and an actin-chromobody visualizing the actin cytoskeleton. Images were obtained by spinning-disk microscopy. Actin patches at the dendritic shaft are indicated by the white arrows and are stable over a 1 h time period. Scale bar: 10 μm .

B) Kymograph of the dendritic segment shown in panels A,B, indicating the stability of actin patches during a 1 h time period. Arrows indicate actin patches at the dendritic shaft. Scale bar: 10 μm .

The actin dynamics at actin patches was further investigated using FRAP microscopy. Fluorescently labelled actin was overexpressed, and imaged by rotating oblique angled illumination. To compare the actin dynamics at dendritic patches to the well-known dynamics within spines,

both actin at patches and spines were photo-bleached (Figure 4.5A, Star et al. [2002], Koskinen and Hotulainen [2014])). The results indicate that the actin dynamics at patches and spines are very similar (Figure 4.5B). Both contain a large ($\pm 80\%$) dynamic actin pool that is exchanged approximately every 3 minutes. 20% of the actin is stable, and exchanged on a much longer time scale. Interestingly, the results indicate that the location of the actin structures has no influence on the recovery dynamics. Actin located in the head of spines is partially constricted in the spine head by a thin spine neck. In FRAP experiments, for recovery, bleached actin molecules in the spine head have to exchange with fluorescent molecules from the shaft. The photo-bleached actin from dendritic patches can directly be exchanged with a high number of actin molecules present in the large volume of the dendritic shaft. The fact that the recovery curves are similar indicates that the spine neck forms no constriction for actin dynamics (under basal conditions). This also suggests that the actin dynamics at patches and spines are similarly controlled and that turnover of the molecules is limited by actin modifying proteins.

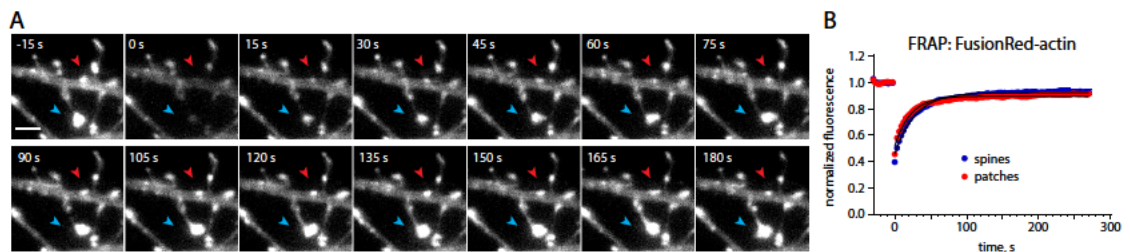


Figure 4.5: F-actin turnover at dendritic patches and within the head of dendritic spines.
 A) FRAP of fusionRed-actin at a spine head (blue arrow) and dendritic patch (red arrow) in a DIV16 neuronal culture. Scale bar: 2 μm.
 B) Quantification of multiple FRAP experiments at dendritic spines and actin patches. Dendritic spines and actin patches show similar actin dynamics. n = 118 (actin patches) and n = 129 (spines) from 26 cells from two independent cultures.

4.5 Dendritic lysosomes are positioned close to microtubules and at actin patches

The location of dendritic actin patches brings them in close proximity to other cellular structures, such as microtubules. Microtubules are often arranged in bundles with a uniform directionality (Tas et al. [2017]). To test whether microtubules invade or cross actin patches, we performed ICC for both structures and performed STED microscopy. The obtained images show that microtubules surround the actin patches (Figure 4.6A). The areas occupied by actin patches are negative of α -tubulin, suggesting that microtubules do not invade these actin structures. Actin patches and the microtubule cytoskeleton exist side-by-side in dendritic segments.

The microtubule and actin cytoskeleton are both known to function as paths for transport. Transported cargoes are bound by a variety of motor proteins by which they can follow both microtubule and actin filaments. Switches of paths are known from microtubule-based towards actin-based transport. This transition may take place, since myosin motor proteins are stronger than kinesins and dynein complexes (Bergeijk et al. [2015], Kapitein et al. [2013], Schroeder III

4.5 DENDRITIC LYOSOMES ARE POSITIONED CLOSE TO MICROTUBULES AND AT ACTIN PATCHES

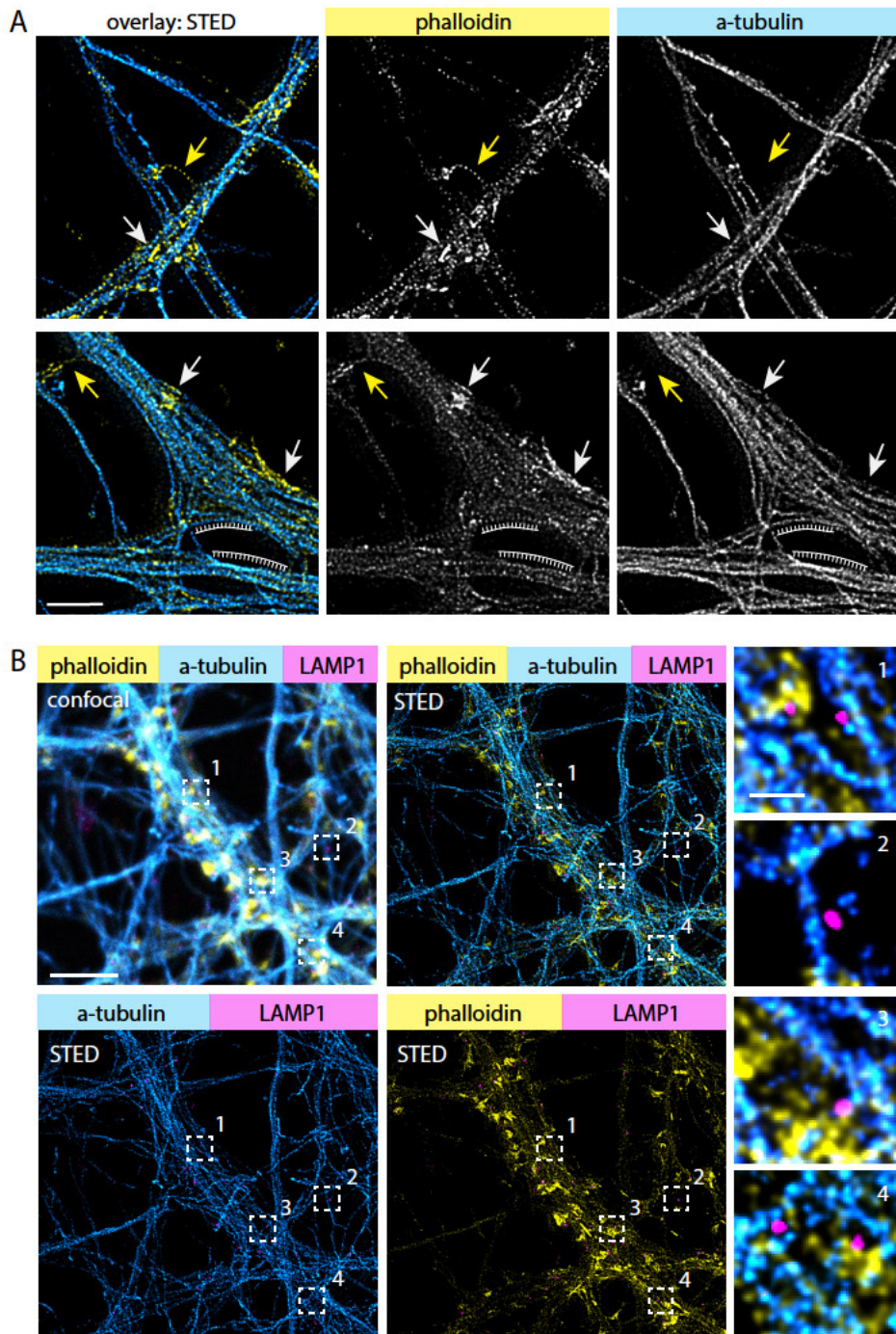


Figure 4.6: The microtubule and actin cytoskeleton form segregated structures to which lysosomes associate. A) Deconvolved STED images showing microtubules and the F-actin cytoskeleton of a dendritic branch. Microtubules surround, but do not cross, actin patches. B) Three colour deconvolved STED images showing lysosomes, microtubules and the F-actin cytoskeleton in a dendritic branch. Inserts highlight 1) lysosomes embedded inside actin patches. 2) Lysosome closely positioned at a microtubule. 3) and 4) lysosomes located on the interface between microtubule and F-actin.

et al. [2010]). To test how cargoes behave around actin patches, we studied the location of lysosomes with three-colour STED microscopy (Figure 4.6B). Lysosomes form an ideal model cargo, as they are good to label and are bound to kinesins, dyneins and myosins (van Bommel et al. [2019]). Hereby lysosomes could bind both microtubules and actin patches. In dendrites, we found lysosomes close to microtubules, most likely being transported along them, and located on the interface between microtubules and actin patches. Some of the lysosomes were surrounded by the actin cytoskeleton, and are most likely interacting exclusively with the actin cytoskeleton. Lysosomes, based on their location, likely interact with microtubules as well as the actin patches found within the dendritic shafts.

4.6 Lysosomes are stalling at dendritic actin patches

To observe directly the mobility of lysosomes, and their possible interaction with actin patches, neurons were transfected with a lysosome marker (LAMP1-eGFP) and an actin-chromobody (chromobody-TagRFP). Simultaneous imaging of both markers was performed using a spinning-disk microscope equipped with two cameras. In line with other studies, we found that lysosomes are transported in antero- and retrograde directions within the dendrites (Figure 4.7, Goo et al. [2017]). Sometimes they stop, and kymograph analysis suggests that this frequently occurs around actin patches. A minor share of the lysosomes was not mobile during the three minutes imaging periods. These lysosomes, judged from the kymographs, are associated with the larger actin structures (Figure 4.7A).

To quantify the stalling behaviour of lysosomes in relation to the actin patches, I created a custom Matlab script (MathWorks)(Figure 4.8). The script was written to determine if the position of actin patches correlates with the stopping of lysosomes. At first, the Matlab script dissects the position of actin patches from the kymograph based on peak intensity and first neighbouring minima. The positions of the actin patches (stable during the 3 min imaging sessions) are converted to a mask. The positioning of the lysosomes was manually traced in kymographs with straight lines in Fiji (Schindelin et al. [2012]), and the line coordinates were imported into Matlab. The mobility (displacement over time) of lysosomes was determined by the slope of the lines. Next, the average speed was computed for line segments inside and outside of the actin mask. The same calculation was made with a shifted mask, as control. Here the actin patch locations were randomly placed without experimental influence. When actin patches stall lysosomes, lysosomes around actin patches (within the actin mask) have on average a lower mobility than that from lysosomes located further away. When the mask is randomly shifted, the mask loses its spatial information about the actin patches and a possible correlation would be lost. The analysis of lysosome mobility in combination with the position of the actin patches indicates that the lysosome mobility around actin patches is significantly reduced (Figure 4.7B). The results strongly imply that the actin patches can induce stalling of lysosomes.

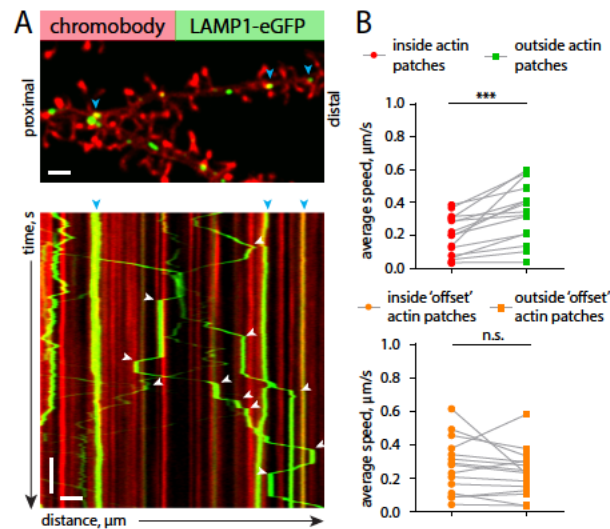


Figure 4.7: Analysis of lysosome mobility in proximity and away from actin patches.

A) Top, dendritic branch with overexpression of a fluorescently tagged actin nanobody and lysosome marker LAMP1. Bottom, corresponding kymograph of the dendritic branch spanning a time period of three minutes. White arrows indicate stopping of lysosomes at actin patches. Blue arrows indicate non-mobile lysosomes.

B) Quantification of lysosome mobility in relation to actin patches for multiple experiments. Top graph shows a reduced mobility of lysosomes around actin patches. Bottom graph illustrates that randomization of the actin patch location abolishes this effect, stressing the influence of actin patches on lysosome stalling. Two-tailed paired Student's t-test. *** $p = 0.0004$. $n = 15$ dendritic segments of 11 cells in three independent cultures.

4.7 What is the mechanism of lysosome stalling at dendritic actin patches?

The observation that lysosomes stall at actin patches raises the question: what factors are involved? We hypothesized that the actin patches could form binding places for myosins or present physical obstacles, both could interfere with microtubule-based transport (Figure 4.9). Myosins, bound to lysosomes, might bind to actin patches. Hereby microtubule transport may switch to actin based transport (Schroeder III et al. [2010]). This may imply a role for unconventional myosin V and myosin VI, which have been shown to outcompete microtubule transport and actively transport cargoes along actin filaments (Esteves da Silva et al. [2015], Kapitein et al. [2013]). In neurons myosin V stalls cargoes at the AIS, thereby preventing them from entering the axon. To do this, myosin V bound to cargo interacts with a dense branched actin network located within the AIS. Moreover, myosin V is known to transport cargoes into spines by walking towards the plus-end of actin filaments (Wang et al. [2008]). Myosin VI is known to transport cargoes towards the minus-end of actin, thereby it transports cargoes out of dendritic spines (Esteves da Silva et al. [2015]). This transport by myosins is much slower than that of kinesins and dyneins, and might sometimes be interpreted as stalling. Cargoes might also stall by the activation of multiple myosins. When this happens in an environment with a multitude of branched actin filaments, myosins running on differently oriented filaments might compete for direction-

4 F-ACTIN PATCHES ASSOCIATED WITH GLUTAMATERGIC SYNAPSES CONTROL POSITIONING OF DENDRITIC LYSOSOMES

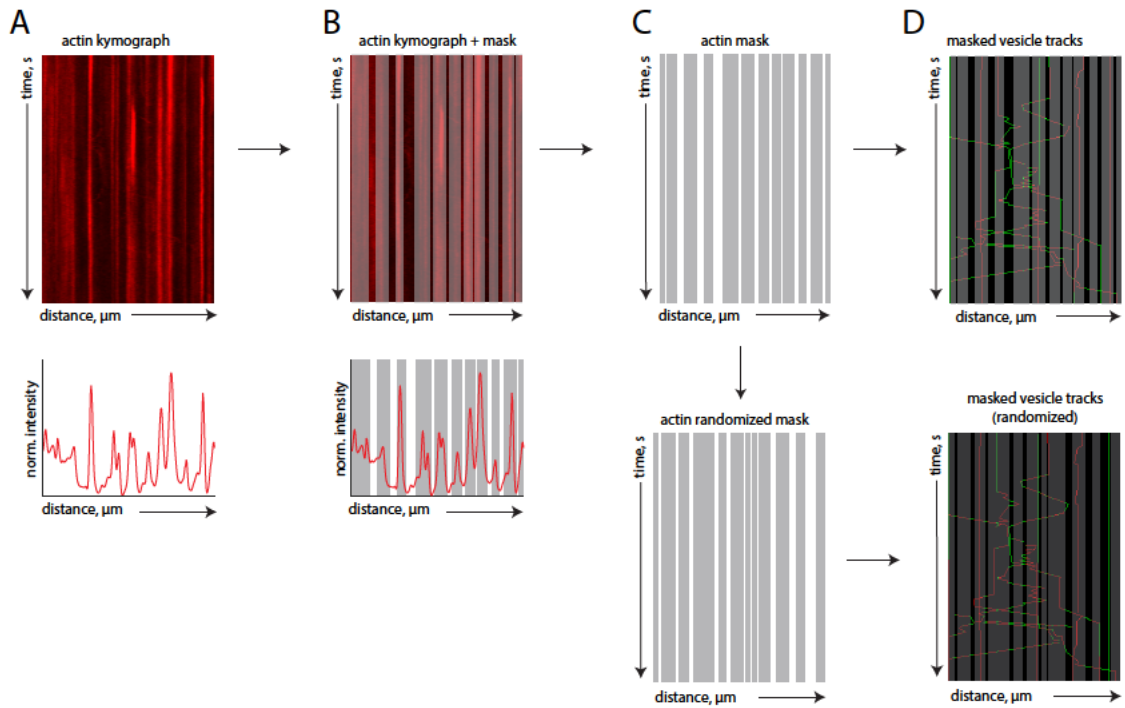


Figure 4.8: Illustration of the Matlab analysis of lysosomes mobility in proximity and away from actin patches.

A) Kymograph and corresponding intensity profile of dendritic F-actin.

B) The kymograph of dendritic F-actin and the corresponding generated mask.

C) The generated actin mask and created randomized mask.

D) Masks used to analyse lysosomes mobility (lines) in proximity of actin patches (red). Green lines illustrate lysosome positions further away from actin patches.

ality which could result in cargo stalling. This would be a tug-of-war between myosin motors. The last is highly speculative, as competition between myosins has not been shown *in vivo*.

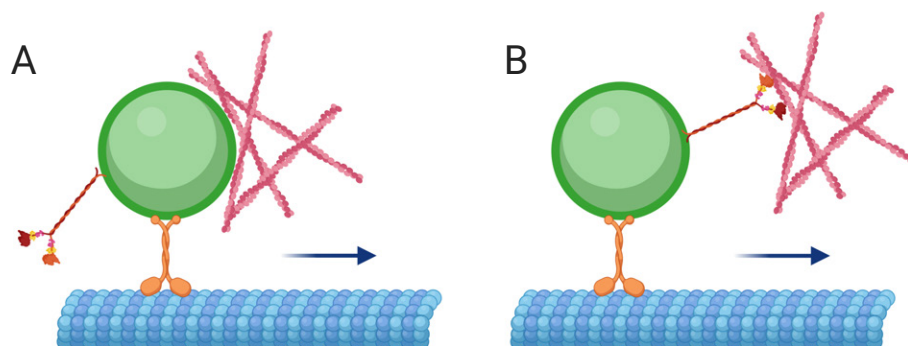


Figure 4.9: Actin induces stalling of lysosomes by forming a barrier or a binding location for vesicle associated myosins.

A) Actin can form a physical barrier for microtubule based transport.

B) The binding of vesicle associated myosins to actin patches enhances the stalling of lysosomes.

This image is created with Biorender.

We hypothesized that dendritic lysosomes are bound by myosins, since lysosomes are both found in the dendrites and axon (Goo et al. [2017]). Anja Konietzny tested and found that lysosomes are bound by both myosin V and VI. By overexpressing dominant negative myosins and using specific inhibitors, she found that myosin V but not VI increases the time of stalling, suggesting that activity of myosin V is involved in the stalling of lysosomes at actin patches (van Bommel et al. [2019], Konietzny [2020]). However, myosin V activity could not fully explain the stalling of lysosomes at actin patches. The competition with a dominant negative form of myosin shortened, but did not abolish the stalling of lysosomes.

In addition we tested the hypothesis that actin patches form physical obstacles for microtubule transport. In cell lines it has been shown that the actin cytoskeleton can form intracellular obstacles for large round objects (Katrukha et al. [2017]). Quantum dots electroporated to the cytoplasm of cells display a bimodal distribution with a slow and fast diffusing fraction. Interestingly, after disruption of the actin cytoskeleton the fraction of slower diffusing quantum dots declines while the number of fast diffusing quantum dots increases. The results indicate that the actin cytoskeleton can obstruct and limit the mobility of larger objects. In line, we tested whether the actin patches can form physical barriers for microtubule based transport. Anja Konietzny performed live imaging of lysosomes in combination with latrunculin treatment. Abolishing of the actin cytoskeleton resulted in an overall increase of lysosome mobility, supporting the idea that actin patches form barriers. To further clarify the mechanism, she forced peroxisomes (negative for myosins) to be transported within the dendrites by recruiting kinesin 2 (KIF17). The mobilized peroxisomes stall at actin patches, but their stalling time is shorter than that of endogenous lysosomes. In fact, it turned out that both mechanisms (actin forming obstacles and activity of myosins) happen to work together. Actin patches create obstacles which induces the stalling of lysosomes, and myosin V activity can extend the time of stalling.

4.8 Do dendritic actin patches influence all dendritic transport, and what is the role of synaptic activity?

In this work lysosomes were taken as an example cargo for dendritic transport; similar 'traffic' rules may apply to other dendritic cargoes. We tested mitochondria, but their transport in mature neurons is rather limited (data not shown). Their size is also considerably larger than that of lysosomes. It is more expected that smaller, more mobile cargoes, display similar kinetics to lysosomes. This could include recycling endosomes, ER-to-Golgi intermediate compartments and Golgi-satellites. The fact that actin patches are found at the base of spines, or are part of excitatory shaft synapses raises many new questions regarding the role of synaptic activity. Synaptic activity and the influx of calcium could affect the F-actin organisation and activity of myosins (Batters et al. [2016], Homma et al. [2000], Nascimento et al. [1996], Nguyen and Higuchi [2005], Trybus et al. [1999]). Synaptic activity might influence the size of dendritic actin patches, perhaps enlarging them and creating a larger physical obstacle for microtubule based transport. Moreover, growing actin patches might have the ability to enclose transported cargoes. We found that some lysosomes were stalled for minutes at a time, based on the STED data likely to be fully trapped by the actin cytoskeleton. At the same time, calcium could influence the activity of myosins and promote stalling of cargoes for longer periods. The role of synaptic activity and corresponding calcium influx remains unaddressed, and may form a topic for further study. Additional experiments could focus on the relationship between synaptic activity/ calcium influx and the actin dynamics at actin patches. It would be interesting to study how calcium affects cellular transport, indirectly by affecting actin structures or directly by influencing motor proteins including myosins.

4.9 Materials and methods

4.9.1 Animals

For this study Wistar-Crl:WI (Han, Charles River) and Wistar Unilever HsdCpb:WU (Envigo) were used. Animals were sacrificed at E18 (pregnant rats) for primary cultures and at P7 (male rat pups) for organotypic hippocampal slice cultures. All procedures were performed in accordance with the Animal Welfare Law of the Federal Republic of Germany (Tierschutzgesetz der Bundesrepublik Deutschland, TierSchG) and with approval of the local authorities of the city-state Hamburg (Behörde für Gesundheit und Verbraucherschutz, Fachbereich Veterinärwesen, from 21.04.2015), and the animal care committee of the University Medical Center Hamburg-Eppendorf.

4.9.2 Constructs

LAMP1 (transcript-variant x1; XM_017599994.1) sequence was amplified from a rat brain cDNA library. For generation of the library, RNA was extracted with an RNeasy Plus mini kit (Qiagen) according to the manufacturer's protocol and transcribed into cDNA using SuperScript III Reverse Transcriptase (Invitrogen #18080-093) and LAMP1-specific primers. The obtained sequence was ligated to eGFP (source: pEGFP-N1, Clontech) by PCR. Then LAMP1-GFP was cloned into a pAAV2 vector (Mikhaylova et al. [2018]) with EcoRI and HindIII.

Table 4.1: List of constructs

Backbone	Promoter	Insert	Source
pAAV	Synapsin	mRuby2	Gift from T.G. Oertner
pAAV	Synapsin	LAMP1 _{rat.trans.var.x1} -eGFP	This study
pCAGGS	pCAG	FusionRed-actin _{NCB:NM_031144.3}	Gift from A. Kostyukova
pAAV	Synapsin	Actin/chromobody-TagRFP	Subcloned from ChromoTek into pAAV backbone

4.9.3 Primary hippocampal culture

Primary hippocampal cultures were prepared from E18 rat embryos. Hippocampi were dissected and cells were detached from one other with a 10 min trypsin treatment (0.25 %, Thermo Fisher Scientific #25200-056) at 37 °C, followed by physical dissociation. Cells were plated on poly-L-lysine coated glass coverslips at a density of 40000-60000 cells per 1 ml in DMEM (Gibco #10270) supplemented with 10 % fetal calf serum (Gibco #10270) and antibiotics (Thermo Fisher Scientific #215140122). 1 h after plating, the medium was replaced by BrainPhys neuronal medium including SM1 (Stem Cell Kit #5792) and 0.5 mM glutamine (Thermo Fisher Scientific #25030024). Cells were cultured in an incubator set to 37 °C, 5 % CO₂.

Primary hippocampal cultures were transfected using lipofectamine 2000 (Thermo Fisher Scientific #11668019). The DNA /lipofectamine ratio was according to manufacturer's protocol

1:2. When co-transfecting multiple plasmids, the ratio was optimized for each combination to achieve optimal expression. At the start of the transfection procedure, the original culturing medium was removed. Neurons were transfected in fresh BrainPhys medium, optionally supplemented with glutamine, but lacking supplement SM1. The transfection medium, including lipofectamine and DNA, was added for 45 min - 1 h. Afterwards, the transfection medium was exchanged to the original culturing medium. Experiments on transfected neurons were performed 1 day after transfection.

4.9.4 Immunocytochemistry

Primary neurons were fixed in 4 % Roti-Histofix/ 4 % sucrose for 10 min at RT and washed 3x in PBS. Neurons were permeabilized with 0.2 % Triton-X-100 in PBS for 10 min, and subsequently washed 3x with PBS. Coverslips were blocked for 45 min to 1 h at RT with blocking buffer (10 % horse serum, 0.1 % Triton-X-100 in PBS). Next, coverslips were incubated with primary antibody in blocking buffer at 4 °C ON. Next day, the coverslips were washed 3x with PBS and incubated for at least 1 h with secondary antibody in blocking buffer at RT. The coverslips were washed 3x with PBS. Optionally the coverslips were stained with phalloidin in either blocking buffer or PBS at 4 °C ON. All samples were mounted in Mowiol mounting medium. The Mowiol mounting medium was prepared according to the manufacture's protocol (9.6 g mowiol 4-88 (Carl-Roth), 24.0 g glycerol, 24 ml H₂O, 48 ml 0.2 M Tris pH 8.5, including 2.5 g DABCO (Sigma-Aldrich #D27802)).

Table 4.2: Primary antibodies

Antibody	Species	Source	Product number
Anti-bassoon	Mouse	Stressgen, now Enzo	ADI-VAMPS003
Anti-synaptotagmin 1 (luminal domain)	Rabbit	Synaptic Systems	105011C3
Anti-homer1	Mouse	Synaptic Systems	160011
Anti-homer1	Rabbit	Synaptic Systems	160103
Anti-gepyhrin	Mouse	Synaptic Systems	147011
Anti-MAP2	Mouse	Sigma-Aldrich	M4403
Anti- α -tubulin	Mouse	Sigma-Aldrich	T5168
Anti-LAMP1	Rabbit	Abcam	Ab24170
Anti-LAMP1	Rat	DSHB	1D4B

Table 4.3: Secondary antibodies

Antibody/reagent	Conjugate	Source	Product number
Anti-mouse	Alexa Fluor 488	Life Technologies	A11029
Anti-rabbit	Alexa Fluor 568	Life Technologies	A11036
Anti-mouse	Alexa Fluor 647	Life Technologies	A21236
Anti-mouse	Abberior Star 580	Sigma-Aldrich	52403

Table 4.3. (continued)

Antibody/reagent	Conjugate	Source	Product number
Anti-rabbit	Abberior Star 580	Sigma-Aldrich	41368
Anti-rat	Alexa Fluor 488	Molecular Probes	A11006
Phalloidin	Atto647N	Sigma-Aldrich	65906

4.9.5 Synaptotagmin antibody uptake assay

The anti-synaptotagmin-Oyster550 antibody was diluted according to manufacturer's protocol including glycerol to a concentration of 0.5 mg/ml. Primary neurons (DIV17) were incubated for 30 min with anti-synaptotagmin-Oyster550 (1:100 in culturing medium). For synaptic silencing, 1 μ M TTX (Tocris) was added directly before incubation with anti-synaptotagmin-Oyster550. After incubation, neurons were washed in culturing medium (containing 1 μ M TTX for silenced cultures) and fixed in 4 % Roti-Histofix/ 4 % sucrose. The procedure was followed by ICC for homer and actin (phalloidin-Atto647N).

4.9.6 Confocal and GATEDSTED microscopy

Confocal imaging of primary neurons was performed using a Leica TCS SP5 microscope (Leica Microsystems). The microscope was operated with Leica Applications Suite Advanced Fluorescence software. Samples were imaged using a 63x objective (Leica, HC PL APO CS2 63x/1.40 oil). Fluorophores were excited with a 488 nm Argon laser, 561 nm diode-pumped solid-state laser and a 633 nm He-Ne laser. Images were acquired at 8-bit, 1024x1024 pixel with a final pixel size of 60 nm. Images were acquired by 2x average for noise suppression, pinhole set to 1 airy unit. For z-stacks, a z-step size of 0.29 μ m was applied.

GATEDSTED images were acquired with a Leica TCS SP8-3X_{GATEDSTED} microscope (Leica Microsystems). Samples were imaged with either a 100x oil objective (Leica, HC APO CS2 100x/1.40 oil) or a 93x glycerol objective (Leica, HC APO 93x/1.30 GLYC motCORR). Excitation was provided with a pulsed WLL ranging from 470 to 670 nm. For excitation of the respective channels, the WLL was set to 650 nm for phalloidin-Atto647N, 561 nm for Abberior Star 580, and 488 nm for either Alexa Fluor 488-conjugated secondary antibodies or GFP-fusion proteins. STED was attained with a 775 nm depletion laser for Atto647N/ Abberior Star 580 and with the 592 nm depletion laser for Alexa Fluor 488/ eGFP. Emission spectra were detected at 660-730 nm for Atto647N, 580-620 nm for Abberior Star 580, and 500-530 nm for Alexa Fluor 488 or eGFP. For GATEDSTED, detector time gates were set to 0.5-6 ns for Abberior Star 580/ Atto647N and 1.5-6 ns for Alexa Fluor 488/ eGFP. Images were acquired as single planes of either 1024x1024 or 1386x1386 pixels, optical zoom factor 5 (for oil: x/y 22.73 nm, for glycerol: x/y 24.44 nm or 18.28 nm pixel size) or 6 (glycerol x/y 20.37 nm pixel size), 600 lines per second, and 16x line averaging. Corresponding confocal channels had the same settings as STED channels, except the excitation power was reduced and the detection time gates were set to 300 ps - 6 ns for all channels.

Deconvolution was performed with Huygens Professional (Scientific Volume Imaging). Within the deconvolution wizard, images were subjected to a background correction, and the signal-to-

noise ratio was set to 15 for STED and 30/ 40 for confocal laser-scanning microscopy (CLSM) images. The optimized iteration mode of the classic maximum likelihood estimation was applied until it reached a quality threshold of 0.01 for STED and 0.05 for CLSM images.

4.9.7 Live cell imaging: oblique-angle and spinning-disk microscopy

Time-lapse series and FRAP experiments were performed on a total internal reflection fluorescence (TIRF) microscope controlled by Visiview (VisitronSystems). Samples were placed on a Nikon Eclipse Ti-E microscope body and kept in focus with the built-in Nikon perfect focus system. All samples were imaged using a 100x TIRF objective (Nikon, ApoTIRF 100x/ 1.49 oil). Fluorophores were excited using a 488, 561 or 639 nm laser coupled to the microscope via an optical fiber. Sample were illuminated by highly inclined illumination obtained with an ILAS2 (GattacaSystems) spinning-TIRF system. FRAP was performed using the ILAS2 unit and a 561 nm laser, set to a higher intensity than for imaging. Emission light was collected through a quad-band filter (Chroma, 405/488/561/640), followed by a filter wheel with filters for GFP (Chroma, 525/50m) and RFP (Chroma, 595/50m). Multi-colour images were acquired sequentially on an Orca flash 4.0LT CMOS camera (Hamamatsu), pixel size 65 nm. Images were acquired with 5 s (FRAP) or 5 min intervals (time-lapse).

Transport of lysosomes, in combination with the actin cytoskeleton, was imaged with a spinning-disk microscope. The spinning-disk microscope, consisting of a Nikon Eclipse Ti-E body and a CSU-W1 spinning-disk unit, was controlled by Visiview software (VisitronSystems). Neurons were imaged using a 100x objective (Nikon, ApoTIRF 60x/ 1.45 oil). Fluorophores were excited with a 488 and 561 nm laser. Emission light was split by a 561 LP dichroic and filtered through a GFP (Chroma, 525/50m), or an mCherry filter (Chroma, 609/34m). Multi-colour images were acquired simultaneously on two EM-CCD cameras (Photometrics, Evolve 512 Delta), pixel size 85 nm. Images were acquired at 4 frames per second.

4.9.8 Analysis of actin patches

The density of actin patches, size and mean fluorescence intensity of F-actin within a given patch, the presence of cortactin and the association with homer1 were analyzed using Fiji (Schindelin et al. [2012]). 2D STED images of dendritic stretches, 13 - 32 μm in length, were used for analysis. ROIs were drawn manually in the phalloidin channel (unprocessed STED) and subsequently size, integrated and mean intensity, and cortactin integrated density were measured in the unprocessed STED channels. The differentiation between spine and shaft associated patches was based on the proximity to clearly detectable dendritic spines (not further than 0.5 μm from the spine base). PSD positive or negative patches were defined by direct association with homer1.

4.9.9 Kymograph analysis, analysis of average velocities inside and outside of actin patches

Kymographs were constructed using the KymoResliceWide plugin for Fiji. Non-overlapping dendritic stretches of 30-80 μm length were traced, using the segmented line tool. Maximum 3 dendrites were taken from the same neuron. Line thickness was chosen to cover the dendritic

shaft, but to omit spines. Trajectories in the kymographs were traced by hand using the straight line tool.

The effects of actin patches on transport of LAMP1-positive vesicle was analysed with a custom written Matlab script (MathWorks). Kymographs images for the F-actin channel were imported and a normalized intensity profile was generated from the first 100 time points. To reduce noise, the profile was filtered with a moving average filter. Actin patches were detected with the function peak prominence, the prominence was adjusted by the user and was dependent on the signal-to-noise level. Borders of the actin patches were defined as 60-75 % distance to the first minimum, separately for both slopes of the peak. To reduce experimental influences, a random control was generated. Borders of the actin patches were moved 5-15 μm (randomized) to the right. Patches that moved out of the kymograph area were added on the left site, so that the area of the kymograph covered by actin patches remained equal. Next, coordinates of displacements, manually traced in kymographs in Fiji, were imported into Matlab. Average velocity of vesicles (including stationary) was computed for inside/ outside actin patches for both the real data and the randomized control. The velocity inside actin patches might be slightly overestimated, since the positions of actin patches are stated from the kymograph analyses as t and x covering the complete dendrite thickness. Vesicles passing by patches in the 3D volume are therefore considered as inside patch regions. The analysis workflow is illustrated in Figure 4.8.

4.9.10 Data representation and statistical analysis

For representative microscopy images, brightness and contrast are linearly adjusted per channel. Statistical analysis was performed in Prism 6.05 (GraphPad). Detailed specifications about the type of test, significance levels, n numbers, and biological replicates are provided in the figure legends. Data are represented individually in dot blots or as mean \pm SEM.

5 Expansion microscopy for high resolution imaging

Contribution of others in the work stated here:

Mireia Casanovas Ferrero helped with establishing expansion microscopy in the lab. Dr. Pasquale Cervero cultured the monocytes/macrophages and provided them as a gift. Dr. Marina Mikhaylova helped with designing the experiments.

5.1 Super-resolution light microscopy

Microscopy has the general aim to obtain a detailed image of small objects. In addition, there is a strong desire for a good contrast between the studied object and other matter. For years, fluorescence microscopy has been providing an excellent tool to allow easy visualization of multiple cellular targets. Unfortunately, fluorescence microscopy is limited in resolution due to the used wavelengths. The wavelengths, ranging from ultraviolet (UV) to infra-red, limit the resolution to approximately 180 nm. During the last decades physicists, chemists, and biologists have tried and designed methods to increase the resolution of light microscopy. This led to the three main methods within 'super-resolution' light microscopy named structured illumination microscopy (SIM), single molecule localization microscopy (SMLM) and stimulated emission depletion microscopy (STED) (Gambiarotto et al. [2018], Gao et al. [2018], Halpern et al. [2017], Wang et al. [2018]). Each of them achieves, by optical and/or computational methods, a better resolution than 180 nm. SIM achieves a resolution of approximately 100 nm, SMLM and STED have a theoretically infinite resolution. In practice SIM achieves a resolution of ± 120 nm, SMLM 20 nm and STED 60 nm. Each of these techniques comes with its advantages and disadvantages, and depending on the research question one technique will stand-out. Meanwhile super-resolution microscopy has answered many biological questions, but a common drawback of these techniques is that they require expensive and highly specialized equipment.

5.2 Expansion microscopy

In the recent years the Boyden lab came up with an alternative method, increasing resolution by expanding the studied specimen (Chen et al. [2015]). The technique, named expansion microscopy, is compatible with standard fluorescence microscopes and makes it possible to reach an equivalent resolution of approximately 60 nm. The final obtained resolution is the maximum achievable resolution of the microscope systems used for acquisition, divided by the expansion factor of the specimen.

Expansion microscopy relies on the embedding of samples within expandable hydrogels (Asano et al. [2018]). Standard is the use of acrylamide gels, which swell when they are submerged in water. An advantage of expansion microscopy over other super-resolution techniques is that the resolution is evenly enhanced in all dimensions (± 4.5 times in X, Y and Z), due to the even expansion of the hydrogel in all dimensions. Image acquisition is performed similarly as for regular specimen, and does not depend on enhanced optical requirements. It does not require multiple exposures (SIM), excitation-depletion cycles (STED) or molecule-transitions (SMLM), thereby lowering the risk for photo-bleaching or indefinite dark states that compromise image quality. Based on these characteristics I proposed that expansion microscopy could be well suited for studying the cytoskeleton in three dimensions (X, Y and Z). For this reason I established expansion microscopy in the lab with the final aim to fully reconstruct the dendritic actin and microtubule cytoskeleton at a high resolution in all three dimensions (X, Y and Z).

5.3 Expansion retention microscopy on cytoskeletal structures

Expansion microscopy can be performed with DNA and fluorophore-coupled antibodies. Here I apply expansion microscopy using fluorophore-coupled antibodies. This protocol, named retention expansion microscopy, is aiming on retaining existing fluorophores within the sample. This approach has the advantage that it can be used with genetically encoded fluorophores and uses widely available substances, such as standard fluorescently labelled antibodies (Chozinski et al. [2016], Tillberg et al. [2016]). The procedure requires a regular immunostaining preceding expansion. The additional steps for retention expansion microscopy are: I) coupling of proteins with an anchoring reagent, II) casting of a gel including the specimen, III) digestion of proteins into peptides IV) and expansion of the gel. Each of the steps has to be performed well to achieve a high labelling density and even expansion (Figure 5.1).

Expansion retention microscopy is slightly different from earlier protocols for expansion microscopy. Expansion microscopy was initially performed and published with the use of DNA-conjugated antibodies and DNA hybridization (Chen et al. [2015]). This option is more challenging as it requires the use of DNA-conjugated antibodies. However, it can offer a higher resolution since the DNA strands are directly conjugated to the primary antibody (Chozinski et al. [2016], Tillberg et al. [2016]). DNA strands do not expand with the gel. In label retention microscopy, the size of secondary antibodies after expansion increases from 20 nm to a theoretical maximum of 90 nm. Hereby, spreading of the conjugated fluorophores could lower the maximum achievable resolution. In our case this is not a problem as the resolution of our microscope setup is estimated around 250 nm. The size of antibody complex (primary and secondaries) after expansion remains below the resolution limit. It could become a point of concern if expansion microscopy is performed in combination with super-resolution light microscopy techniques such as SIM, STED or SMLM (Gambarotto et al. [2018], Gao et al. [2018], Halpern et al. [2017], Wang et al. [2018]). It could also become relevant for iterative expansion microscopy, introducing a second round of gelation and expansion, or in combination with gel compositions that allow up to 10 times expansion (Chang et al. [2017], Truckenbrodt et al. [2018], Truckenbrodt et al. [2019]). Before aiming for these possibilities one should ask themselves if this is required for answering their particular biological question. Imaging at a finer resolution, or expanding the sample to extremes, introduces more challenges for image acquisition. The quantity of fluorophores per area reduces and thereby it imposes a greater challenge to obtain sufficient photons for a good acquisition. For three-dimensional acquisition of dendritic segments, working at extreme resolution would actually be a disadvantage as it would lower intensities and/or introduce extremely long acquisition. Standard label retention expansion microscopy offers here sufficient resolution and is the more practical/ better choice.

Crucial for label retention expansion microscopy is the use of an anchoring reagent. Anchoring of proteins and peptides is the first step in expansion retention microscopy. The anchoring reagent ensures coupling of proteins (secondary antibodies conjugated to a fluorophore, or fluorescent proteins) to the acrylamide gel. Here we use methacrylic acid N-hydroxysuccinimide ester (MA-NHS) as anchoring reagent (Figure 5.1B). Proteins and peptides can also be coupled by other anchoring reagents, but we preferred MA-NHS as it is cheaper than acryloyl-X (AcX)

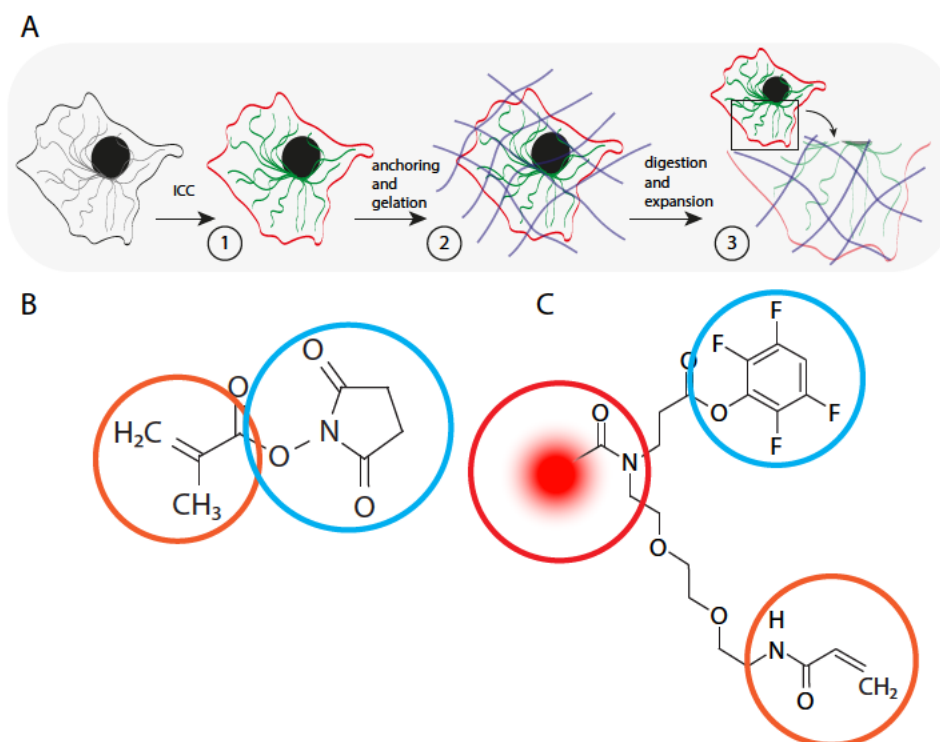


Figure 5.1: Principles of expansion microscopy and fluorophore retention strategies.

A) Graphical illustration of the protocol for expansion microscopy. 1) The first step is a standard immunostaining with primary and secondary antibodies. 2) Proteins/peptides, including fluorescently labelled antibodies, are conjugated with a linker containing an acryl group. This is followed by gelation, casting of the sample within an acrylamide gel. 3) Next, proteins in the specimen are digested into small peptides with proteinase K, followed by expansion.

B) MA-NHS used as linker to retain fluorescently labelled proteins/peptides in the acrylamide gel. Blue circle indicates the N- hydroxysuccinimide ester reactive group that is used to conjugate the methacrylic group (orange) to proteins. The methacrylic group is later incorporated within the acrylamide gel, hereby MA-NHS functions as linker between proteins/peptides and the acrylamide gel.

C) Example of a tri-linker (modified from Wen et al. [2019]). Blue circle, a reactive handle to conjugate to peptides such as phalloidin or antibodies. Orange circle indicates an acryl monomer for retention in the acrylamide gel. Red circle indicates a conjugated fluorophore. The use of tri-linkers ensures that every fluorophore has a high chance to be retained with the acrylamide gel.

and produces less background than glutaraldehyde (Chozinski et al. [2016]). MA-NHS reacts with amino groups on the proteins. In the following step, the sample is casted within an acrylamide gel. The free methacrylic group of the anchoring MA-NHS is here incorporated in the acrylamide gel. Hereby the proteins are anchored within the gel. This ensures the retention of the fluorophore signal after the steps of digestion and expansion.

For success in label retention expansion microscopy it is important to use the correct fluorophores (Min et al. [2019], Tillberg et al. [2016]). Expansion microscopy protocols are based on (bis)-acrylamide gels, which set by a radical forming polymerization process. This radical polymerization can also affect the structures of fluorescent molecules, turning them non-fluorescent. To test which fluorophores can be used for expansion microscopy I analyzed a pallet of different fluorophores (Figure 5.2). The survival of fluorophores/ fluorescence was estimated by their absorption maximum after gelation (polymerization of the gel), relative to their absorption maximum in PBS, using a spectrophotometer. Most fluorophores survived gelation well. Common cyanine-based fluorophores, such as Alexa Fluor 647, should be avoided. This is no point of concern as for each regular fluorescent channel (blue, green, red, far-red) there are well performing fluorophores (Figure 5.2A,B). However, the use of UV/blue fluorophores needs to be avoided whenever possible. Even though blue fluorophores survive gelation in acrylamide gels generally well, the acrylamide gel itself absorbs in their excitation- and partially emission spectrum (Figure 5.2C). This absorption will have a negative impact on the signal-to-noise ratio during imaging, which is for most blue fluorophores already suboptimal. This might also explain a discrepancy in survival of Alexa Fluor 405 measured within another study, in which fluorescent survival was estimated lower in expanded biological samples (Min et al. [2019]). To achieve the best image quality it is best to use fluorophores in the green, red and far-red microscopy channels.

Here I established multi-colour expansion microscopy with MA-NHS as a general linker. After testing the survival of different fluorophores, it was clear that three- or even four colour expansion microscopy is within reach. COS-7 cells were used to further optimize the technique. To label microtubules, I used primary antibodies against α -tubulin and Alexa Fluor 488 conjugated anti-mouse secondary antibodies. After testing different linking strategies and incubation periods for digestion, it became clear that linking with MA-NHS followed by ON digestion with proteinase K yielded the best results. The expansion was relative even and the fluorophores were well retained within the gel, yielding a high labelling density of the microtubules (Figure 5.3). Initial attempts to stain F-actin with phalloidin failed. The phalloidin toxin has a minimal number of amino group(s) and standard fluorescently conjugated phalloidin is incompatible with expansion microscopy. Phalloidin cannot be conjugated with MA-NHS when already conjugated to a fluorophore, and is therefore washed out during expansion of the gel. A workaround is the use of a tri-linker, which introduces an acryl-group by which fluorescently labelled phalloidin can be incorporated in the acrylamide gel (Figure 5.1C) (Wen et al. [2019]). The combination of antibody staining for microtubules and phalloidin conjugated with a tri-linker provides good labelling of the cytoskeleton in expansion microscopy (Figure 5.3).

To further explore the possibilities of expansion microscopy I continued with a multi-colour staining of a structure highly enriched in cytoskeletal elements and cell adhesions molecules: the podosome. Podosomes help cells migrate through tissue. The structure is found in macrophages

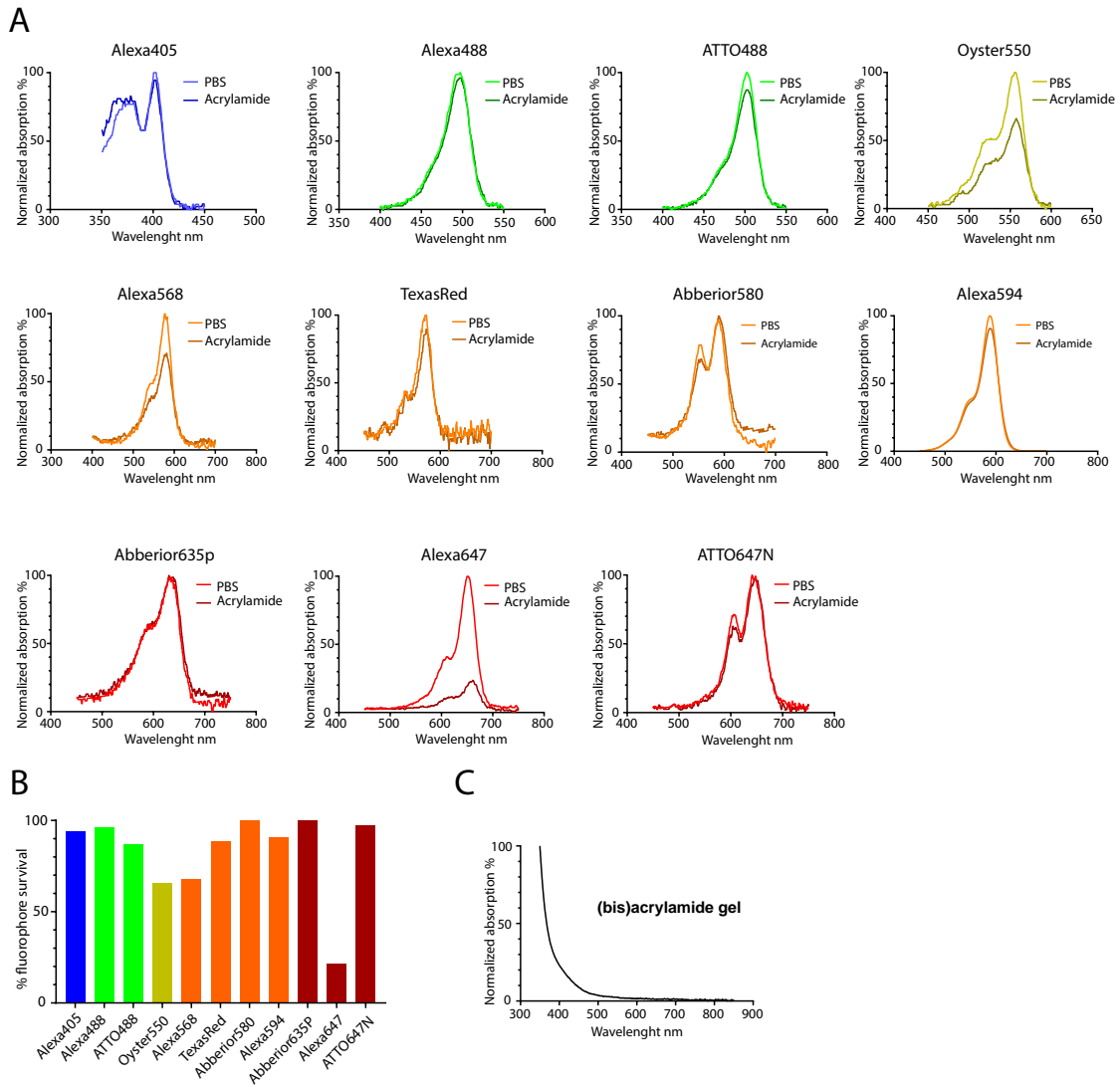


Figure 5.2: Survival of fluorophores upon gelation in an acrylamide gel.

A. Comparison of normalized absorption spectra of different fluorophores in PBS and casted in acrylamide. The absorption spectra provide a good prediction of their fluorescence survival in expansion microscopy.

B. Bar graph summarizing fluorophore survival presented in panel A.

C. Absorption spectrum of the (bis)acrylamide gel used for expansion microscopy, relative to PBS.

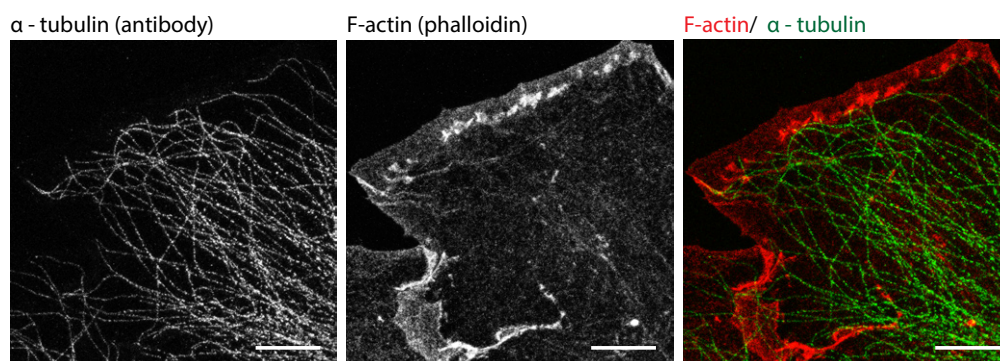


Figure 5.3: Expansion microscopy applied for visualization of the cytoskeleton of COS-7 cells. Immunostaining visualizing microtubules and the actin cytoskeleton in expanded sample. Scale bar: 10 μm .

(as stained here) but very similar structures can be found in aggressive tumour cells (Seano and Primo [2015]). I used a combination of well surviving fluorophores (Alexa Fluor 488, TexasRed and Atto647N) to expose the podosome structure at a higher resolution (Figure 5.4). When imaging the expanded podosome structures it became apparent that the coverslip displayed some auto-fluorescence in the far-red channel, which is also partly visible within the red channel. The exact cause has still to be verified, but I anticipate that the NHS-MA linker could have reacted with the coverslip coating causing the fluorescent signal. This issued no direct problems for imaging the podosomes as they are located further from the coverslip. However, if one is interested in structures located closer to the cell membrane or the coverslip it introduce problems. To solve this issue, one might avoid using the far-red channel or explore other linker strategies. I did not test whether the use of AcX and/or glutaraldehyde as anchoring reagent would solve this particular problem. On the side note, I do not anticipate any of such problems if expansion microscopy is performed on tissue or specimen cultured on non-coated coverslips.

The aim of this project was to establish a method for high-resolution three-dimensional imaging with light microscopy. The imaging of the expanded samples provided more challenges than initially anticipated. First, the samples appear extremely dim due to the spread of the fluorophores. The fluorophores are, after expansion, spread over an approximately 91 times larger volume ($4.5 \times 4.5 \times 4.5$). This makes searching in the sample difficult. Second, it proved more difficult than expected to image the expanded gel. High NA oil objectives have insufficient working distances to access all cellular structures in expanded samples. The large expansion factor in Z requires the use of larger working distance objectives. We found that the use of a 1.1 NA water immersion objective provided a good compromise. The water immersion matches the refractive index of the gel well (which consists of mainly water) and still offers sufficient resolution. Nonetheless, it remained hard to obtain three dimensional acquisitions of the sample. The enormous expansion factor imposes a challenge to grasp sufficient cellular structures in the field of view to draw conclusions. The use of a lower magnification water immersion objective helped, but obtaining high resolution three-dimensional acquisitions as planned imposed long scanning times. The long scanning times in combination with the fragile nature of the expanded gels caused movement artefacts. I was not able to reach the initial goal of imaging dendritic structures in 3D at high resolution. Nonetheless, the acquisition of single planes is faster, did

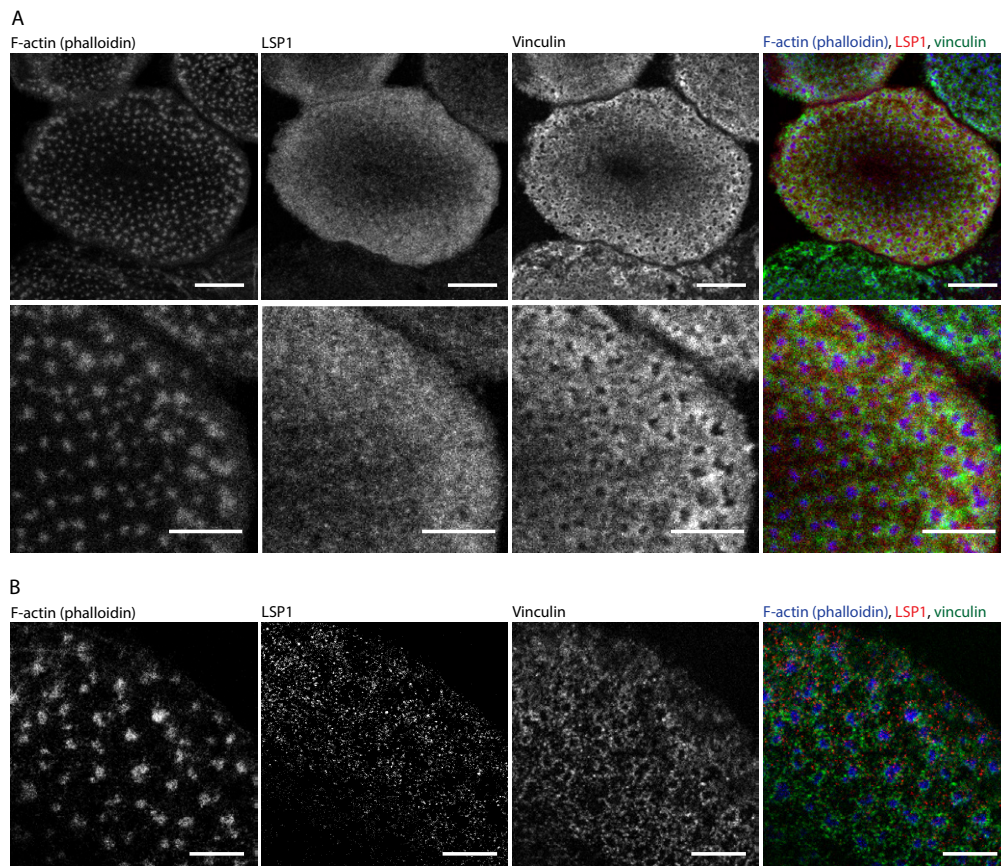


Figure 5.4: Immunostainings visualizing podosomes, non-expanded and expanded.

A. Standard immunostaining visualizing podosomes in macrophages. Cells are stained for the actin cytoskeleton (F-actin), lymphocyte-specific protein 1 (LSP1) and vinculin. Scale bar upper panels: 10 μm , lower panels: 5 μm .

B. Similar podosome structures to panel A in expansion microscopy. Expansion microscopy exposes more detail. Scale bar: 20 μm .

not suffer from moving artefacts and the increase in resolution can be clearly observed (Figure 5.4). I anticipate that further optimization of the image acquisition and gel stabilization with specifically designed imaging chambers could solve the above described difficulties, and that obtaining proper three-dimensional acquisitions is possible. One could also try to reduce the acquisition time by using faster microscopes. This could be state-of-the-art spinning-disk confocal or light-sheet microscopes. When well equipped, either of the two options could help with the acquisition of expanded samples in high-resolution and three dimensions.

While performing the work described here, other studies on the use of expansion microscopy raised criticising notes that should be taken in consideration (Gao et al. [2019], Martínez et al. [2020], Pernal et al. [2019]). The expansion factor of cellular structures appears to be not fully even. It turns out that the local cellular composition can influence the expansion factor. This occurs most likely by minor differences in gel composition. One cause might be the local protein concentration (Martínez et al. [2020]). These findings illustrate that one should be extremely careful when using expansion microscopy to study the size of cellular structures. This drawback has also been noted by its original developers, and attempts to tackle this problem with different gel composition are ongoing (Gao et al. [2019]). Nonetheless, this drawback could also offer opportunities for the future. Once it becomes clear which factors exactly influence gel expansion, this knowledge might reveal interesting information on local cellular composition.

5.4 Materials and methods

5.4.1 Cos-7 cells

Cos-7 cells were cultured in DMEM (Gibco #41966-029), supplemented with 10 % fetal bovine serum (Gibco #10270), 1x penicillin/streptomycin (Gibco #15140-122) at 37 °C, 5 % CO₂ and 95 % humidity. Cells were split twice per week. For experiments, Cos-7 cells were plated on 13 mm \varnothing coverslips (Thermo Fisher Scientific #CB00130RA0-20MNT0). Cells were fixed 1 to 2 days after plating at approximately 60-80 % confluency.

5.4.2 Macrophages

For the culturing of macrophages, monocytes were collected from human peripheral blood (University Medical Center Hamburg-Eppendorf, Hamburg, Germany) and differentiated into macrophages. Approval for the analysis of anonymized blood donations was provided by the Ethical Committee of the Ärztekammer Hamburg (Germany). The collection procedure in brief: human heparinized blood was carefully added to Lymphocyte Separation Medium (LSM 1077, PAA Laboratories #J15-004) and centrifuged at 450 x g for 30 min at 4 °C. Monocytes were collected from the buffy coat. Cells were cultured in RPMI-1640 (containing 100 units/ml penicillin, 100 μ g/ml streptomycin, 2 mM glutamine and 20 % autologous serum) at 37 °C, 5 % CO₂ and 90 % humidity. Monocytes differentiated to macrophages due to the addition of 20 % autologous serum. At DIV10-14 macrophages were fixed with 4 % PFA.

5.4.3 Immunocytochemistry

Samples were fixed in 4 %PFA/ 4 % sucrose (Roti-Histofix, Roth #A146.4), subsequently washed 3 times in 1x PBS and permeabilized in 0.2 % TritonX-100 (PanReac AppliChem #A4975) in PBS for 10 min, washed 2 times and incubated with blocking buffer, consisting of 10 % horse serum, 0.1 % TritonX-100 in PBS for 1 h at RT. Primary antibodies (1:100) were incubated ON at 4 °C. Samples were washed 3 times in PBS and incubated with secondary antibodies (1:100) for 1 h at RT. Phalloidin-TexasRed (1:40) was incubated afterwards at 4 °C ON in 1x PBS. Afterwards, samples were washed 3 times in 1x PBS. Samples were mounted in Vectashield (Vector Laboratories #H-1000) or further processed for expansion microscopy as described below (5.4.4).

Table 5.1: Materials for ICC

Target	Conjugate	Host	Clonality	Source	Product number
α -tubulin	N/A	Mouse	Monoclonal	Sigma-Aldrich	T5168
β -tubulin	N/A	Mouse	Monoclonal	Thermo Fisher Scientific	MA5-11732
Detyrosinated tubulin		Rabbit	Polyclonal	Abcam	ab48389
LSP1	N/A	Rabbit	Polyclonal	Atlas antibodies	HPA019693

Table 5.1. (continued)

Target	Conjugate	Host	Clonality	Source	Product number
Vincullin	N/A	Mouse	Monoclonal	Sigma-Aldrich	V9131
Actin (Phalloidin)	TexasRed	N/A	N/A	Chrometra	ActinRed ExM
Mouse	Alexa Fluor 488	Goat	Polyclonal	Thermo Fisher Scientific	A11029
Rabbit	Atto647N	Goat	Polyclonal	Sigma-Aldrich	40839

5.4.4 Expansion microscopy

Immunostained cells were incubated with 25 mM methacrylic acid N-hydroxysuccinimide ester (MA-NHS, Sigma #730300) in 1x PBS for 1-2 h at RT, followed by three washes with 1xPBS. Next, samples were shortly washed in monomer solution (1x PBS, 2 M NaCl, 8.625 % sodium acrylate, 2.5 % acrylamide, 0.15 % N,N'-methylenebisacrylamide). Meanwhile, the accelerator tetramethylethylenediamine (TEMED), the inhibitor 4-hydroxy-2,2,6,6-tetramethylpiperidin-1-oxyl (4-hydroxy-TEMPO) and, at last, the initiator ammonium persulfate (APS) were added to an aliquot of monomer solution to make the gel solution with final concentrations of 0.2 %, 0.01 %, and 0.2 %, respectively. Coverslips were placed on top of a droplet of gel solution with cells facing down. Gelation was allowed to proceed for 1-2 h at RT.

Samples were placed in digestion buffer (50 mM Tris (pH 8), 1 mM EDTA, 0.5 % Triton X-100, 0.9 M guanidine HCl), with 8 units/ml of Proteinase K (New England Biolabs #P8107S) added freshly. Digestion was performed at 37 °C ON.

Digested gels were placed in 92 mm \varnothing petri dishes (Sarstedt #82.1473.001) in excess volumes of doubly deionized water for 3-4 h for expansion. Water was exchanged every 20-30 min until maximum expansion was reached. The expansion factor of the complete gel was measured with a ruler and estimated to be 4.5 times. For mounting, gels were cut into smaller pieces and placed in glass bottom μ -dishes (Ibidi #81158). A glass coverslip was placed on top (Thermo Fisher Scientific #CB00180RA020MNT0), and the sides were sealed with 2 % low melting argarose (Roboklon #E0303). Deionized water was added to prevent shrinkage and dehydration.

Table 5.2: Materials for expansion microscopy

Material	Source	Product number	Step
Methacrylic acid N-hydroxysuccinimide ester	Sigma-Aldrich	730300	Anchoring
DMSO	Roth	A994.1	Anchoring
Sodium Acrylate	Sigma-Aldrich	408220	Gel solution
Acrylamide	Sigma-Aldrich	A9099	Gel solution
N,N-Methylenebisacrylamide	Sigma-Aldrich	M7279	Gel solution
Sodium chloride	VWR	27810.364	Gel solution

Table 5.2. (continued)

Material	Source	Product number	Step
N,N,N','- Tetramethylethylenediamine	Sigma-Aldrich	411019	Gel solution
4-Hydroxy-TEMPO	Sigma-Aldrich	176141	Gel solution
APS	Sigma-Aldrich	A3678	Gel solution
Tris	Sigma-Aldrich	2449.2	Protein Digestion
Ethylenediaminetetraacetic	Roth	8040.3	Protein Digestion
Triton X-100	AppliChem	A4975	Protein Digestion
Guanidine Hydrochloride	Sigma-Aldrich	G3272	Protein Digestion
Proteinase K	New England Bio- labs	P8107S	Protein Digestion
ddH ₂ O	N/A	N/A	Expansion
Petri dish 92x16 mm	Sarstedt	82.1473.001	Expansion
μ-dish (35 mm ∅, high glass bottom)	Ibidi	81158	Mounting
Low melting agarose	Roboklon	E0303	Mounting
Cover glass 18 mm ∅	Thermo Fisher Sci- entific	CB00180RA020MN	Mounting

5.4.5 Analysis of fluorophore survival

Analysis of fluorophore survival was estimated by measuring the absorption spectra of each fluorophore with a NanoDrop OneC (Thermo Fisher Scientific). Equal concentrations of fluorophore, or antibody conjugated fluorophore, were measured in 1x PBS (Roth #9150.1) and polymerized acrylamide gel. Dilutions ranged from 1:100 to 1:50. Absorption spectra were measured in 10 mm path length cuvettes (Brand #759200). Absorption spectra were corrected to baseline and measured by peak absorption. For representation, graphs are normalized to the minimum and maximum value in each dataset.

Table 5.3: Materials used for fluorophore survival analysis

Product name	Host	Clonality	Source	Product Number
Anti-synaptotagmin- Oyster550	Rabbit	Polyclonal	Synaptic Systems	105103C3
Anti-mouse- Alexa Fluor 405	Goat	Polyclonal	Abcam	Ab175660
Anti-mouse- Alexa Fluor 488	Goat	Polyclonal	Thermo Fisher Scientific	A11029
Phalloidin-Atto488	N/A	N/A	ATTO-TEC	AD 488-81
Anti-mouse- Alexa Fluor 568	Goat	Polyclonal	Thermo Fisher Scientific	A11031

Table 5.3. (continued)

Target	Host	Clonality	Source	Product Number
Phalloidin-TexasRed	N/A	N/A	Chrometra	ActinRed ExM
Anti-mouse-Abberrior Star 580	Goat	Polyclonal	Abberrior	ST580
Alexa Fluor 594-Hydrazide	N/A	N/A	Thermo Fisher Scientific	A10438
Anti-guinea pig-Abberrior Star 635P	Goat	Polyclonal	Abberrior	ST635P
Anti-mouse-Alexa Fluor 647	Goat	Polyclonal	Thermo Fisher Scientific	A21236
Anti-mouse-Atto647N	Goat	Polyclonal	Sigma-Aldrich	50185

5.4.6 Image representation

For representation the contrast of the images was linearly adjusted with Fiji. Size of the scale bar is specified in each figure legend.

6 Discussion and perspective

6.1 Synopsis

This work is focused on the dendritic neuronal cytoskeleton, and its role in protein and organelle transport. In different sets of experiments, I characterized the organisation of the dendritic cytoskeleton in combination with factors that regulate actin dynamics. At last, I looked at the influence of the dendritic actin and microtubule cytoskeleton on lysosomal transport and established expansion microscopy as an alternative approach to image the cytoskeleton at high resolution.

6.2 Caldendrin and calcium signalling

The cytoskeleton forms paths for molecular transport and provides physical supports to dendritic structures (Korobova and Svitkina [2010]). At the same time, the cytoskeleton structure is prone to remodelling (Bosch et al. [2014]). This is partially due to a balance in growth and shrinking events at the plus-end of actin filaments and microtubules. The balance between the growth and shrinking events creates a dynamic environment which facilitates the turnover of proteins, also at dendritic spines. LTP inducing synaptic activity, causing strong elevations in calcium, can break this balance and start a complete reorganisation of the cytoskeleton. This includes the activation of severing proteins and proteins regulating actin polymerization and stabilization (Bosch et al. [2014]). This type of remodelling often leads to a newly set structure and a balance in protein turnover. Such extreme remodelling is tightly regulated by calcium binding proteins namely calmodulin and caldendrin (Mikhaylova et al. [2006], Mikhaylova et al. [2018]). Calmodulin indirectly induces severing and branching of new actin filaments. On the other hand, caldendrin protects existing actin branches creating a starting point from which a new actin cytoskeleton architecture can be formed. This function appears to be essential to grow large and stable mushroom-shaped spines, characterized by a cupped shaped actin organization at the base of the spine head. The absence of caldendrin results in a disorganization of F-actin in dendritic spines and a loss in the number of large mushroom-like spines. Moreover, in the absence of caldendrin LTP declines over time (Mikhaylova et al. [2018]). The data strongly suggest that caldendrin plays an important role during strong actin modifying events, in which a new actin structure is formed. The presence of caldendrin is essential to guide actin dynamics during synaptic plasticity events and ensures long-term spine/ synaptic stability.

It is still unclear whether caldendrin plays a role in other calcium events which do not lead to long-term plasticity, namely single synaptic activations. Small calcium events could also open caldendrin to a similar extent as it activates calmodulin, since their affinity for calcium is very similar (Mikhaylova et al. [2018]). Interestingly, caldendrin is not equally distributed to every spine (Laube et al. [2002]). It is the abundance ratio calmodulin/caldendrin within spines that will determine which of the two gets predominantly activated. Thereby, the response to calcium might differ between spines. In addition, the function of caldendrin may not exclusively be the translation of calcium signals towards the actin cytoskeleton, but caldendrin might also influence the activity of motor proteins. A similar role has been illustrated for calmodulin, which can regulate myosin based transport and activity (Batters et al. [2016], Homma et al. [2000], Nascimento et al. [1996], Nguyen and Higuchi [2005], Trybus et al. [1999]). What role

caldendrin plays during non-plasticity inducing calcium events and if it has additional calcium independent roles deserves further attention and research effort.

6.3 The MPS in the neck of dendritic spines

The organisation and remodelling of branched actin in dendritic spines is well studied in contrast to the recently discovered MPS.

In this work I demonstrated the presence of the actin lattice within the neck of dendritic spines. This is an interesting finding, as the necks of dendritic spines perform an important function in isolating spine heads from the dendritic shafts. The thickness of the neck influences to which extend spines are chemically (diffusion) and electrically (membrane potential changes) compartmentalized from the connecting dendritic branch. The length and diameter of spine necks is variable but correlates with width of the spine head (Tønnesen et al. [2014]). It is therefore extremely likely that LTP and LTD events also affect the spine neck. It might well be that the MPS in the neck of spines actively regulates the spine neck diameter, or that remodelling of the MPS is required to allow changes in neck diameter to take place.

We discovered that even though the actin lattice is present throughout the full neck, β -II spectrin is not. This could be due to the inability of the antibody to reach all epitopes, or it could have a biological meaning. In a later published study it was demonstrated that, next to β -II spectrin, β -III spectrin is important for the formation of spines (Efimova et al. [2017]). β -III spectrin is, different from β -II spectrin, enriched at the base of spine, where they connect to the dendritic branch, and within spine necks. The absence of β -III spectrin results in predominantly shaft synapses (Efimova et al. [2017]). It could well be that the actin-spectrin lattice in spine necks is composed of a combination in β -II/ β -III spectrins, whereas the dendritic- and axonal MPS is mostly composed of β -II spectrin (Efimova et al. [2017]). This could make a difference for the regulation of the MPS. First studies on the regulation of the MPS highlight an important role for calpain-2 (Zhou et al. [2019]). Calpain-2 is a calcium binding protein, but can also be activated by the Erk signalling pathway downstream of epidermal growth factor (EGF) receptors. Active calpain-2 is able to cleave β -II spectrin, thereby locally disassembling the MPS. Interestingly, this regulatory process is part of a feedback mechanism. The EGF receptor in turn requires the MPS at the membrane to function. The MPS structures diffusion in the membrane and brings proteins in close proximity for protein-protein interaction, promoting signal transduction (Albrecht et al. [2016], Zhou et al. [2019]). This feedback loop has been illustrated for the MPS in axons, but there are so far no reports on the regulation at the soma, dendrites or the neck of dendritic spines. The presence of β -II and β -III spectrin in spine necks could allow differences in regulation, perhaps by differences in susceptibility for cleavage by calpain-2. This would mean that the MPS in spine necks can be regulated and disassembled independently from the dendritic MPS structure, and that the diameter of spine necks can be tuned without affecting dendrites. It should not be forgotten that β -I spectrin is also expressed within the brain, but so far no study has indicated a function within the MPS.

An alternative hypothesis is that MPS in spine necks actively participates in regulation of the spine neck diameter, e.g. by participation of myosin II. Myosin II is known to be present in structures that provide contractile forces, and has been shown to be essential to keep the mem-

brane of erythrocytes in shape (Smith et al. [2018]). Additionally, myosin II is enriched within the neck of spines, and might be able to provide contractile forces to narrow the spine neck (Tatavarty et al. [2012]). Tuning of the spine neck diameter might correlate with the activity of myosin II. This hypothesis is strengthened by the finding that myosin II inhibition severely alters spine morphology (Ryu et al. [2006]). Moreover, recent studies have shown that myosin II fulfils important functions in the MPS of the axon (Berger et al. [2018], Costa et al. [2020]). Myosin II activity is important for the formation and plasticity of the AIS as well as the diameter of the axon (Evans et al. [2017]). Interestingly, prolonged neuronal activation diminishes phosphorylation of myosin II and reduces the localization to- and shortens the overall length of the AIS (Berger et al. [2018]). This makes neurons less excitable. At the same time, phosphorylation of myosin II and also its ability to perform a stepping motion has proven essential to retain the axon diameter (Costa et al. [2020]). It may well be that a similar mechanism regulates the spine neck diameter: a mechanism in which calcium signalling regulates the phosphorylation and strength of contractile forces provided by myosin II (Adelstein and Eisenberg [1980]). It would provide a fast mechanism by which synaptic activity, calcium signalling, and myosin activity can regulate the spine neck diameter without the need of complete disassembly and re-assembly of the MPS. Such scenario would be optimal in terms of speed and cellular energy efficiency.

Similar to the regulation of the MPS, there is little known about the direct function of the actin-spectrin lattice within the spine necks. The above described regulation of the neck diameter is highly speculative. One may also hypothesize that the MPS in dendrites might have a more comparable function to the MPS in axons, i.e. serving as a platform for membrane signalling. Given that the spine neck provides relatively little membrane surface for signalling, I believe that this scenario is unlikely. Instead, the MPS might be important for providing mechanical strength. It could for example support spine shape, as the knockdown of β -III spectrin results in strong spine but no synaptic loss (Efimova et al. [2017]). Perhaps it is a combination of factors, i.e. myosin II providing tension on β - spectrins, which yields mechanical strength.

6.4 Dendritic organelle transport

The formation and maintenance of thousands of spines and synapses along the dendritic arbour require many resources, namely functional proteins. On top comes the possible need of extra resources to support LTP events. The required resources/ proteins are delivered by organelles and cellular transport. A large proportion originates from the ER and is later modified within the Golgi, organelles that are located within the soma and dendrites. Their position is rather fixed. Aside, there is a large group of smaller organelles, namely lysosomes, recycling endosomes, ER-to-Golgi intermediate compartments and Golgi-satellites, that are actively transported within dendrites. Frequently these transported organelles halt, which raises the question: What factors control the halting and active transport, and what is their purpose? Does it bring organelles to specific locations to perform their function?

Here we found that lysosomes stall at actin patches associated with synapses. These actin patches are located at the base of spines, but are also part of functional excitatory shaft synapses. Interestingly, we found that the initial stalling occurs as a result of physical hindrance; the actin cytoskeleton forms a barrier for microtubule-based transport. This might also be a first regu-

latory mechanism by which neurons control cellular transport and organelle positioning. It is well known that synaptic activity guides actin dynamics, also within the dendritic shaft (Schätzle et al. [2018]). Increased synaptic activity leads to an elaboration of the actin cytoskeleton in dendrites and this promotes microtubule entry into spines (Schätzle et al. [2018]). It could be that in this situation, the F-actin structures at the base of spines form barriers for polymerizing microtubules. In line, we never found microtubules crossing actin structures. It seems that microtubules have a higher likeliness to polymerize around actin structures rather than growing through them. As dendritic actin patches might form barriers for microtubule polymerization, they might also form the same barrier for microtubule-based transport. The size and complexity of the actin patches might determine the effectiveness of these barriers, and synaptic activity might be the main regulator.

In our data we also found a population of lysosomes that were not mobile during the imaging period (3 minutes). It is very unlikely that these lysosomes are permanently stalled, since longer imaging sessions show a 100% mobile lysosome fraction (data not shown). We have the impression that the longer stalling lysosomes are closer embedded within the actin structures. They might be surrounded by ongoing actin polymerization. The only possibility for the lysosome to be released, would be a reduction in actin polymerization. These findings further suggest that the regulation of dendritic patches (size and complexity) contributes to the organization of molecular transport.

Above I illustrated that the fine actin cytoskeleton at dendritic segments has a large influence on cellular trafficking. However, cellular trafficking exceeds single dendritic segments and takes place over larger cellular compartments. Proteins can be distributed within cells in two ways: by motor proteins and diffusion. Cellular transport via motor proteins is a form of active transport; diffusion is a classical form of entropy. Where diffusion takes place, it is evening concentrations. Diffusion is important for many cellular processes. For example, diffusion of actin and tubulin monomers creates an even concentration across the cell volume and ensures that monomers are never a limiting factor for F-actin and microtubule growth. Moreover, it is important in tuning synaptic strength. Plasticity-related proteins can diffuse out of one spine towards neighbouring spines, probing them for synaptic strengthening (Murakoshi et al. [2011]). Transport by motor proteins is different. It is an active process that continuously requires ATP as an energy source. The fact that this system uses energy means that it can create and maintain concentration gradients. It can force cargoes to go towards specific areas, which are, based on protein concentration or entropy levels, unfavourable. Processes like these are frequently found in neurons. A good example is the filtering at the AIS via motor proteins. The AIS in combination with ATP consuming motor proteins is able to create a strong molecule bias within neurons (Leterrier [2018], Song et al. [2009], Watanabe et al. [2012]). Hereby, e.g. NMDA receptor GluN2B subunits are highly concentrated within the dendrites and rarely found within the axon (Song et al. [2009]), while other cargoes, including transport vesicles containing the synaptic vesicle protein VAMP2, are enriched within the axon (Song et al. [2009]). These concentration differences between the axon and dendrites are actively maintained by continuous transport of new proteins to either of the two compartments. If continuous transport would not take place, the gradients would eventually fade away due to protein diffusion and degradation. In other words, cells use active transport to force and maintain concentration differences, which could well be the case for lyso-

somes -perhaps not only for a segregation between the axonal and dendritic compartment, but also locally within cellular compartments.

Lysosomal transport takes place by motor proteins. Thereby the position of lysosomes can be actively steered. We found that besides kinesin family member 5c and dynein, lysosomes are bound by myosin V and VI. Myosins are stronger than kinesins, and when it comes to a tug-of-war, myosin can overpower active kinesins (Janssen et al. [2017], Kapitein et al. [2013], Schroeder III et al. [2010]). We found that for lysosomes, myosin V activity promotes longer stalling periods. The combined regulation of dendritic actin dynamics and motor protein activity influences the final positioning of lysosomes. Similar mechanisms and transport kinetics might apply to other dendritic cargoes. Dendritic cargoes are excluded from the axon by an interaction of myosin V with actin located in the AIS. Therefore it is likely that many dendritic cargoes are bound by myosin V (Janssen et al. [2017]). The exact composition of motor proteins (number and family member(s) of kinesins, dyneins and myosins) present at organelles could introduce some differences in transport kinetics between organelle types. The overall interplay of different motor proteins, their exact time of activation, their strength and the organisation of the cytoskeleton plays an important role in guiding organelles to locations of importance.

A factor that can influence the activity of motor proteins is calcium. Increased levels of calcium as a result of synaptic signalling have been shown to promote myosin activity (Batters et al. [2016], Shen et al. [2016], Wang et al. [2008]). The activation of myosins can strongly affect the transport of organelles. In case of lysosomes, myosin V is contributing by elongating stalling times. Here a role for calcium regulation is not excluded. The role of calcium is especially interesting in relation to functional excitatory shaft synapses. Shaft synapses are, in contrast to spine synapses, not isolated by a spine neck. When activated, resulting calcium influx is directly rising calcium levels inside the dendritic shaft. This could have direct implications on dendritic transport. Shaft synapses might play a crucial role in controlling dendritic trafficking.

Calcium signalling is a strong candidate but probably not the only signalling pathway that regulates cellular trafficking. In particular in neurons, since neurons frequently fire action potentials. Action potentials induce strong cell-wide calcium elevations via back-propagating action potentials, which could interfere with all calcium dependent organelle trafficking. Tuning of local transport, e.g. towards active synapses, would hereby be disturbed. Therefore, it could well be that also other signalling cascades influence motor protein activity and organelle transport, especially at particular cellular segments. Highly speculative, this might start with extracellular signalling pathways including e.g. BDNF or endocannabinoid signalling, resulting in possible activation of motor proteins (Kondo et al. [2012]). These molecules might be co-released with neurotransmitters from the presynapse and guide trafficking in the postsynaptic cell to dendritic segments that harbour active synapses. The dendritic segments might accumulate more organelles and locally boost protein turnover.

The exact function of organelle stalling at actin patches has not been clarified yet. It can well be that the stalling of organelles is helpful for them to fulfil their function. When stalled, organelles might become active. This could happen when multiple different organelles stall at the same location, interact and share content. For example, it has been proposed that late endosomes can transition into mature lysosomes upon fusion with Golgi-derivates, which provide hydrolases (Ferguson [2018]). Stalling of organelles could also have another purpose. It could

be that organelles are always active and that stalling of an organelle concentrates its focus of activity towards a particular cellular area. Either of the options can enhance the protein turnover within subcellular areas. Which of these possibilities holds true might also depend on the specific type of organelle studied.

From the work presented here one could follow up in diverse directions. One can further dissect the factors that control dendritic organelle transport or clarify the relationship between synaptic dynamics and lysosome function.

Transport in cells includes many different factors: from the organisation of the cytoskeleton (including the modifications of the tracks) to motor interplay at cargoes. Here we looked at lysosomes as a model cargo. Trafficking of lysosomes displays kinetics attributed to the involvement of kinesins, dyneins, and myosins, and interplays with both the microtubule and actin cytoskeleton. To further understand the 'rules' of cellular trafficking, we would have to further dissect each component: the contribution of tracks (e.g. microtubule modifications) and the different motor proteins, and how each of them is regulated. In which manner are motor proteins regulated by calcium? Are there other signalling molecules and pathways to consider? In addition, how do modifications of the tracks influence motor proteins? Do motor proteins have preferences for certain microtubule modifications (Guardia et al. [2016], Tas et al. [2017]), and on what time-scale are these modifications regulated and steer transport? I propose that these types of questions could be well studied with the use of *in vitro* models or with the isolation of cellular cytoskeletons.

That fact that actin patches are part of synaptic structures, and at the same time influence lysosome transport, strongly suggest that intracellular trafficking is coupled to synaptic activity. The work presented in this thesis could be extended by e.g. knocking down lysosomal enzymes and studying the effect on synaptic maintenance and plasticity. In case of lysosomes, it is possible to inhibit enzyme function by pharmacologically preventing acidification (Goo et al. [2017]). One could also try to inhibit organelle functions by targeting photosensitizing proteins (e.g. KillerRed) to organelles of interest and thereby heavily oxidizing and destroying proteins (Bulina et al. [2006]). Additionally, it would be an options to remove organelles from or restrict them to specific dendritic locations by e.g. light-induced transport (Bergeijk et al. [2015]). These experiments could show if, or which organelles are required to maintain and/ or tune synaptic strength.

At last there is the open question whether organelles would support single synapses or if their reach ranges down the length of dendritic segments, affecting multiple synapses at once. Similar to local protein diffusion and translation (Murakoshi et al. [2011], Govindarajan et al. [2006], Govindarajan et al. [2011]), organelle transport may facilitate clustered synaptic plasticity. The two might also be tightly coupled. It was recently found that lysosomes can co-transport mRNA (Liao et al. [2019]). mRNA is attached to the lysosome by the protein annexin A11, which functions by a calcium-dependent lipid interaction. These findings suggests that local protein translation might depend on organelle transport. Organelle transport and positioning might have a large influence on synaptic plasticity, and on the computational weight of dendritic segments in terms of their ability to activate the neuron. This would reflect on the information flow within neuronal networks, hallmark of storage and retrieval of memories. Whether the positioning and function of organelles is decisive for 'synaptic learning rules' remains to be seen.

References

- R. S. Adelstein and E. Eisenberg. Regulation and kinetics of the actin-myosin-ATP interaction. *Annual Review of Biochemistry*, 49(1):921–956, 1980.
- B. Alberts, A. Johnson, J. Lewis, M. Raff, K. Roberts, and P. Walter. Chapter 16 - The Cytoskeleton. In *Molecular Biology of the Cell, fifth edition*, pages 965–1052. Garland Science, Taylor & Francis Group, 2008.
- D. Albrecht, C. M. Winterflood, M. Sadeghi, T. Tschager, F. Noé, and H. Ewers. Nanoscopic compartmentalization of membrane protein motion at the axon initial segment. *Journal of Cell Biology*, 215(1):37–46, 2016.
- S. M. Asano, R. Gao, A. T. Wassie, P. W. Tillberg, F. Chen, and E. S. Boyden. Expansion microscopy: Protocols for imaging proteins and RNA in cells and tissues. *Current Protocols in Cell Biology*, 80(1):E56, 2018.
- J. Bär, O. Kobler, B. van Bommel, and M. Mikhaylova. Periodic F-actin structures shape the neck of dendritic spines. *Scientific reports*, 6:37136, 2016.
- C. Batters, D. Brack, H. Ellrich, B. Averbek, and C. Veigel. Calcium can mobilize and activate myosin-VI. *Proceedings of the National Academy of Sciences of the United States of America*, 113(9):E1162–E1169, 2016.
- P. V. Bergeijk, M. Adrian, C. C. Hoogenraad, and L. C. Kapitein. Optogenetic control of organelle transport and positioning. *Nature*, 518(7537):111–114, 2015.
- S. L. Berger, A. Leo-Macias, S. Yuen, L. Khatri, S. Pfenning, Y. Zhang, E. Agullo-Pascual, M.-S. Zhu, E. Rothenberg, C. Melendez-Vasquez, M. Delmar, C. Leterrier, and J. L. Salzer. Localized myosin ii activity regulates assembly and plasticity of the axon initial segment. *Neuron*, 97:555 – 570, 2018.
- G. Q. Bi and M.-m. Poo. Synaptic modifications in cultured hippocampal neurons: Dependence on spike timing, synaptic strength, and postsynaptic cell type. *Journal of Neuroscience*, 18(24):10464–10472, 1998.
- M. Bosch, J. Castro, T. Saneyoshi, H. Matsuno, M. Sur, and Y. Hayashi. Structural and molecular remodeling of dendritic spine substructures during long-term potentiation. *Neuron*, 82(2):444–459, 2014.
- M. Bucher, T. Fanutza, and M. Mikhaylova. Cytoskeletal makeup of the synapse: shaft versus spine. *Cytoskeleton*, 77:55 – 64, 2019.
- M. E. Bulina, K. A. Lukyanov, O. V. Britanova, D. Onichtchouk, S. Lukyanov, and D. M. Chudakov. Chromophore-assisted light inactivation (CALI) using the phototoxic fluorescent protein KillerRed. *Nature Protocols*, 1(2):947–953, 2006.

- J. K. Burkhardt. The role of microtubule-based motor proteins in maintaining the structure and function of the Golgi complex. *Biochimica et Biophysica Acta - Molecular Cell Research*, 1404(1-2):113–126, 1998.
- T. J. Byers and D. Branton. Visualization of the protein associations in the erythrocyte membrane skeleton. *Proceedings of the National Academy of Sciences of the United States of America*, 82(18):6153–6157, 1985.
- J. B. Chang, F. Chen, Y. G. Yoon, E. E. Jung, H. Babcock, J. S. Kang, S. Asano, H. J. Suk, N. Pak, P. W. Tillberg, A. T. Wassie, D. Cai, and E. S. Boyden. Iterative expansion microscopy. *Nature Methods*, 14(6):593–599, 2017.
- F. Chen, P. W. Tillberg, and E. S. Boyden. Expansion microscopy. *Science*, 347(6221):543–548, 2015.
- R. Chéreau, G. E. Saraceno, J. Angibaud, D. Cattaert, and U. V. Nägerl. Superresolution imaging reveals activity-dependent plasticity of axon morphology linked to changes in action potential conduction velocity. *Proceedings of the National Academy of Sciences of the United States of America*, 114(6):1401–1406, 2017.
- T. J. Chozinski, A. R. Halpern, H. Okawa, H. J. Kim, G. J. Tremel, R. O. Wong, and J. C. Vaughan. Expansion microscopy with conventional antibodies and fluorescent proteins. *Nature Methods*, 13(6):485–488, 2016.
- D. E. Clapham. Calcium signaling. *Cell*, 131(6):1047–1058, 2007.
- A. R. Costa, S. C. Sousa, R. Pinto-Costa, J. C. Mateus, C. D. Lopes, A. C. Costa, D. Rosa, D. Machado, L. Pajuelo, X. Wang, F.-q. Zhou, A. J. Pereira, P. Sampaio, B. Y. Rubinstein, I. Mendes Pinto, M. Lampe, P. Aguiar, and M. M. Sousa. The membrane periodic skeleton is an actomyosin network that regulates axonal diameter and conduction. *eLife*, 9:e55471, 2020.
- C. A. Denny, M. A. Kheirbek, E. L. Alba, K. F. Tanaka, R. A. Brachman, K. B. Laughman, N. K. Tomm, G. F. Turi, A. Losonczy, and R. Hen. Hippocampal memory traces are differentially modulated by experience, time, and adult neurogenesis. *Neuron*, 83(1):189–201, 2014.
- N. D. Derr, B. S. Goodman, R. Jungmann, A. E. Leschziner, W. M. Shih, and S. L. Reck-Peterson. Tug-of-war in motor protein ensembles. *Science*, 338(November 2):662–666, 2012.
- E. D’Este, D. Kamin, F. Göttfert, A. El-Hady, and S. W. Hell. Sted nanoscopy reveals the ubiquity of subcortical cytoskeleton periodicity in living neurons. *Cell Reports*, 10:1246–1251, 2015.
- E. D’Este, D. Kamin, C. Velte, F. Göttfert, M. Simons, and S. W. Hell. Subcortical cytoskeleton periodicity throughout the nervous system. *Scientific Reports*, 6, 2016.
- N. Efimova, F. Korobova, M. C. Stankewich, A. H. Moberly, D. B. Stolz, J. Wang, A. Kashina, and M. Ma. β III Spectrin is necessary for formation of the constricted neck of dendritic spines and regulation of synaptic activity in neurons. *Journal of Neuroscience*, 37(27):6442–6459, 2017.
- S. A. Endow, F. J. Kull, and H. Liu. Kinesins at a glance. *Journal of Cell Science*, 123(20):3420–3424, 2010.

- M. Esteves da Silva, M. Adrian, P. Schätzle, J. Lipka, T. Watanabe, S. Cho, K. Futai, C. J. Wierenga, L. C. Kapitein, and C. C. Hoogenraad. Positioning of AMPA receptor-containing endosomes regulates synapse architecture. *Cell Reports*, 13(5):933–943, 2015.
- M. D. Evans, C. Tufo, A. S. Dumitrescu, and M. S. Grubb. Myosin ii activity is required for structural plasticity at the axon initial segment. *Developmental Neuroscience*, 46:1751–1757, 2017.
- S. M. Ferguson. Axonal transport and maturation of lysosomes. *Current Opinion in Neurobiology*, 51:45 – 51, 2018.
- M. A. Franker, M. Esteves da Silva, R. P. Tas, E. Tortosa, Y. Cao, C. P. Frias, A. F. Janssen, P. S. Wulf, L. C. Kapitein, and C. C. Hoogenraad. Three-step model for polarized sorting of KIF17 into dendrites. *Current Biology*, 26(13):1705–1712, 2016.
- N. A. Frost, H. Shroff, H. Kong, E. Betzig, and T. A. Blanpied. Single-molecule discrimination of discrete perisynaptic and distributed sites of actin filament assembly within dendritic spines. *Neuron*, 67(1):86–99, 2010.
- M.-m. Fu and E. L. Holzbaur. Integrated regulation of motor-driven organelle transport by scaffolding proteins. *Trends in Cell Biology*, 24(10):564–574, 2014.
- D. Gambarotto, F. U. Zwettler, M. Cernohorska, D. Fortun, S. Borgers, J. Heine, J. G. Schloetel, M. Reuss, M. Unser, E. S. Boyden, M. Sauer, V. Hamel, and P. Guichard. Imaging beyond the super-resolution limits using ultrastructure expansion microscopy (UltraExM). *BioRxiv*, pages 1–24, 2018.
- F. Gambino, S. Pagès, V. Kehayas, D. Baptista, R. Tatti, A. Carleton, and A. Holtmaat. Sensory-evoked LTP driven by dendritic plateau potentials *in vivo*. *Nature*, 515(7525):116–119, 2014.
- M. Gao, R. Maraschini, O. Beutel, A. Zehtabian, B. Eickholt, A. Honigmann, and H. Ewers. Expansion stimulated emission depletion microscopy (ExSTED). *ACS Nano*, 12(5):4178–4185, 2018.
- R. Gao, C.-C. J. Yu, L. Gao, K. D. Piatkevich, R. L. Neve, S. Upadhyayula, and E. S. Boyden. A highly homogeneous expansion microscopy polymer composed of tetrahedron-like monomers. *BioRxiv*, 1:814111, 2019.
- C. E. Gee, I. Ohmert, S. J. Wiegert, and T. G. Oertner. Preparation of slice cultures from rodent hippocampus. *Cold Spring Harbor Protocols*, 1:126 – 130, 2017.
- M. S. Goo, L. Sancho, N. Slepak, D. Boassa, T. J. Deerinck, M. H. Ellisman, B. L. Bloodgood, and G. N. Patrick. Activity-dependent trafficking of lysosomes in dendrites and dendritic spines. *Journal of Cell Biology*, 216(8):2499–2513, 2017.
- A. Govindarajan, R. J. Kelleher, and S. Tonegawa. A clustered plasticity model of long-term memory engrams. *Nature Reviews Neuroscience*, 7(7):575–583, 2006.
- A. Govindarajan, I. Israely, S. Y. Huang, and S. Tonegawa. The dendritic branch is the preferred integrative unit for protein synthesis-dependent LTP. *Neuron*, 69(1):132–146, 2011.
- R. Green and E. J. Rogers. Chapter 28: Transformation of chemically competent *E. coli*. In *Methods in enzymology*, volume 529, pages 329–336. Elsevier, 2013.

- C. M. Guardia, G. G. Farías, R. Jia, J. Pu, and J. S. Bonifacino. BORC functions upstream of kinesins 1 and 3 to coordinate regional movement of lysosomes along different microtubule tracks. *Cell Reports*, 17:1950–1961, 2016.
- A. R. Halpern, G. C. Alas, T. J. Chozinski, A. R. Paredez, and J. C. Vaughan. Hybrid structured illumination expansion microscopy reveals microbial cytoskeleton organization. *ACS Nano*, 11(12):12677–12686, 2017.
- J. A. Hammer and W. Wagner. Functions of class V myosins in neurons. *Journal of Biological Chemistry*, 288(40):28428–28434, 2013.
- B. Han, R. Zhou, C. Xia, and X. Zhuang. Structural organization of the actin-spectrin-based membrane skeleton in dendrites and soma of neurons. *Proceedings of the National Academy of Sciences*, 114(32):E6678–E6685, 2017.
- C. D. Harvey and K. Svoboda. Locally dynamic synaptic learning rules in pyramidal neuron dendrites. *Nature*, 450(7173):1195–1200, 2007.
- C. D. Harvey, R. Yasuda, H. Zhong, and K. Svoboda. The spread of Ras activity. *Science*, 321(July):136–140, 2008.
- J. He, R. Zhou, Z. Wu, M. A. Carrasco, P. T. Kurshan, J. E. Farley, D. J. Simon, G. Wang, B. Han, J. Hao, E. Heller, M. R. Freeman, K. Shen, T. Maniatis, M. Tessier-Lavigne, and X. Zhuang. Prevalent presence of periodic actin-spectrin-based membrane skeleton in a broad range of neuronal cell types and animal species. *Proceedings of the National Academy of Sciences*, 113(21):6029–6034, 2016.
- M. C. Hendershott and R. D. Vale. Regulation of microtubule minus-end dynamics by CAM-SAPs and patronin. *Proceedings of the National Academy of Sciences of the United States of America*, 111(16):5860–5865, 2014.
- K. Homma, J. Saito, R. Ikebe, and M. Ikebe. Ca^{2+} -dependent regulation of the motor activity of myosin V. *Journal of Biological Chemistry*, 275(44):34766–34771, 2000.
- S. Honnappa, S. M. Gouveia, A. Weisbrich, F. F. Damberger, N. S. Bhavesh, H. Jawhari, I. Grigoriev, F. J. van Rijssel, R. M. Buey, A. Lawera, I. Jelesarov, F. K. Winkler, K. Wüthrich, A. Akhmanova, and M. O. Steinmetz. An EB1-binding motif acts as a microtubule tip localization signal. *Cell*, 138(2):366–376, 2009.
- P. Hotulainen and C. C. Hoogenraad. Actin in dendritic spines: connecting dynamics to function. *Journal of Cell Biology*, 189(4):619–629, 05 2010.
- D. Jaarsma and C. C. Hoogenraad. Cytoplasmic dynein and its regulatory proteins in Golgi pathology in nervous system disorders. *Frontiers in Neuroscience*, 9(OCT):1–9, 2015.
- C. Janke and M. Kneussel. Tubulin post-translational modifications: Encoding functions on the neuronal microtubule cytoskeleton. *Trends in Neurosciences*, 33(8):362–372, 2010.
- A. F. J. Janssen, R. P. Tas, P. van Bergeijk, R. Oost, C. C. Hoogenraad, and L. C. Kapitein. Myosin-V induces cargo immobilization and clustering at the axon initial segment. *Frontiers in Cellular Neuroscience*, 11, 2017.

- K. Jiang, S. Hua, R. Mohan, I. Grigoriev, K. W. Yau, Q. Liu, E. A. Katrukha, A. F. Altelaar, A. J. Heck, C. C. Hoogenraad, and A. Akhmanova. Microtubule minus-end stabilization by polymerization-driven CAMSAP deposition. *Developmental Cell*, 28(3):295–309, 2014.
- S. A. Josselyn and S. Tonegawa. Memory engrams: Recalling the past and imagining the future. *Science*, 367(6473), 2020.
- L. C. Kapitein, P. Van Bergeijk, J. Lipka, N. Keijzer, P. S. Wulf, E. A. Katrukha, A. Akhmanova, and C. C. Hoogenraad. Myosin-V opposes microtubule-based cargo transport and drives directional motility on cortical actin. *Current Biology*, 23(9):828–834, 2013.
- E. A. Katrukha, M. Mikhaylova, H. X. Van Brakel, P. M. Van Bergen En Henegouwen, A. Akhmanova, C. C. Hoogenraad, and L. C. Kapitein. Probing cytoskeletal modulation of passive and active intracellular dynamics using nanobody-functionalized quantum dots. *Nature Communications*, 8, 2017.
- N. Kaul, V. Soppina, and K. J. Verhey. Effects of α -tubulin K40 acetylation and detyrosination on kinesin-1 motility in a purified system. *Biophysical Journal*, 106(12):2636–2643, 2014.
- R. Kaushik, K. M. Grochowska, I. Butnaru, and M. R. Kreutz. Protein trafficking from synapse to nucleus in control of activity-dependent gene expression. *Neuroscience*, 280:340–350, 2014.
- T. Kitamura, S. K. Ogawa, D. S. Roy, T. Okuyama, M. D. Morrissey, L. M. Smith, R. L. Recondo, and S. Tonegawa. Engrams and circuits crucial for systems consolidation of a memory. *Science*, 356(6333):73–78, 2017.
- M. Kneussel and W. Wagner. Myosin motors at neuronal synapses: Drivers of membrane transport and actin dynamics. *Nature Reviews Neuroscience*, 14(4):233–247, 2013.
- M. Kondo, Y. Takei, and N. Hirokawa. Motor protein KIF1A is essential for hippocampal synaptogenesis and learning enhancement in an enriched environment. *Neuron*, 73:743 – 757, 2012.
- A. Konietzny. *Of Road Blocks and Loading Bays - Control Mechanisms of Dendritic Cargo Trafficking*. PhD thesis, Universität Hamburg, 2020.
- A. Konietzny, J. Bär, and M. Mikhaylova. Dendritic actin cytoskeleton: structure, functions, and regulations. *Frontiers in Cellular Neuroscience*, 11, 2017.
- F. Korobova and T. Svitkina. Molecular Architecture of Synaptic Actin Cytoskeleton in Hippocampal Neurons Reveals a Mechanism of Dendritic Spine Morphogenesis. *Molecular Biology of the Cell*, 21(1):165–176, 2010.
- M. Koskinen and P. Hotulainen. Measuring F-actin properties in dendritic spines. *Frontiers in Neuroanatomy*, 8, 2014.
- D. N. Krementsov, E. B. Krementsova, and K. M. Trybus. Myosin V: Regulation by calcium, calmodulin, and the tail domain. *Journal of Cell Biology*, 164(6):877–886, 2004.
- G. Laube, C. I. Seidenbecher, K. Richter, D. C. Dieterich, B. Hoffmann, M. Landwehr, K. H. Smalla, C. Winter, T. M. Böckers, G. Wolf, E. D. Gundelfinger, and M. R. Kreutz. The neuron-specific Ca^{2+} -binding protein caldendrin: Gene structure, splice isoforms, and expression in

- the rat central nervous system. *Molecular and Cellular Neuroscience*, 19(3):459–475, 2002.
- S. C. Leite, P. Sampaio, V. F. Sousa, J. Nogueira-Rodrigues, R. Pinto-Costa, L. L. Peters, P. Brites, and M. M. Sousa. The actin-binding protein α -adducin is required for maintaining axon diameter. *Cell Reports*, 15(3):490–498, 2016.
- C. Leterrier. The axon initial segment: an updated viewpoint. 38(9):2135–2145, 2018.
- Y. C. Liao, M. S. Fernandopulle, G. Wang, H. Choi, L. Hao, C. M. Drerup, R. Patel, S. Qamar, J. Nixon-Abell, Y. Shen, W. Meadows, M. Vendruscolo, T. P. Knowles, M. Nelson, M. A. Czekalska, G. Musteikyte, M. A. Gachechiladze, C. A. Stephens, H. A. Pasolli, L. R. Forrest, P. St George-Hyslop, J. Lippincott-Schwartz, and M. E. Ward. RNA granules hitchhike on lysosomes for long-distance transport, using annexin A11 as a molecular tether. *Cell*, 179(1):147–164.e20, 2019.
- M. H. Longair, D. A. Baker, and J. D. Armstrong. Simple neurite tracer: Open source software for reconstruction, visualization and analysis of neuronal processes. *Bioinformatics*, 27(17):2453–2454, 2011.
- C. Lüscher and R. C. Malenka. NMDA receptor-dependent long-term potentiation and long-term depression (LTP/LTD). *Cold Spring Harbor Perspectives in Biology*, 4:1–16, 2012.
- G. F. Martínez, N. G. Gazal, G. Quassollo, A. M. Szalai, E. D. Cid-Pellitero, T. M. Durcan, E. A. Fon, M. Bisbal, F. D. Stefani, and N. Unsain. Quantitative expansion microscopy for the characterization of the spectrin periodic skeleton of axons using fluorescence microscopy. *Scientific Reports*, 10(1), 2020.
- M. Matsuzaki, N. Honkura, G. C. Ellis-Davies, and H. Kasai. Structural basis of long-term potentiation in single dendritic spines. *Nature*, 429:761–766, 2014.
- B. Mel, J. Schiller, and P. Poirazi. Synaptic plasticity in dendrites: complications and coping strategies. *Current Opinion in Neurobiology*, 43:177 – 186, 2017.
- M. Melak, M. Plessner, and R. Grosse. Actin visualization at a glance. *Journal of Cell Science*, 130(3):525–530, 2017.
- M. Mikhaylova, Y. Sharma, C. Reissner, F. Nagel, P. Aravind, B. Rajini, K. H. Smalla, E. D. Gundelfinger, and M. R. Kreutz. Neuronal Ca^{2+} signaling via caldendrin and calneurons. *Biochimica et Biophysica Acta - Molecular Cell Research*, 1763(11):1229–1237, 2006.
- M. Mikhaylova, S. Bera, O. Kobler, R. Frischknecht, and M. R. Kreutz. A dendritic Golgi satellite between ERGIC and retromer. *Cell Reports*, 14(2):189–199, 2016.
- M. Mikhaylova, J. Bär, B. van Bommel, P. Schätzle, P. A. YuanXiang, R. Raman, J. Hradsky, A. Konietzny, E. Y. Loktionov, P. P. Reddy, J. Lopez-Rojas, C. Spilker, O. Kobler, S. A. Raza, O. Stork, C. C. Hoogenraad, and M. R. Kreutz. Caldendrin directly couples postsynaptic calcium signals to actin remodeling in dendritic spines. *Neuron*, 97(5):1110–1125.e14, 2018.
- K. Min, I. Cho, M. Choi, and J. B. Chang. Multiplexed expansion microscopy of the brain through fluorophore screening. *Methods*, (February):0–1, 2019.
- H. Murakoshi, H. Wang, and R. Yasuda. Local, persistent activation of rho GTPases during plasticity of single dendritic spines. *Nature*, 472(7341):100–106, 2011.

- A. A. Nascimento, R. E. Cheney, S. B. Tauhata, R. E. Larson, and M. S. Mooseker. Enzymatic characterization and functional domain mapping of brain myosin-V. *Journal of Biological Chemistry*, 271(29):17561–17569, 1996.
- H. A. Nguyen and H. Higuchi. Motility of myosin V regulated by the dissociation of single calmodulin. *Nature Structural and Molecular Biology*, 12(2):127–132, 2005.
- A. F. Oliveira and R. Yasuda. Neurofibromin is the major ras inactivator in dendritic spines. *Journal of Neuroscience*, 34(3):776–783, 2014.
- O. F. Omotade, S. L. Pollit, and J. Q. Zheng. Actin-based growth cone motility and guidance. *Molecular and Cellular Neuroscience*, 84:4–10, 2017.
- M. Park. AMPA receptor trafficking for postsynaptic potentiation. *Frontiers in Cellular Neuroscience*, 12(October):1–10, 2018.
- S. P. Pernal, A. Liyanaarachchi, D. L. Gatti, B. Formosa, R. Pulvender, E. R. Kuhn, R. Ramos, A. R. Naik, K. George, S. Arslanturk, D. J. Taatjes, and B. P. Jena. Differential expansion microscopy. *BioRxiv*, page 699579, 2019.
- D. Purves, G. J. Augusine, D. Fitzpatrick, W. C. Hall, A.-S. LaMantia, and L. E. White. Chapter 23: Construction of Neuronal Circuits. In *Neuroscience, fifth edition*, pages 507–536. Sinauer Associates, 2012.
- C. S. Rex, C. F. Gavin, M. D. Rubio, E. A. Kramar, L. Y. Chen, Y. Jia, R. L. Huganir, N. Muzyczka, C. M. Gall, C. A. Miller, G. Lynch, and G. Rumbaugh. Myosin IIb regulates actin dynamics during synaptic plasticity and memory formation. *Neuron*, 67(4):603–617, 2010.
- J. I. Rossato, A. Moreno, L. Genzel, M. Yamasaki, T. Takeuchi, S. Canals, and R. G. Morris. Silent learning. *Current Biology*, 28:3508–3515, 2018.
- J. Ryu, L. Liu, T. P. Wong, D. C. Wu, A. Burette, R. Weinberg, Y. T. Wang, and M. Sheng. A critical role for myosin IIb in dendritic spine morphology and synaptic function. *Neuron*, 49(2):175–182, 2006.
- B. L. Sabatini, T. G. Oertner, and K. Svoboda. The life cycle of Ca^{2+} ions in dendritic spines. *Neuron*, 33(3):439–452, 2002.
- P. Schätzle, M. Esteves da Silva, R. P. Tas, E. A. Katrukha, H. Y. Hu, C. J. Wierenga, L. C. Kapitein, and C. C. Hoogenraad. Activity-dependent actin remodeling at the base of dendritic spines promotes microtubule entry. *Current Biology*, 28(13):2081–2093.e6, 2018.
- J. Schindelin, I. Arganda-Carreras, E. Frise, V. Kaynig, M. Longair, T. Pietzsch, S. Preibisch, C. Rueden, S. Saalfeld, B. Schmid, J.-Y. Tinevez, D. J. White, V. Hartenstein, K. Eliceiri, P. Tomancak, and A. Cordona. Fiji: An open-source platform for biological-image analysis. *Nature Methods*, 9(7):676–682, 2012.
- H. W. Schroeder III, C. Mitchell, H. Shuman, E. L. F. Holzbaur, and Y. E. Goldman. Motor number controls cargo switching at actin-microtubule intersections *in vitro*. *Current Biology*, 20(8):687–696, 2010.
- E. Schulze, D. J. Asai, J. C. Bulinski, and M. Kirschner. Posttranslational modification and microtubule stability. *Journal of Cell Biology*, 105(5):2167–2177, 1987.

- G. Seano and L. Primo. Podosomes and invadopodia: tools to breach vascular basement membrane. *Cell Cycle*, 14(9):1370–1374, 2015.
- B. W. Shen, R. Josephs, and T. L. Steck. Ultrastructure of the intact skeleton of the human erythrocyte membrane. *Journal of Cell Biology*, 102(3):997–1006, 1986.
- M. Shen, N. Zhang, S. Zheng, W. B. Zhang, H. M. Zhang, Z. Lu, Q. P. Su, Y. Sun, K. Ye, and X. D. Li. Calmodulin in complex with the first IQ motif of myosin-5a functions as an intact calcium sensor. *Proceedings of the National Academy of Sciences of the United States of America*, 113(40):E5812–E5820, 2016.
- S. C. Sidenstein, E. D’Este, M. J. Böhm, J. G. Danzl, V. N. Belov, and S. W. Hell. Multicolour multilevel STED nanoscopy of actin/spectrin organization at synapses. *Scientific Reports*, 6, 2016.
- M. Sirajuddin, L. M. Rice, and R. D. Vale. Regulation of microtubule motors by tubulin isoforms and post-translational modifications. *Nature Cell Biology*, 16(4):335–344, 2014.
- A. S. Smith, R. B. Nowak, S. Zhou, M. Giannetto, D. S. Gokhin, J. Papoin, I. C. Ghiran, L. Blanc, J. Wan, and V. M. Fowler. Myosin IIa interacts with the spectrin-actin membrane skeleton to control red blood cell membrane curvature and deformability. *Proceedings of the National Academy of Sciences of the United States of America*, 115(19):E4377–E4385, 2018.
- A.-h. Song, D. Wang, G. Chen, Y. Li, J. Luo, S. Duan, and M.-m. Poo. A selective filter for cytoplasmic transport at the axon initial segment. *Cell*, 136(6):1148–1160, 2009.
- E. N. Star, D. J. Kwiatkowski, and V. N. Murthy. Rapid turnover of actin in dendritic spines and its regulation by activity. *Nature Neuroscience*, 5(3):239–246, 2002.
- T. Takeuchi, A. J. Duzskiewicz, and R. G. Morris. The synaptic plasticity and memory hypothesis: encoding, storage and persistence. *Philosophical Transactions of the Royal Society B: Biological Sciences*, 369(1633), 2014.
- R. P. Tas, A. Chazeau, B. M. Cloin, M. L. Lambers, C. C. Hoogenraad, and L. C. Kapitein. Differentiation between oppositely oriented microtubules controls polarized neuronal transport. *Neuron*, 96(6):1264–1271.e5, 2017.
- V. Tatavarty, S. Das, and J. Yu. Polarization of actin cytoskeleton is reduced in dendritic protrusions during early spine development in hippocampal neuron. *Molecular Biology of the Cell*, 23(16):3167–3177, 2012.
- P. W. Tillberg, F. Chen, K. D. Piatkevich, Y. Zhao, C. C. Yu, B. P. English, L. Gao, A. Martorell, H. J. Suk, F. Yoshida, E. M. Degennaro, D. H. Roossien, G. Gong, U. Seneviratne, S. R. Tannenbaum, R. Desimone, D. Cai, and E. S. Boyden. Protein-retention expansion microscopy of cells and tissues labeled using standard fluorescent proteins and antibodies. *Nature Biotechnology*, 34(9):987–992, 2016.
- S. Tonegawa, X. Liu, S. Ramirez, and R. Redondo. Memory engram cells have come of age. *Neuron*, 87(5):918–931, 2015.
- J. Tønnesen, G. Katona, B. Rózsa, and U. V. Nägerl. Spine neck plasticity regulates compartmentalization of synapses. *Nature Neuroscience*, 17(5):678–685, 2014.

- S. Truckenbrodt, M. Maidorn, D. Crzan, H. Wildhagen, S. Kabatas, and S. O. Rizzoli. X10 expansion microscopy enables 25-nm resolution on conventional microscopes. *EMBO reports*, 19(9):1–12, 2018.
- S. Truckenbrodt, C. Sommer, S. O. Rizzoli, and J. G. Danzl. A practical guide to optimization in X10 expansion microscopy. *Nature Protocols*, 14(3):832–863, 2019.
- K. M. Trybus, E. Kremontsova, and Y. Freyzon. Kinetic characterization of a monomeric unconventional myosin V construct. *Journal of Biological Chemistry*, 274(39):27448–27456, 1999.
- B. van Bommel and M. Mikhaylova. Talking to the neighbours: The molecular and physiological mechanisms of clustered synaptic plasticity. *Neuroscience & biobehavioral reviews*, 71:352–361, 2016.
- B. van Bommel, A. Konietzny, O. Kobler, J. Bär, and M. Mikhaylova. F-actin patches associated with glutamatergic synapses control positioning of dendritic lysosomes. *The EMBO Journal*, 38(15):1–17, 2019.
- K. J. Verhey and J. W. Hammond. Traffic control: Regulation of kinesin motors. *Nature Reviews Molecular Cell Biology*, 10(11):765–777, 2009.
- W. Wagner, K. Lippmann, F. F. Heisler, K. V. Gromova, F. L. Lombino, M. K. Roesler, Y. Pechmann, S. Hornig, M. Schweizer, S. Polo, J. R. Schwarz, J. Eilers, and M. Kneussel. Myosin VI drives clathrin-mediated AMPA receptor endocytosis to facilitate cerebellar long-term depression. *Cell Reports*, 28(1):11–20.e9, 2019.
- G. Wang, J. R. Moffitt, and X. Zhuang. Multiplexed imaging of high-density libraries of RNAs with MERFISH and expansion microscopy. *Scientific Reports*, 8, 2018.
- Z. Wang, J. G. Edwards, N. Riley, D. W. Provance, R. Karcher, X. dong Li, I. G. Davison, M. Ikebe, J. A. Mercer, J. A. Kauer, and M. D. Ehlers. Myosin Vb mobilizes recycling endosomes and AMPA receptors for postsynaptic plasticity. *Cell*, 135(3):535–548, 2008.
- K. Watanabe, S. Al-Bassam, Y. Miyazaki, T. J. Wandless, P. Webster, and D. B. Arnold. Networks of polarized actin filaments in the axon initial segment provide a mechanism for sorting axonal and dendritic proteins. *Cell Reports*, 2(6):1546–1553, 2012.
- G. Wen, M. Vanheusden, A. Acke, D. Vali, S. Finn Mayer, R. K. Neely, V. Leen, and J. Hofkens. Evaluation of direct grafting strategies in expansion microscopy. *BioRxiv*, pages 1–12, 2019.
- J. S. Wiegert, M. Pulin, C. E. Gee, and T. G. Oertner. The fate of hippocampal synapses depends on the sequence of plasticity-inducing events. *eLife*, 7:1–18, 2018.
- S. J. Wiegert, C. E. Gee, and T. G. Oertner. Single-cell electroporation of neurons. *Cold Spring Harbor Protocols*, 1:135 – 138, 2017.
- E. Wulf, A. Deboben, F. A. Bautz, H. Faulstich, and T. Wieland. Fluorescent phalloxin, a tool for the visualization of cellular actin. *Proceedings of the National Academy of Sciences of the United States of America*, 76(9):4498–4502, 1979.
- K. Xu, G. Zhong, and X. Zhuang. Actin, spectrin, and associated proteins form a periodic cytoskeletal structure in axons. *Science*, 339(6118):452–456, 2013.

- G. Yang, F. Pan, and W.-B. Gan. Stably maintained dendritic spines are associated with lifelong memories. *Nature*, 462:920–924, 2009.
- Y. Yang and N. Calakos. Presynaptic long-term plasticity. *Frontiers in Synaptic Neuroscience*, 5:1 – 22, 2013.
- K. W. Yau, P. Schatzle, E. Tortosa, S. Pages, A. Holtmaat, L. C. Kapitein, and C. C. Hoogenraad. Dendrites *in vitro* and *in vivo* contain microtubules of opposite polarity and axon formation correlates with uniform plus-end-out microtubule orientation. *Journal of Neuroscience*, 36(4):1071–1085, 2016.
- I. Yu, C. P. Garnham, and A. Roll-Mecak. Writing and reading the tubulin code. *Journal of Biological Chemistry*, 290(28):17163–17172, 2015.
- G. Zhong, J. He, R. Zhou, D. Lorenzo, H. P. Babcock, V. Bennett, and X. Zhuang. Developmental mechanism of the periodic membrane skeleton in axons. *eLife*, 3:1–21, 2014.
- R. Zhou, B. Han, C. Xia, and X. Zhuang. Membrane-associated periodic skeleton is a signaling platform for RTK transactivation in neurons. *Science*, 365(6456):929–934, 2019.

Appendix

A Additional materials, methods, and protocols

A.1 Plasmid DNA preparation

Protocol to extract plasmids from bacteria in small volume amount (mini-prep). Prepare buffers P1, P2, and P3 according to Table A.1.

Table A.1: Buffers for DNA mini prep

Buffer	Composition	Comments
P1	50 mM Tris-HCl, 10 mM EDTA, 100 µg/ml RNase A, pH 8.0	Store at 4 °C
P2	200 mM NaOH, 1 % SDS	
P3	3 M potassium acetate, pH 5.5	Pre-chill on ice

1. Inoculate 5 ml cultures (lysogeny broth (LB) medium + 100 µg/ml ampicillin or 30 µg/ml kanamycin) and grow for 12 h.
2. Pellet down 2 ml of each culture in an 2 ml Eppendorf tube (5 min, 3000 x g).
3. Discard the supernatant, and resuspend in 300 µl P1 buffer.
4. Add 300 µl P2 buffer, turn tubes upside down for 4 times.
5. Incubate for 1- 5 min at RT.
6. Add 300 µl of cold P3 buffer, turn tube upside down for 4 times.
7. Incubate for 5 min on ice.
8. Centrifuge for 10 min at 4 °C (20000 x g / max speed).
9. Transfer supernatant into a new Eppendorf tube.
10. Add 500 µl of isopropanol, mix thoroughly.
11. Incubate for 10 min at RT.
12. Centrifuge for 10 min at 4 °C (20000 x g / max speed).
13. Discard supernatant, and add 1 ml of 70 % ethanol.
14. Centrifuge for 10 min (20000 x g / max speed).

15. Discard supernatant and airdry the pellet.
16. Resuspend the pellet in 30 μl H_2O .
17. Measure the DNA concentration by (nano-) spectrophotometry.

A.2 Molecular cloning procedures

Cloning and generation of new plasmids can be performed in many different ways. Here I describe the most general procedures of cloning steps used in the work of this thesis.

A.2.1 Plan the cloning

Which insert needs to be placed in what target vector? Design primers to perform a PCR to extract the insert from a template DNA (another vector/ DNA library, synthesized DNA fragment or other). Define unique restriction sites to open and linearize the target vector at the desired place. Make sure that the final product has the correct reading frame for the translation of all components.

A.2.2 Run a PCR to amplify the insert

Run a PCR to amplify the insert from the template. Use a DNA polymerase with proofreading ability to minimize mutations. The primer annealing temperature depends on the primer sequences. The extension time depends on the length of the insert and speed of the used polymerase.

Table A.2: Standard PCR pipetting scheme

Component	Volume
H_2O	19 μl
10x buffer	3 μl
dNTPs (10 mM each)	2 μl
5' - primer (10 μM)	2 μl
3' - primer (10 μM)	2 μl
DNA polymerase	1 μl
Template DNA (50-1000 ng)	1 μl
Total volume: 30 μl	

Table A.3: Standard PCR Protocol

Temperature, °C	Time	PCR step
98	1.5 min	Initial denaturation
30-35 cycles		
98	20 s	Denaturation
50-72 (variable)	30 s	Annealing
72	variable	Extension
72	7 min	Final extension
4	∞	

A.2.3 Purify the PCR fragment using agarose gel electrophoresis

To purify the insert, the PCR product is loaded next to a marker (a mixture DNA fragments with a defined size) on a agarose gel (0.5-2 %, 1 % standard). By applying electrical current to the gel, the negatively charged DNA fragment migrates through the gel based on its length and folding (smaller fragments migrate faster). Hereby fragments of different sizes are segregated. The position of DNA can be visualized with Rotisafe, ethidiumbromide or other methods. If the PCR was successful, there should be an band corresponding to the correct size. The band can be cut out of the gel and the DNA can be extracted using a purification kit (e.g. Roboklon, Argaroseout Gel-extraction DNA kit #E3540-02, used in this work).

A.2.4 Digest the target vector and insert

Standard cloning is performed with the use of restriction sites. When possible one should use unique sticky-end (vs. blunt-end) restriction sites for the vector and insert. This reduces the chances of ligation of the vector without insertion of the insert. It also ensures that the insert can be, in a later step, only inserted in one orientation (5' → 3'). The time of digestion depends on the used amount of DNA and enzymes (units). Some enzymes can be used simultaneously in the same buffer, others have to be used sequentially in different buffers. For optimum results, use the recommended protocols from the supplier.

To prevent unwanted back-ligation of the digested vector, especially in blunt-end cloning, one should introduce a dephosphorylation step of the vector. This procedure removes the 5' phosphate group, which makes it extremely unlikely for the vector to ligate. If this step is applied, one should make sure that the 5' end of the insert contains a phosphate.

A.2.5 Purify the digested fragment and vector using agarose gel electrophoresis

This step is similar to step A.2.3. By use of the agarose gel electrophoresis the digested insert and vector are cleaned up from other undesired DNA fragments. The DNA is extracted from the agarose gel using a purification kit.

A.2.6 Ligation of the insert and target vector

Ligate the insert into the target vector using a DNA ligase (e.g. T4 DNA-ligase, Thermo Fisher Scientific #EL0011, used in this work). Use according to the manufacturer's protocol. Incubate 15 min at RT or ON at 4 °C.

Optional: Include the digested target vector without insert as negative control.

A.2.7 Transform the ligated products

Transform the ligated products (and optional negative control) into chemically competent bacteria. Use a bacterial strain optimized for plasmid production (e.g. self prepared XL10-Gold, see A.3, used here).

1. Incubate DNA with bacteria for 10 min on ice.
2. Heat-shock for 45 s at 42 °C in water bath or thermo shaker.
3. Incubate for 2 min on ice.
4. Incubate for 45 min - 1 h in super optimal broth with catabolite repression (SOC) medium (super optimal broth (SOB) medium + 20 mM glucose).
5. Plate on LB agar plates with correct antibiotics (100 µg/ml ampicillin, 30 µg/ml kanamycin, or 25 µg/ml chloramphenicol).

A.2.8 Perform minipreps to test which of the obtained colonies are correct

Perform mini preps (see A.1) from the obtained colonies. To check if the desired insert is present, one can use the DNA to perform a PCR or digestion. Run an agarose gel electrophoresis to check if the insert (with correct size) is present. The obtained DNA of the clones can be sequenced to exclude clones with point mutations and/or frame shifts. Bacteria from correct clones can be grown in larger volumes for midi/maxi plasmid purifications (e.g. Quiagen, Plasmid midi kit #12143, used in this work).

A.2.9 Optional procedures

1. Insert DNA fragments can be extended by running a second PCR. A new forward or reverse primer is used to extend the original insert (template). This extension can be used to include e.g. additional restriction sites or small tags.
2. Small DNA fragments/ inserts (1 < kb) can be ligated by PCR. To do this, the fragments need a ± 15 base pair overlapping end. Both fragments are included in a PCR reaction as template. The PCR mix should also include 1 forward and 1 reverse primer fitting for the final, larger product.

3. Instead of restriction digestion cloning, one can perform cloning by homologous recombination. Homologous recombination does not require restriction sites for ligation, instead it needs ± 15 base pair overlap on each side. (Of note: The target vector still needs to be linearized by digestion.) This can be an advantage if the number of (unique) restriction sites is limited. Cloning by homologous recombination can also be faster, as it includes less steps. Kits for cloning with homologous recombination are supplied by different manufacturers. One example used in this work is the cold fusion cloning kit supplied by system biosciences (system biosciences #MC100B-1).

A.3 Preparation of chemical competent bacteria

This protocol is based on Green and Rogers [2013].

1. Prepare buffers I and II according to Tables A.4 and A.5.

Table A.4: Transformation buffer I (120 ml)

Component	Final concentration	Amount
RbCl	100 mM	1.45 g
MnCl ₂	50 mM	0.86 g
Potassium acetate	30 mM	0.35 g
CaCl ₂ * 2 H ₂ O	10 mM	0.18 g
Glycerol	15 % (v/v)	18 ml

Add manganese chloride last, try to minimize red/ orange precipitation.
Adjust pH to 5.8 with citric acid and filter through a 0.45 μ m filter.

Table A.5: Transformation buffer II (100 ml)

Component	Final concentration	Amount
MOPS ¹	10 mM	0.21 g
RbCl	10 mM	0.12 g
CaCl ₂	75 mM	1.10 g
Glycerol	15 % (v/v)	15 ml

Adjust pH to 6.8 with KOH and filter through a 0.2 μ m filter.

2. Pre-cool tubes and racks in -20 °C freezer.
3. Grow *E. coli* XL10-Gold on an agar plate with chloramphenicol.

¹3-(N-morpholino)propanesulfonic acid

4. Pick a colony and start a 50 ml pre-culture with chloramphenicol ON.
5. Add 10 ml of pre-culture to 190 ml LB medium and grow to OD₆₀₀ 0.4-0.5.
6. Incubate for 15 min on ice.
7. Centrifuge at 3500 x g for 15 min at 4 °C.
8. Re-suspend pellet in 60 ml ice-cold transformation buffer I.
9. Incubate for 10 min on ice.
10. Centrifuge at 3500 x g for 15 min at 4 °C.
11. Re-suspend pellet in 8 ml ice-cold transformation buffer II.
12. Aliquot in 50 µl and directly freeze in liquid nitrogen.
13. Store at -80 °C.

A.4 Culturing procedures for standardized cell lines

A.4.1 Splitting of COS-7/ HEK/ MRC-5 cells

Cell lines are cultured in 10 cm ø petri dishes. Full medium for culturing of cell lines is prepared according to Table A.6 and can be stored after heat inactivation (30 min, 56 °C) in aliquots at -20 °C. Note that DMEM contains glucose.

Table A.6: Full medium

Volume	Component	Supplier	Product number
450 ml	DMEM	Gibco / Thermo Fisher Scientific	41966-029
50 ml	Fetal calf serum	Gibco / Thermo Fisher Scientific	10270
5 ml	Penicillin/ strepto- mycin	Gibco / Thermo Fisher Scientific	15140-122

1. Prewarm HBSS, full medium, and trypsin/ EDTA (Thermo Fisher Scientific #25200-056) in water bath.
2. Remove medium from the cells.
3. Carefully add 10 ml warm HBSS to the wall of the dish for washing.
4. Remove HBSS.

5. Trypsinize celly by adding 2 ml trypsin/ EDTA and incubate 5-7 min at 37 °C in the incubator.
6. Check if cells detached. If not, carefully tap on dish, shake a bit, or incubate a bit longer (not longer than 10 min in total).
7. Add 8 ml warm full medium.
8. If cells are still attached: detach by pipetting up and down.
9. Take a new dish, add 9 ml fresh full medium and add 1 ml of cell suspension (for 1:10 split).
10. Mix gently.
11. Place back in incubator.

Split two or three times per week.

A.4.2 Freezing of COS-7/ HEK/ MRC-5 cells

1. Prepare freeze-down medium (full medium with 20 % FCS + 10 % DMSO (Roth #A994.1)).
2. Trypsinize confluent plate(s) with cells.
3. Add 10 ml full medium.
4. Spin down cells at 100 x g for 5 min 4 °C.
5. Remove supernatant, add 2 ml freeze-down medium.
6. Aliquote the cell suspension in cryo tubes.
7. Place vials into a cryo-cooler in the -80 °C freezer for 24 h. Note: The cryo-cooler should be at RT and filled with the correct amount of isopropanol.
8. Transfer containers to a liquid nitrogen tank.

A.4.3 Thawing of COS-7/ HEK/ MRC-5 cells

1. Preheat full medium.
2. Quickly (< 1 min) thaw one cryo tube with cells by gently swirling the vial in a 37 °C water bath.
3. Add 10 ml full-medium.
4. Spin-down cells at 100 x g for 5 min 4 °C.
5. Remove supernatant.

6. Resuspend pellet carefully in 1 ml full medium.
7. Plate on 10 cm \varnothing dish with 9 ml full-medium.
8. Place in incubator.

A.4.4 Transfection of COS-7/ HEK/ MRC-5 cells

1. Preheat full medium.
2. Prepare one eppendorf tube with transfection mix per well.
 - a) 2 μ g (6 well plate) or 1 μ g (12 well plate) of (total) DNA per tube.
 - b) Add 200 μ l (6 well plate) or 100 μ l (12 well plate) DMEM.
 - c) Add 6 μ l (6 well plate) or 3 μ l (12 well plate) Fugene 6 (Promega # E2691)/ or Max-PEI (Polysciences #24765-1).
 - d) Mix and incubate 20-30 min at RT (longer incubation increases transfection rate).
3. Take the plates for transfection, remove medium and add 2 ml (6 well plate) or 1 ml (12 well plate) of warm full medium.
4. Add transfection mix to cells.
5. Culture at 37 °C, 5 % CO₂ ON.

Always keep the ratio of DNA:Fugene/ MaxPEI constant.

A.5 Poly-L-lysine coating of coverslips for adherent cell culture

Protocol for poly-L-lysine (PLL) coating of coverslips for adherent cell culture (e.g. HEK 293T cells and primary hippocampal neurons).

1. Prepare 10 mg/ml PLL (Sigma-Aldrich #P2636-25mg) stock solution in sterile H₂O. Store PLL stock in 150 μ l aliquots at -80 °C.
2. Prepare 0.15 M borate (Roth #6943.2) solution in H₂O. Sterile filter. Store borate solution at 4 °C.
3. Freshly prepare coating solution by dissolving 1 aliquot of PLL stock in 15 ml of borate solution.
4. Coating of coverslips:
 - a) Add 150 μ l per well of a 6-well plate (80 μ l for 12-well plate) and put glass coverslips on top. Incubate for 4 h at RT.
 - b) Flip the coverslips and wash 5x with sterile water.

- c) Replace water by HBSS and store at 37 °C, 5 % CO₂. HBSS will turn orange/ light brown.

5. Seeding of cells:

- Remove HBSS and seed cells in full medium (see Table A.6) at the desired concentration.

A.6 Preparation of primary rat hippocampal cell cultures

The preparation of rat primary hippocampal cultures requires the use of animals. All procedures must be performed with, and in agreement with a license provided by the local and/ or state authorities. The license can be obtained after ethical assessment of the project. The assessment involves judging of the experimental procedures, harm to the animal, training of the experimentalist and the knowledge the experiment could provide. The preparation of primary hippocampal cultures is categorized as sacrificing for tissue and not an animal experiment. The respective license should be obtained before the start of the experiment.

Primary rat hippocampal cultures are prepared from E18 embryos.

A.6.1 Required materials

- 20 % O₂ / 80 % CO₂ gas mixture, regulator, and tubing
- Guillotine for rats
- 24-well, 12-well or 6-well plates with coated coverslips (see A.5)
- HBSS –/– (Sigma-Aldrich #H9269)
- 0.25 % trypsin/ EDTA (Thermo Fisher Scientific #25200-056)
- Dissection tools
 - 1x large scissors
 - 2x large forceps
 - 1x medium sized scissors
 - 1x Fine scissors
 - 1x Course forceps
 - 1x Small spatula or spoon
 - 2x fine forceps
- Minimal two glass petridishes
- Dissection stereomicroscope with cold base
- Syringe 2 ml

- Syringe needle 20 G (0.90 x 40 mm, Braun)
- Syringe needle 26 G (0.45 x 25 mm, Braun)
- 1 EASYstrainer (Greiner #542000)
- Neubauer chamber
- Trypan blue
- Light microscope (for counting)
- Full medium (see Table A.6)
- Culturing medium (BrainPhys + 1x SM1 (StemCell #05792) + 0.5 mM glutamine)
- 1 ice bucket
- Hot bead sterilizer
- Water bath (37 °C)
- Vacuum pump with a sterile glass Pasteur pipette as nozzle
- Incubator (37 °C / 5 % CO₂)

A.6.2 Preparations

1. Sterilize all tools and petri dishes by autoclaving.
2. Preheat culturing medium.
3. Prepare outside of the hood:
 - Guillotine
 - Dissection stereomicroscope with cold base
 - Neubauer counting chamber
 - Light microscope
 - Dissection tools for dissecting the embryos and collecting the heads:
 - 1x large sciccors
 - 2x large forceps
 - 1x medium sized scissors
 - Dissection tools for dissecting the hippocampi:
 - 1x fine scissors
 - 1x small spatula or spoon
 - 2x fine forceps

- Dissection stereomicroscope with cold base
 - Neubauer counting chamber
 - Light microscope
 - 1x 15 falcon on ice with 10 ml HBSS –/–
 - 1x 50 ml HBSS –/– in the water bath
 - 2x 50 ml of full medium in the water bath
4. Prepare inside of the hood:
- 1x 50 ml HBSS –/– on ice
 - Syringe 2 ml
 - Syringe needle 20 G
 - Syringe needle 26 G
 - 1 Eppendorf tube with 15 μ l trypan blue

A.6.3 Procedure

1. Anesthetize a pregnant rat with 20 % O₂ / 80 % CO₂ and sacrifice it using the guillotine.
2. Dissect out the E18 embryos using the large scissors and large forceps. Directly decapitate the embryos and collect the heads in a petridisch with cold HBSS –/–. Note: Be careful with the dissection. During dissection the embryos should be kept sterile.
3. Dissect the embryonic brains out of the skull using fine scissors, coarse forceps and a small spatula/spoon. First, cut the skin and skull starting from the neck in direction to the nose. Remove the skin and skull towards the side of head with the large forceps. Use the spatula/spoon to flip the brain out.
4. Flip the brain into a petri dish filled with cold HBSS –/–. Place the petridish with the brain under the dissection microscope. Hold the cerebellum with one fine forceps to keep the brain in place. With the second forceps, separate the two hemispheres up to the cerebellum. Flip one of the hemisphere outwards on the sagittal axis. This should expose the hippocampus. Remove when needed any meninges. Use the second forceps to make a small cut at the frontal and caudal end of the hippocampus. Carefully try to remove the hippocampus. Repeat the procedure for the other hemisphere. Collect the hippocampi in a 15 ml falcon tube with 10 ml HBSS –/–. Place the falcon tube on ice and repeat the dissection of hippocampi for all pups.
5. Take the falcon tube with hippocampi inside of the cell culture hood and wash the hippocampi 5 times with 10 ml cold HBSS –/– .
6. Remove all but 2 ml HBSS –/– and add 100 μ l trypsin per hippocampus. Incubate for 15 min at 37 °C (water bath).

7. In the cell culture hood, wash the trypsinized hippocampi 5 times with warm HBSS –/– (9 ml each).
8. Aspirate the HBSS –/– to a final volume of 2 ml. Mechanically triturate the hippocampi using the two different needles. Start with larger diameter needle. Carefully pipette the hippocampi up and down until all big pieces of tissue have disappeared and the solution turns cloudy. Subsequently filter the cells using the EASYstrainer, flush with 2-3 ml warm HBSS –/–.
9. Pipette 15 µl of the cell solution to the earlier prepared 15 µl trypan blue. Mix slowly by pipetting a few times. Pipette 10 µl to the Neubauer counting chamber. Count the number of living cells using the light microscope. Number of cells per ml = [average of the four large quadrants * 10000] * 2.
10. Dilute the cells to the desired plating concentration in full medium (40000 (low density) or 60000 (high density) cells /ml).
11. Take the earlier prepared plates with the coated coverslips. Remove the HBSS –/– from the plates with the vacuum pump and plate the cells (2 ml, 1 ml or 0.5 ml per well in a 6-, 12,- or 24- well plate). Place the plates in the incubator (37 °C / 5 % CO₂).
Note: For biochemistry applications one can also grow the neurons on a plastic surface. This does not require coating with poly-L-lysine.
12. After approximately one hour, when the cells have adhered, exchange the full medium with growth medium. Culture in the incubator (37 °C / 5 % CO₂).

A.6.4 Culturing

For optimal growth partially exchange the medium every week: Remove a proportion of the old growth medium (200 µl, 100 µl, or 50 µl for 6-well, 12-well, or 24-well plate). Add double volume new growth medium.

A.7 Preparation of organotypic hippocampal slice cultures

The preparation of rat organotypic hippocampal slice cultures requires the use of animals. All procedures must be performed with, and in agreement with a license provided by the local and/ or state authorities. The license can be obtained after ethical assessment of the project. The assessment involves judging of the experimental procedures, harm to the animal, training of the experimentalist and the knowledge the experiment could provide. The preparation of primary hippocampal slice cultures is categorized as sacrificing for tissue and is not an animal experiment. The respective license should be obtained before the start of the experiment. This protocol is based on: 'Preparation of Slice Cultures from Rodent Hippocampus' by Gee et al. [2017].

A.7.1 Required materials

- 20 % O₂ / 80 % CO₂ gas mixture, regulator, and tubing
- 500 ml glass beaker
- 1000 µl cell saver tips (BIOzym #6933000)
- 1x 1000 µl- pipette
- 6-well cell culture plates
- Dissection stereomicroscope
- Whatman filter paper (6 cm ø, Macherey-Nagel #431005)
- Fine paintbrush
- Hot bead sterilizer
- Incubator (37 °C / 5% CO₂)
- 1 large ice container
- 1 small ice container
- Millicell Cell Culture Inserts (30 mm, Hydrophilic PTFE [polytetrafluoroethylene], 0.4 µm, Millipore #PICMORG50)
- Paper towels (autoclaved)
- Glass Pasteur pipettes (autoclaved, Carl Roth #4518.1)
- Glass Pasteur pipettes with tips broken off (autoclaved, Carl Roth #4518.1)
- 2 pipette bulbs (2 ml, Sigma-Aldrich #Z111597)
- Plastic disposable pasteur pipettes (Sarstedt #86.1171.010)
- Spray bottle filled with 70 % ethanol
- Stainless steel tray
- Dissection tools:
 - 1x large scissors
 - 2x scalpel knives
 - 1x fine scissors
 - 1x large forceps
 - 1x small spatula or spoon

- 2x fine forceps
- 1x dissection tool
- Tissue chopper with razor blade (McIlwain type, Ted Pella #10180)
- Glass petri dishes
- Tissue culture hood
- 50 ml, 15 ml falcon tubes

A.7.2 Required buffers

Dissection medium and slice culture medium are prepared according to Tables A.7 and A.8.

Table A.7: Dissection medium (low sodium ACSF, 500 ml)

Component	Final Concentration	Amount
1M CaCl ₂	1 mM	0.5 ml
1M MgCl ₂	5 mM	2.5 ml
Glucose	10 mM	0.9 g
KCl	4 mM	0.15 g
NaHCO ₃	26 mM	1.09 g
Sucrose	248 mM	40 g
0.5 % phenol red	0.001 %	1 ml

Filter sterilize through a 0.2 µm filter, aliquote in 50 ml, store at 4 °C.
Before use, add kynurenic acid to a final concentration of 2 mM.

Table A.8: Slice culturing medium (500 ml)

Component	Final Concentration	Amount
MEM		394 ml
Horse serum	20 %	100 ml
200 mM L-glutamine	1 mM	2.5 ml
25 % ascorbic acid	0.00125 %	2.4 µl
1 mg/ml insulin	0.01 mg/ml	0.5 ml
1 M CaCl ₂	1 mM	0.5 ml
1 M MgSO ₄	2 mM	1 ml
D-glucose	13 mM	1.16 g

20 mM HEPES (final concentration) needs to be added if MEM without is used.

Horse serum has to be heat inactivated at 56 °C for 30 min.

Filter sterilize through a 0.2 µm filter, aliquot in 50 ml and store at 4 °C.

The pH value should be 7.28, osmolarity 320 mOsm.

A.7.3 Procedure

1. Sterilize the dissection tools by autoclaving. Place a filter paper in the glass petri dishes (1 petri dish/ animal) and autoclave.
2. Prepare the 6-well plates for culturing: Add 1 ml of culturing medium to each well. Place a Millipore membrane in each well, use autoclaved forceps. Place the prepared well plate(s) in the incubator at 37 °C, 5 % CO₂.
3. Prepare outside of the cell culture hood:
 - An ice bucket covered with a stainless steel tray. Place the glass petri dishes with filter paper on top to cool.
 - Prepare a small stainless steel tray with sterile paper for dissection.
 - A container for the body
 - Sort the following tools on a sterile paper:
 - 1x large scissors
 - 1x scalpel knife
 - 1x fine scissors
 - 1x large forceps
 - 1x small spatula or spoon
 - A bucket with water
 - A heated bead sterilizer
4. Prepare inside of the cell culture hood:
 - The dissection stereomicroscope including a cold base (can be a liquid cooling element or steel base).
 - An ice bucket with a 50 ml falcon tube with dissection medium (continuously bubbled with 95 % O₂/ 5 % CO₂ - use a sterile glass Pasteur pipette). In addition, add one disposable Pasteur pipette.
 - A sterile paper towel with the following dissection tools:
 - 2x fine forceps
 - 1x scalpel knife
 - 1x dissection tool
 - A ready to use tissue chopper fitted with a blade. All parts, later in contact with the tissue, should be disinfected with 70 % ethanol.
 - A rack with three 15 ml falcon tubes containing:
 - 1x glass Pasteur pipette with pipette bulb
 - 1x inverted glass Pasteur pipette (with broken tip) with pipette bulb

– 1000 µl pipette fitted with a cell saver tip

5. To start, add dissection medium to one of the petri dishes with filter paper. The filter paper should be fully wet.
6. Decapitate an animal on the stainless steel tray using the large scissors. Discard the body in the container. Take the scalpel knife and cut the skin from the nose towards the neck region and remove to the sides. Next, take the fine scissors and cut the skull from the neck towards the nose (stop at the front of the brain). Remove the skull with the large forceps towards the sides of the head. Use the spacula/ small spoon to take out the brain. Work from the front of the brain. Place the brain in the petri dish on the filter paper soaked with dissection medium, and taken it into the cell culture hood. The lid of the petri dish is placed upside down and used later. Directly add some dissection medium on top of the brain. Work carefully to prevent the skin from touching the brain or any of the clean tools. The skin is not sterile. Decontaminate the gloves with 70 % ethanol before continuing with the next steps.

Note: After using the tools place them in the beaker with water, with exception of the scalpel knife. When finished with point 11, take out the tools and dry them with a paper tissue. Put them shortly in the hot bead sterilizer before placing them clean back on the autoclaved tissue. Clean the scalpel knife with 70 % ethanol.

7. Dissect the hippocampi out of the brain. Hold the cerebellum with one fine forceps to keep the brain in place. Use the scalpel knife to cut in between the two hemispheres. Flip one hemisphere outwards over the transverse axis. This will expose the hippocampus. Loosen the hippocampus in the frontal and distal part of the brain by a small cut with a dissection tool. Next, roll the hippocampus outwards over the cortex. When the hippocampus is isolated from the rest of the brain, keep it submerged in dissection medium. Repeat the procedure for the other hemisphere.
8. Use the inverted glass Pasteur pipette with bulb to transfer the hippocampi onto the base of the tissue chopper. Make sure that the hippocampi are placed in the transverse orientation relative to the blade. Remove all medium with the glass Pasteur pipette and chop the hippocampus into 400 µm thick sections.
9. Take the lid of the glass petri dish and place it under the dissection microscope. Take the base of the tissue chopper with the chopped hippocampi and transfer the hippocampi into the lid of the petri dish. Do this by using dissection medium and the glass Pasteur pipette.
10. Separate the hippocampal slices further with two fine forceps in the hood. Try to touch the hippocampal slices as less as possible to not damage them. Sometimes it can help to carefully pipette them up and down with a 1000 µl pipette equipped with a cell saver tip.
11. Take the 6-well plate with membranes out of the incubator. Take the 1000 µl pipette with a cell saver tip to transfer hippocampal slices onto the membranes. Select 'good' slices, which contain all structures of the hippocampus and are not damaged. Place two to four slices per membrane (depending on the application). Use the fine paintbrush to orientate

the slices in the desired direction. Afterwards, remove all dissection medium with the glass Pasteur pipette. Place the 6-well plate back in the incubator.

12. Proceed with the next pup starting from point 5.
13. Afterwards, clean all tools and prepare them for autoclaving. Clean all surfaces and the cell culturing hood with 70 % ethanol. Clean the base of the tissue chopper and small paintbrush with 70 % ethanol.

A.7.4 Culturing of the organotypic slices

The organotypic slices require a medium change two to three times a week.

1. Use a glass pasteur pipette and sterilize it by placing it shortly in a hot bead sterilizer.
2. Attach the sterilized pasteur pipette to a vacuum pump via tubing.
3. Suck away approximately 75 % of the old medium in each of the wells by placing the pasteur pipette on the side.
4. Pipette 750 μ l of new slice culturing medium (37 °C) to each well.

A.8 Immunocytochemistry

A.8.1 Preparation of Mowiol-based mounting medium

1. For approximately 96 ml of mounting medium mix the following:
 - 9.6 g Mowiol (Mowiol 4-88, Roth #0713.2)
 - 24 ml PCR grade water
 - 24 g glycerol (99.5 % purity, Roth #3789)
2. Stir for 2 h.
3. Add 48 ml 0.2 M Tris pH 8.5 (pureTris, VWR #97061-796), pH adjusted with HCl.
4. Heat to 50 °C for 2 h (in a water bath). Stir 2 min every 20 min with magnetic stirrer.
5. Centrifuge at 5000 x g for 15 min to remove undissolved Mowiol.
6. Optional: Add 2.4 g (25 mg/ml) DABCO (Sigma-Aldrich #D27802-25g).
7. Aliquot and store at -20 °C.

The refractive index of this mounting medium (incl. DABCO) is 1.46 after 3 days (van Bommel et al. [2019]).

A.8.2 Buffers for ICC

- 20x PBS stock (3 M NaCl, 161 mM Na₂HPO₄, 39 mM NaH₂PO₄)
- Permeabilization buffer (0.2 % Triton-X-100 in 1x PBS (pH 7.4))
- Blocking buffer (10 % horse serum, 0.1 % Triton-X-100 in 1x PBS (pH 7.4)). Aliquots in 15 ml falcon tubes can be stored at -20 °C.

A.8.3 ICC procedure

ICC of 19 mm \varnothing coverslips. Volumes have to be adjusted proportionally for smaller or bigger coverslips.

1. Fix cells with 500 μ l of 4 % PFA (or Roti-Histofix, Roth #A146.4)/ 4 % sucrose for 10 min at RT.
2. Wash 3 times with 500 μ l 1x PBS for 10 min each.
3. Permeabilize cells with 500 μ l of permeabilization buffer for 10 min at RT.
4. Wash 2 times with 500 μ l 1x PBS for 5 min each.
5. Block cells in blocking buffer for 45-60 min in blocking buffer at RT.
6. Incubate with primary antibody: Flip coverslips on parafilm on 50 μ l droplets. The cells should face the parafilm/antibody solution. Incubate at 4 °C ON.
7. Flip coverslips back and wash 3 times with 500 μ l 1x PBS at RT for 10 min each.
8. Incubate with secondary antibody: Flip coverslips on parafilm on 50 μ l droplets. The cells should face the parafilm/antibody solution. Incubate for 1 h at RT.
9. Flip coverslips back and wash 3 to 5 times with 500 μ l 1x PBS for 10 min each.
10. Optional: Incubate with phalloidin in 1x PBS (1:40) ON at 4 °C and wash 3 times with 500 μ l 1x PBS. Note: This incubation step can also be shortened to 1 h at RT or applied together with secondary antibodies.
11. Optional: Add 1 μ g/ml DAPI in the second last washing step (1:1000 dilution of 1 mg/ml stock).
12. Mount coverslips on microscopy slides (approximately 10 μ l Mowiol or Vectashield).

A.9 Expansion microscopy

A.9.1 Required buffers

Prepare gel solution and digestion buffer according to Tables A.9 and A.10. Stocks for digestion buffer can be stored in aliquots at -20 °C.

Table A.9: Gel solution

	Amount for stock solution each	Amount for working solution
Sodium acrylate	19 g	2.25 ml
Acrylamide	12.5 g	1 ml
N,N-Methylenebisacrylamide	1 g	0.75 ml
Sodium chloride	12.98 g	4.50 ml
10x PBS		1 ml
Total		9.5 ml

Table A.10: Digestion buffer

	Stock concentration	Amount for 50 ml	Final concentration
TRIS	1 M	2.5 ml	50 mM
EDTA	0.125 M	0.4 ml	1 mM
Triton X-100	20 %	1.25 ml	0.5 %
Guanidine Hydrochloride		3.82 g	0.8 M

A.9.2 Procedure

1. Start with a regular ICC (see A.8), steps 1-10. Note: For expansion microscopy use tri-linked phalloidin in step 10.
2. Apply the anchoring reagent:
 - a) Incubate with 25 mM MA-NHS (in PBS) for 1 h at RT. Use 1 ml per coverslip in a 12-well plate. A 1:40 stock solution (in PBS) can be prepared and stored in the freezer for several weeks.
 - b) Wash 3 times with PBS 1x for 10 min each.
3. Gelation:
 - a) Add 1 ml of gel solution (without TEMED, 4-Hydroxy-TEMPO or APS) in a well of 12-well plate.
 - b) Wash the coverslips in the gel solution for approximately 1 min.
 - c) Pipette 950 μ l of gel solution in an Eppendorf tube and add 20 μ l of TEMED + 10 μ l 4-Hydroxy-TEMPO + 20 μ l APS. Mix by pipetting and keep on ice to prevent early polymerization.

- d) Pipette 200 μ l for 18 mm \varnothing coverslips and 100 μ l for 12 mm \varnothing coverslips from the solution prepared at point 3, on a layer of parafilm. Place the coverslips flipped on the droplets with the cells facing the parafilm. Incubate for 1 h at RT.

4. Digestion:

- a) Add 1:100 dilution of Proteinase K (final concentration of 8 units/ml) to the digestion buffer.
- b) Face the coverslip with gel upwards and submerge the gel in the digestion buffer. Incubate ON at 37 °C.

Note: The gel will expand approximately 1.5 times during digestion. Add sufficient digestion buffer and leave space for expansion. If necessary, the gel can be trimmed by carefully cutting its sides.

5. Expansion:

- a) Aspirate the digestion buffer.
- b) Place the gel carefully in a petri dish. Try to avoid stress on the gel, as it breaks easily. Remember on which side the coverslip with the cells was located.
- c) Incubate the gel in deionized water for 3-4 h. Exchange the water every 20-30 min. The gel will expand to approximately 4.5 times of its original size.
- d) Optional: Stain nuclei with DAPI.
 - i. Take a piece of the gel.
 - ii. Incubate 10 min with 1:1000 DAPI (1 mg/ml stock) in deionized water.
 - iii. Wash in H₂O for 10 min.

Note: Since the expansion of the gel depends on water, DAPI is slowly washed out when not present in the imaging solution. To ensure a proper signal-to-noise, don't wait too long with microscopy.

6. Mounting:

- a) Prepare 2% low melting agarose (Roboklon #E0303-50) and keep in the water bath at 37 °C.
- b) Cut a small piece of the gel and place it in a 35 mm μ -dish. Face the side with the cells to the glass bottom.
- c) Add agarose and let it harden to fixate the gel.
- d) Add water on top to prevent shrinkage and dehydration.
- e) Seal the chamber with parafilm.
- f) Let the sample settle for a few hours before imaging to prevent moving artifacts during imaging.

B List of hazardous substances



Figure B.1: Globally harmonized system of classification and labelling of chemicals. Their symbols, numbers and summarized meaning.

Table B.1: GHS Hazard statements

Hazardous statements	Meanings
H200	Unstable Explosive.
H201	Explosive; mass explosion hazard.
H202	Explosive; severe projection hazard.
H203	Explosive; fire, blast or projection hazard.
H204	Fire or projection hazard.
H205	May mass explode in fire.
H206	Fire, blast or projection hazard; increased risk of explosion if desensitizing agent is reduced.

Table B.1. (continued)

Hazardous statements	Meanings
H207	Fire or projection hazard; increased risk of explosion if desensitizing agent is reduced.
H208	Fire hazard; increased risk of explosion if desensitizing agent is reduced.
H220	Extremely flammable gas.
H221	Flammable gas.
H222	Extremely flammable aerosol.
H223	Flammable aerosol.
H224	Extremely flammable liquid and vapour.
H225	Highly flammable liquid and vapour.
H226	Flammable liquid and vapour.
H227	Combustible liquid.
H228	Flammable solid.
H229	Pressurized container may burst if heated.
H230	May react explosively even in the absence of air.
H231	May react explosively even in the absence of air at elevated pressure and/ or temperature.
H232	May ignite spontaneously if exposed to air.
H240	Heating may cause an explosion.
H241	Heating may cause a fire or explosion.
H242	Heating may cause a fire.
H250	Catches fire spontaneously if exposed to air.
H251	Self-heating; may catch fire.
H252	Self heating in large quantities; may catch fire.
H260	In contact with water releases flammable gases which may ignite spontaneously.
H261	In contact with water releases flammable gas.
H270	May cause or intensify fire; oxidizer.
H271	May cause fire or explosion; strong oxidizer.
H272	May intensify fire; oxidizer.
H280	Contains gas under pressure; may explode if heated.
H281	Contains refrigerated gas; may cause cryogenic burns or injury.
H282	Extremely flammable chemical under pressure may explode if heated.
H283	Flammable chemical under pressure may explode if heated.
H284	Chemical under pressure; may explode if heated.
H290	May be corrosive to metals.
H300	Fatal if swallowed.
H301	Toxic if swallowed.

Table B.1. (continued)

Hazardous statements	Meanings
H302	Harmful if swallowed.
H303	May be harmful if swallowed.
H304	May be fatal if swallowed and enters airways.
H305	May be fatal if swallowed and enters airways.
H310	Fatal in contact with skin.
H311	Toxic in contact with skin.
H312	Harmful in contact with skin.
H313	May be harmful in contact with skin.
H314	Causes severe skin burns and eye damage.
H315	Causes skin irritation.
H316	Causes mild skin irritation.
H317	May cause an allergic skin reaction.
H318	Causes serious eye damage.
H319	Causes serious eye irritation.
H320	Causes eye irritation.
H330	Fatal if inhaled.
H331	Toxic if inhaled.
H332	Harmful if inhaled.
H333	May be harmful if inhaled.
H334	May cause allergy or asthma symptoms or breathing difficulties if inhaled.
H335	May cause respiratory irritation.
H336	May cause drowsiness or dizziness.
H340	May cause genetic defects.
H341	Suspected of causing genetic defects.
H350	May cause cancer.
H351	Suspected of causing cancer.
H360	May damage fertility or the unborn child.
H361	Suspected of damaging fertility or the unborn child.
H362	May cause harm to breast-fed children.
H370	Causes damage to organs.
H371	May cause damage to organs.
H372	Causes damage to organs through prolonged or repeated exposure.
H373	Causes damage to organs through prolonged or repeated exposure.
H400	Very toxic to aquatic life.
H401	Toxic to aquatic life.
H402	Harmful to aquatic life.
H410	Very toxic to aquatic life with long lasting effects.
H411	Toxic to aquatic life with long lasting effects.

Table B.1. (continued)

Hazardous statements	Meanings
H412	Harmful to aquatic life with long lasting effects.
H413	May cause long lasting harmful effects to aquatic life.
H420	Harms public health and the environment by destroying ozone in the upper atmosphere.

Table B.2: GHS precautionary statements

Hazardous statements	Meanings
P101	If medical advice is needed, have product container or label at hand.
P102	Keep out of reach of children.
P103	Read label before use.
P201	Obtain special instructions before use.
P202	Do not handle until all safety precautions have been read and understood.
P210	Keep away from heat, hot surface, sparks, open flames and other ignition sources. - No smoking.
P211	Do not spray on an open flame or other ignition source.
P212	Avoid heating under confinement or reduction of the desensitized agent.
P220	Keep away from clothing and other combustible materials.
P221	Take any precaution to avoid mixing with combustibles.
P222	Do not allow contact with air.
P223	Do not allow contact with water.
P230	Keep wetted with...
P231	Handle under inert gas.
P232	Protect from moisture.
P233	Keep container tightly closed.
P234	Keep only in original container.
P235	Keep cool.
P240	Ground/ bond container and receiving equipment.
P241	Use explosion-proof [electrical/ ventilating/ lightning/.../] equipment.
P242	Use only non-sparking tools.
P243	Take precautionary measures against static discharge.
P244	Keep valves and fittings free from oil and grease.
P250	Do not subject to grinding/ shock/ friction/...
P251	Do not pierce or burn, even after use.
P260	Do not breathe dust/ fume/ gas/ mist/ vapours/ spray.
P261	Avoid breathing dust/ fume/ gas/ mist/ vapours/ spray.

Table B.2. (continued)

Hazardous statements	Meanings
P262	Do not get in eyes, on skin, or on clothing.
P263	Avoid contact during pregnancy/ while nursing.
P264	Wash ...thoroughly after handling.
P270	Do not eat, drink or smoke when using the product.
P271	Use only outdoors or in a well-ventilated area.
P272	Contaminated work clothing should not be allowed out of the workspace.
P273	Avoid release to the environment.
P280	Wear protective gloves/ protective clothing/ eye protection/ face protection.
P281	Use personal protective equipment as required.
P282	Wear cold insulating gloves/ face shield/ eye protection.
P283	Wear fire resistant or flame retardant clothing.
P284	[In case of inadequate ventilation] Wear respiratory protection.
P285	In case of inadequate ventilation wear respiratory protection.
P231 + P232	Handle under inert gas/...Protect from moisture.
P235 + P410	Keep cool. Protect from sunlight.

Table B.3: Response precautionary statements

Response precautionary statements	Meanings
P301	IF SWALLOWED ...
P302	IF ON SKIN ...
P303	IF ON SKIN (or hair) ...
P304	IF INHALED ...
P305	IF IN EYES ...
P306	IF ON CLOTHING ...
P307	IF exposed ...
P308	IF exposed or concerned ...
P309	IF exposed or if you feel unwell ...
P310	Immediately call a POISON CENTER or doctor/ physician.
P311	Call a POISON CENTER or doctor/ ...
P312	Call a POISON CENTER or doctor/ ... if you feel unwell.
P313	Get medical advice/ attention.
P314	Get medical advice/ attention if you feel unwell.
P315	Get immediate medical advice/ attention.

Table B.3. (continued)

Response precautionary statements	Meanings
P320	Specific treatment is urgent (see ... on this label).
P321	Specific treatment (see ... on this label).
P332	Specific measures (see ... on this label).
P330	Rinse mouth.
P331	Do NOT induce vomiting.
P332	IF SKIN irritation or rash occurs ...
P333	If skin irritation or rash occurs ...
P334	Immerse in cool water [or wrap in wet bandages].
P335	Brush off loose particles from skin.
P336	Thaw frosted parts with lukewarm water. Do not rub affected area.
P337	If eye irritation persists ...
P338	Remove contact lenses, if present and easy to do. Continue rinsing.
P340	Remove victim to fresh air and keep at rest in a position comfortable for breathing.
P341	If breathing is difficult, remove victim to fresh air and keep at rest in a position comfortable for breathing.
P342	If experiencing respiratory symptoms ...
P350	Gently wash with plenty of soap and water.
P351	Rinse cautiously with water for several minutes.
P352	Wash with plenty of water/ ...
P353	Rinse skin with water [or shower].
P360	Rinse immediately contaminated clothing and skin with plenty of water before removing clothes.
P361	Take off immediately all contaminated clothing.
P362	Take of contaminated clothing.
P363	Wash contaminated clothing before reuse.
P364	And wash if before reuse.
P370	In case of fire ...
P371	In case of major fire and large quantities ...
P372	Explosion risk.
P373	DO NOT fight fire when fire reaches explosives.
P374	Fight fire with normal precautions from a reasonable distance.
P376	Stop leak if safe to do so.
P377	Leaking gas fire: Do not extinguish, unless leak can be stopped safely.
P378	Use ... to extinguish.
P380	Evacuate area.

Table B.3. (continued)

Response precautionary statements	Meanings
P381	In case of leakage, eliminate all ignition sources.
P390	Absorb spillage to prevent material damage.
P391	Collect spillage.
P301 + P310	IF SWALLOWED: Immediately call a POISON CENTER/ doctor/...
P301 + P312	IF SWALLOWED: Call a POISON CENTER/ doctor/... IF you feel unwell.
P301 + P330 + P331	IF SWALLOWED: Rinse mouth. Do NOT induce vomiting.
P302 + P334	IF ON SKIN: Immerse in cool water [or wrap in wet bandages].
P302 + P335 + P334	Brush off loose particles from skin. Immerse in cool water [or wrap in wet bandages].
P302 + P350	IF ON SKIN: Gently wash with plenty of soap and water.
P302 + P352	IF ON SKIN: Wash with plenty of water.
P303 + P361 + P353	IF ON SKIN (or hair): Take off immediately all contaminated clothing. Rinse SKIN with water [or shower].
P304 + P312	IF INHALED: Call a POISON CENTER/ doctor/... if you feel unwell.
P304 + P340	IF INHALED: Remove person to fresh air and keep comfortable for breathing.
P304 + P341	IF INHALED: If breathing is difficult, remove victim to fresh air and keep at rest in a position comfortable for breathing.
P305 + P351 + P338	IF IN EYES: Rinse cautiously with water for several minutes. Remove contact lenses if present and easy to do - continue rinsing.
P306 + P360	IF ON CLOTHING: Rinse immediately contaminated CLOTHING and SKIN with plenty of water before removing clothes.
P307 + P311	IF exposed: call a POISON CENTER or doctor/ physician.
P308 + P311	IF exposed or concerned: Call a POISON CENTER/ doctor/...
P308 + P313	IF exposed or concerned: Get medical advice/ attention.
P309 + P311	IF exposed or if you feel unwell: call a POISON CENTER or doctor/ physician.
P332 + P313	IF SKIN irritation occurs: Get medical advice/ attention.
P333 + P313	IF SKIN irritation or rash occurs: Get medical advice/ attention.

Table B.3. (continued)

Response precautionary statements	Meanings
P335 + P334	Brush off loose particles from skin. Immerse in cool water/ wrap in wet bandages.
P337 + P313	IF eye irritation persists: Get medical advice/ attention.
P342 + P311	IF experiencing respiratory symptoms: Call a POISON CENTER/ doctor/...
P361 + P364	Take off immediately all contaminated clothing and wash it before reuse.
P362 + P364	Take off contaminated clothing and wash it before reuse.
P370 + P376	In case of fire: Stop leak if safe to do so.
P370 + P378	In case of fire: Use ... to extinguish.
P370 + P380	In case of fire: Evacuate area.
P370 + P380 + P375	In case of fire: Evacuate area. Fight fire remotely due to the risk of explosion.
P371 + P380 + P375	In case of major fire and large quantities: Evacuate area. Fight fire remotely due to the risk of explosion.

Table B.4: Storage precautionary statements

Storage precautionary statements	Meanings
P401	Store in accordance with ...
P402	Store in a dry place.
P403	Store in a well-ventilated place.
P404	Store in a closed container.
P405	Store locked up.
P406	Store in corrosive resistant/... container with a resistant inner liner.
P407	Maintain air gap between stacks or pallets.
P410	Protect from sunlight.
P411	Store at temperatures not exceeding... °C/ ... °F.
P412	Do not expose to temperatures exceeding 50 °C/ 122 °F.
P413	Store bulk masses greater than ... kg/ ...lbs at temperatures not exceeding ... °C/ ... °F.
P420	Store separately.
P422	Store contents under ...
P402 + P404	Store in a dry place. Store in a closed container.
P403 + P233	Store in a well-ventilated place. Keep container tightly closed.
P403 + P235	Store in a well-ventilated place. Keep cool.

Table B.4. (continued)

Storage precautionary statement	Meanings
P410 + P403	Protect from sunlight. Store in a well-ventilated place.
P410 + P412	Protect from sunlight. Do not expose to temperatures exceeding 50 °C/ 122 °F.
P411 + P235	Store at temperatures not exceeding ... °C/ ... °F. Keep cool.

Table B.5: Disposal precautionary statements.

Disposal precautionary statements	Meanings
P501	Dispose of contents/ container to...
P502	Refer to manufacturer or supplier for information on recovery or recycling.

Table B.6: GHS substances used for the work presented in this thesis

Reagent (CAS #)	Picto-gram	Hazardous (H) statements	Precautions (P) statements
Acrylamide (79-06-1)	GHS06 GHS08	H301, H312 + H332, H315, H317, H319, H332, H340, H350, H361, H372	P201, P202, P260, P261, P264, P270, P271, P272, P280, P281, P301 + P310, P302 + P352, P304 + P312, P304 + P340, P305 + P351 + P338, P308 + P313, P312, P314, P321, P322, P330, P332 + P313, P333 + P313, P337 + P313, P362, P363, P405, P501
AgaroseOut (EURX) DNA purification kit (-)	GHS02 GHS05 GHS07	H225, H302 + H332, H314, H319, H412	P273, P280, P301 + P312 + P330 + P331, P303 + P361 + P353, P304 + P340, P305 + P315 + P338 + P351, P310, P337+ P313, P405
Ammonium persulfate (7727-54-0)	GHS03 GHS07 GHS08	H272, H302, H315, H317, H319, H334, H335	P210, P220, P221, P261, P264, P270, P271, P272, P280, P285, P301 + P312, P302 + P352, P304 + P340, P304 + P341, P305 + P351 + P338, P312, P321, P330, P332 + P313, P333 + P313, P337 + P313, P342 + P311, P362, P363, P370 + P378, P403 + P233, P405, P501
Ampicillin disodium salt (69-52-3)	GHS08	H317, H334	P261, P272, P280, P285, P302 + P352, P304 + P341, P321, P333 + P313, P342 + P311, P363, P501
Chloramphenicol (56-75-7)	GHS05 GHS07 GHS08	H317, H318, H350, H351, H361	P201, P202, P261, P272, P280, P281, P302 + P352, P305 + P351 + P338, P308 + P313, P310, P321, P333 + P313, P363, P405, P501
cOmplete, EDTA-free protease inhibitor cocktail (-)	GHS05	H314	P260, P280, P301+ P330 + P331, P303 + P361 + P353
DMSO ¹ , anhydrous (67-68-5)	GHS07	H315, H319, H335	P261, P264, P271, P280, P302 + P352, P304 + P340, P305 + P351 + P338, P312, P321, P332 + P313, P337 + P313, P362, P403 + P233, P405, P501

¹Dimethyl sulfoxide

Table B.6. (continued)

Reagent (CAS #)	Pictogram	Hazardous (H) statements	Precautions (P) statements
EDTA ² (60-00-4)	GHS07	H319	P264, P280, P305 + P351 + P338, P337 + P313
EGTA ³ (67-42-5)	GHS07	H315 + H319 + H335	P261, P264, P271, P280, P302 + P352, P304 + P340, P305 + P351 + P338, P312, P321, P332+P313, P337 + P313, P362, P403 + P233, P405, P501
Ethanol (64-17-5)	GHS02	H225	P210, P233, P240, P241, P242, P243, P280, P303 + P361 + P353, P370 + P378, P403 + P235, P501
Formaldehyde (Roti-Histofix 10%) (50-00-0)	GHS07 GHS08	H302 + H312, H315, H317, H319, H335, H341, H350, H371	P280, P302 + P352, P305 + P351 + P338, P308 + P313
Glutaraldehyde (111-30-8)	GHS06 GHS07 GHS08 GHS09	H301, H314, H317, H330, H334, H335, H400, H411	P260, P261, P264, P270, P271, P272, P273, P280, P284, P285, P301 + P310, P301 + P330 + P331, P302 + P352, P303 + P361 + P353, P304 + P340, P304 + P341, P305 + P351 + P338, P310, P312, P320, P321, P330, P333 + P313, P342 + P311, P363, P391, P403 + P233, P405, P501
Guanidine hydrochloride (50-01-1)	GHS07	H302 + H332, H315, H319	P264, P270, P280, P301 + P312, P302+P352, P305 + P351 + P338, P321, P330, P332 + P313, P337 + P313, P362, P501
HEPES ⁴ (7365-45-9)	GHS07	H315, H319, H335	P280, P301 + P312, P302 + P352, P304 + P312, P304 + P340, P305 + P351 + P338, P321, P321, P322, P330, P332 + P313, P337 + P313, P362, P363, P403 + P233, P405, P501
Hydrochloric acid (7647-01-0)	GHS05 GHS06	H314, H331	P260, P261, P264, P271, P280, P301+P330+P331, P303 + P361 + P353, P304 + P340, P305 + P351 + P338, P310, P311, P321, P363, P403 + P233, P405, P501

²Ethylenediaminetetraacetic acid³Ethylenebis(oxyethylenitrilo)tetraacetic acid⁴4-(2-hydroxyethyl)-1-piperazineethanesulfonic acid

Table B.6. (continued)

Reagent (CAS #)	Pictogram	Hazardous (H) statements	Precautions (P) statements
4 -hydroxy-TEMPO ⁵ (2226-96-2)	GHS05 GHS07 GHS08	H302, H315, H318, H319, H335, H373, H412	P260, P261, P264, P270, P271, P273, P280, P301 + P312, P302 + P352, P304 + P340, P305 + P351 + P338, P310, P312, P314, P321, P330, P332 + P313, P337 + P313, P362, P403 + P233, P405, P501
Imidazole (288-32-4)	GHS05 GHS07 GHS08	H302, H314, H360	P201, P202, P260, P264, P270, P280, P281, P301 + P312, P301 + P330 + P331, P303 + P361 + P353, P304 + P340, P305 + P351 + P338, P308 + P313, P310, P321, P330, P363, P405, P501
Isopropanol (67-63-0)	GHS02 GHS07	H225, H319, H336	P210, P233, P240, P241, P242, P243, P261, P264, P271, P280, P303 + P361+P353, P304 + P340, P305 + P351 + P338, P312, P337 + P313, P370 + P378, P403 + P233, P403 + P235, P405, P501
Kanamycin sulfate (25389-94- 0)	GHS08	H360	P201, P202, P281, P308 + P313, P405, P501
MA-NHS ⁶ (38862-25- 8)	GHS07	H302, H315, H317, H319, H332, H335	P261, P264, P270, P271, P272, P280, P301 + P312, P302 + P352, P304 + P312, P304 + P340, P305 + P351 + P338, P312, P321, P330, P332 + P313, P333 + P313, P337 + P313, P362, P363, P403 + P233, P405, P501
Methanol (67-56-1)	GHS02 GHS06 GHS08	H225, H301, H311, H331, H370	P210, P233, P240, P241, P242, P243, P260, P261, P264, P270, P271, P280, P301 + P310, P302 + P352, P303 + P361 + P353, P304 + P340, P307 + 308 + P311, P311, P312, P321, P322, P330, P361, P363, P370 + P378, P403 + P233, P403 + P235, P405, P501

⁵4-Hydroxy-2,2,6,6-tetramethylpiperidinyloxy⁶Methacrylic acid N-hydroxysuccinimide ester

Table B.6. (continued)

Reagent (CAS #)	Pictogram	Hazardous (H) statements	Precautions (P) statements
2-Mercapto-ethanol (60-24-2)	GHS05 GHS06 GHS07 GHS08 GHS09	H301, H302, H310, H311, H314, H315, H317, H318, H331, H332, H361, H373, H400, H410, H411	P201, P202, P260, P261, P262, P264, P270, P271, P272, P273, P280, P281, P301 + P310, P301 + P312, P301 + P330 + P331, P302 + P350, P302 + P352, P303 + P361 + P353, P304 + P312, P304 + P340, P305 + P351 + P338, P308 + P313, P310, P311, P312, P314, P321, P322, P330, P332 + P313, P333 + P313, P361, P362, P363, P391, P403 + P233, P405, P501
N,N-Methylene-bisacrylamide (110-26-9)	GHS05 GHS06 GHS07 GHS08	H301, H302, H312, H317, H318, H332, H340, H350, H351, H360, H361, H372	P201, P202, P260, P261, P264, P270, P271, P272, P280, P281, P301 + P310, P301 + P312, P302 + P352, P304 + P312, P304 + P340, P305 + P351 + P338, P308 + P313, P310, P312, P314, P321, P322, P330, P333 + P313, P363, P405, P501
Microscope oil (-)	GHS07 GHS09		
Midiprep kit (Qiagen) ⁷ (1132-61-2, 64-19-7, 2682-20-4, 67-68-5, 9001-99-4, 151-21-3, 1310-73-2)	GHS02 GHS05 GHS08	H226, H290, H315, H317, H319, H334	P210, P261, P280, P284, P308 + P311, P340
Phalloidin (17466-45-4)	GHS06	H300, H310, H330	P260, P262, P264, P270, P271, P280, P284, P301 + P310, P302 + P350, P304 + P340, P310, P320, P321, P322, P330, P361, P363, P403 + P233, P405, P501

⁷containing: MOPS, acetic acid, CMIT7/MIT (3:1), dimethyl sulfoxide, isopropanol, RNase, sodium dodecyl sulphate, sodium hydroxide

Table B.6. (continued)

Reagent (CAS #)	Pictogram	Hazardous (H) statements	Precautions (P) statements
Potassium hydroxide (1310-58-3)	GHS05 GHS07	H290, H302, H314	P260, P264, P270, P280, P301 + P312 P330 + P331, P303 + P361 + P353, P304 + P340, P305 + P351 + P338, P308 + P310, P321, P330, P363, P405, P501
Rotiphorese Gel 40 ⁸ (79-06-1, 110-26-9)	GHS07 GHS08	H302 + H332, H315, H317, H319, H340, H350, H361, H372	P201, P280, P302 + P352, P304 + P340, P305 + P351 + P338, P308 + P313, P314
Sodium acrylate (7446-81-3)	GHS09	H400, H411	P273, P391, P501
TEMED ⁹ (110-18-9)	GHS02 GHS05 GHS07	H225, H302, H314, H332	P210, P233, P240, P241, P242, P243, P260, P261, P264, P270, P271, P280, P301 + P312, P301 + P330 + P331, P303 + P361 + P353, P304 + P312, P304 + P340, P305 + P351 + P338, P310, P312, P321, P330, P363, P370 + P378, P403 + P235, P405, P501
Tetrodotoxine (4368-28-9)	GHS06	H300, H310, H330	P260, P262, P264, P270, P271, P280, P284, P301 + P310, P302 + P350, P304 + P340, P310, P320, P321, P322, P330, P361, P363, P403 + P233, P405, P501
TRIS ¹⁰ (77-86-1)	GHS07	H315, H319, H335	P261, P264, P271, P280, P302 + P352, P304 + P340, P305 + P351 + P338, P312, P321, P332 + P313, P337 + P313, P362, P403 + P233, P405, P501
Triton-X-100 (9002-93-1)	GHS05 GHS07 GHS09	H302, H315, H318, H319, H410, H411, H412	P264, P270, P273, P280, P301 + P312, P302 + P352, P305 + P351 + P338, P310, P321, P330, P332 + P313, P337 + P313, P362, P391, P501

⁸40 % acrylamide-, bisacrylamide 5:1 solution⁹N, N, N', N'-Tetramethylethylenediamine¹⁰2-amino-2-hydroxymethyl-propane-1,3-diol

Table B.6. (continued)

Reagent (CAS #)	Picto- gram	Hazardous (H) state- ments	Precautions (P) statements
Trypsin (9002-07-7)	GHS07 GHS08	H315, H319, H334, H335	P261, P264, P271, P280, P285, P302 + P352, P304 + P340, P304 + P341, P305 + P351 + P338, P312, P321, P332 + P313, P337 + P313, P342 + P311, P362, P403 + P233, P405, P501

Acknowledgements

I would like to thank the people that helped me during the past 4 years, the time of my doctoral studies. To obtain the results described in this work your help was very welcome - all the help directly related to the work, but also the support outside of working/study time.

First, I would like to thank my parents for supporting my education leading to the start of my doctoral studies. Also for the numerous Skype hours, to check with me if everything was going well. Your visits to Hamburg (including Ghislaine) and the invitations for holidays were very well appreciated. I would also like to thank all of my friends in the Netherlands. Coming back to the Netherlands was not always easy and visits were often short. Nonetheless, the times we had were always like the 'old times' and were great fun. Your visits to Hamburg are also not forgotten. You are always very welcome in Hamburg, perhaps Berlin in the future.

One of the most important things I learned during my doctoral studies is that science is a team effort. Working together and sharing knowledge is the fastest and best way to success - a wise lesson from Marina, which I would also like to thank for giving me the opportunity to conduct my doctoral studies in her group. Over the years, you put a great team together. At the start, the group was very small and we had to set up the lab from almost nothing. This was for a beginning doctoral student not always easy, but very educative. With the help of Sabine and Julia everything went much faster, thank you! In special, I would like to thank Julia for the great help and time, in- and outside of the lab.

Shortly after, the group grew with new members Anja and Sergei. Sergei, thank you for showing me a glimpse of software development. I hope you have a good time as a microscopy specialist. Anja, thank you very much for working together. Together we have some very nice publications. Indirectly you taught me about veganism. I will not adapt it, but it shows a lot of strength from you to pursue this lifestyle. Good luck in the future, I hope you find a nice job after your doctoral studies. A little later we got help from a great chemist. Michi (Michael) thank you for all the help with the 'hardcore' chemistry questions. Don't let the chemicals touch your brain too much, sleep well and enjoy diving. Judit and Friederike, thank you very much for bringing the good mood and help to the lab. I would also like to thank Jasper for the organisation and discussions during the lab meetings. Not to forget his donations from the Netherlands (hagelslag and chocolates!). Yannes, all the best with your master thesis. Would you be part of the next paragraph?

Best wishes to the new generation of PhD students. Tomas, Dani (Daniela) and Nathalie, I hope to attend three nice PhD defences in 3-4 years. Tomas, thank you for the good Italian coffee and being a companion with experience in electrophysiology. Dani, it was great to have you one year as a student/assistant. It makes me proud to see you now working as a PhD student. Nathalie, good luck with studying cellular transport. The imaging and analysis can be a pain, but there is still a lot to discover. I'm sure you and Dani will form the start of a great team in Berlin. I'm certain that many talented people will follow.

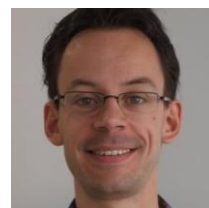
I would also like to thank Henning Tidow, and the biochemistry department of Universität Hamburg for having me as student in your faculty. Thank you for your effort and guidance during my PhD studies.

At last, I would like to thank all people that helped me and were not mentioned here. Your help was very much appreciated.

Curriculum Vitae

Bas van Bommel was born on the 9th of February 1992 in Utrecht, The Netherlands. He started school at the primary school 'De Tandem' - IJsselstein. In 2004, he continued with high school at the 'Anna van Rijn College' - Nieuwegein, from which he graduated in 2010. At high school, he was mostly interested in beta studies, and followed the direction of 'Nature and Health' including classes in Physics, Chemistry and Biology. As part of his high school thesis, Bas participated in the Dutch CanSat competition. A competition for students, organized by the Technical University Delft, in which students build their own satellites in cans. After high school, he continued with a bachelor in Biomedical Sciences at the Utrecht University. During his bachelor studies, he pursued his developing interest in neuroscience. After obtaining his bachelor degree 2013, he continued with the master Neuroscience and Cognition, following the track focussing on molecular neuroscience. As part of the master studies, he conducted two internships. One 9 months internship in the department of Biology at the Utrecht University under supervision of Dr. C. J. Wierenga and Dr. C. C. Hoogenraad, followed by a 6 months internship in the Institute for Synaptic Physiology at the Center for Molecular Neurobiology Hamburg with supervision of Dr. C. E. Gee and Dr. Prof. T. G. Oertner. Both internships were focused on the physiology of neurons, studied by electrophysiology. Bas obtained his master degree in the year 2015. Directly after his master degree, Bas started as PhD candidate in the research group of Dr. M. Mikhaylova. Here he studied cellular trafficking and physiology in neurons, mainly applying high-end microscopy techniques. Results obtained during this time are part of this dissertation.

Name: Bas van Bommel
Date of birth: 9. Feb. 1992
Place of birth: Utrecht
Nationality: Dutch



Education

- 2016 – 2020 **PhD candidate at the department of Biochemistry**
University Hamburg & Center for Molecular Neurobiology Hamburg (ZMNH), Germany
- Thesis Title: ‘Structural and functional characterization of the actin and microtubule cytoskeleton in dendrites’
Research group: Neuronal Protein Transport
Supervisors: Dr. Marina Mikhaylova and Dr. Henning Tidow
Co-supervisor: Dr. Thomas G. Oertner
- 2013-2015 **Master Neuroscience & Cognition**
Utrecht University, Utrecht, The Netherlands
- Courses: Introduction to Neurosciences (UU), Behaviour Genetics (VU Amsterdam), Life Cell Imaging (VU Amsterdam), Laboratory Animal Sciences (UU)
- 9 months internship
‘The role of TRIM46 in neuronal excitability’
Supervisors: Dr. Corette J. Wierenga and Dr. Casper C. Hoogenraad
Department of Cell Biology, Utrecht University, The Netherlands
- 6 months internship
‘Optic control of spike timing-dependent plasticity’
Supervisors: Dr. Christine E. Gee, Dr. Thomas G. Oertner and Dr. Geert M. J. Ramakers
Institute for Synaptic Physiology, ZMNH, Hamburg, Germany
- Thesis: ‘Physiological and molecular tuning of synaptic plasticity’
Supervisors: Dr. Marina Mikhaylova and Dr. Casper C. Hoogenraad
RG Neuronal Protein Transport, ZMNH, Hamburg, Germany
- 2010 - 2013 **Bachelor Biomedical Sciences**
Utrecht University, Utrecht, The Netherlands
- 2004 - 2010 **High school with A-levels diploma in ‘Nature and Health’ profile**
Anna van Rijn College, Nieuwegein, The Netherlands

Additional education

2019	Course Biosafety officer (GenTSV), <i>BioMedConcept GmbH, Berlin, Germany</i>
2014	FELASA C, Utrecht University, <i>Utrecht, The Netherlands</i>
2010	Diploma veilige microbiologische technieken ('Safe microbiological techniques'), <i>Utrecht University, Utrecht, The Netherlands</i>
2009	First aid diploma, <i>EHBO IJsselstein, The Netherlands</i>

Research skills

Molecular cloning

Preparation and maintaining model systems

Standardized cell lines, primary hippocampal cultures and organotypic hippocampal slice cultures

Microscopy of fixed and living samples

epi-fluorescence, TIRF, FRAP, laser scanning/spinning-disk confocal, 2-photon, SHG, SIM, STED

Expansion microscopy

Patch clamp electrophysiology

Single-cell electroporation

Viral transduction

Image processing in ImageJ/Fiji

Matlab programming

Languages

Dutch	native
English	fluent
German	average

Eidesstattliche Versicherung

Hiermit versichere ich an Eides statt, die vorliegende Dissertation selbst verfasst und keine anderen als die angegebenen Hilfsmittel benutzt zu haben. Die eingereichte schriftliche Fassung entspricht der auf dem elektronischen Speichermedium. Ich versichere, dass diese Dissertation nicht in einem früheren Promotionsverfahren eingereicht wurde.

Hamburg, den 16.04.2020



Bas van Bommel